

1



2

Exploiting CVD diamond properties for particle detection and identification

3

4

5

Matevž Červ

6

Vienna University of Technology

7

A thesis submitted for the degree of

8

Doctor of technical sciences

9

Geneva 2016

¹⁰ Contents

¹¹ 1	Introduction	1
¹² 1.1	Fundamental research	2
¹³ 1.1.1	CERN	3
¹⁴ 1.1.2	Particle accelerators	4
¹⁵ 1.1.3	The ATLAS experiment	5
¹⁶ 1.1.4	Atominstirut, Vienna	6
¹⁷ 1.1.5	n-ToF	7
¹⁸ 1.2	Particle detectors	8
¹⁹ 1.2.1	Semiconductor detectors	9
²⁰ 1.2.2	Diamond sensors	10
²¹ 2	Signal formation in diamond	12
²² 2.1	Principles of signal formation in semiconductors	13
²³ 2.1.1	Signal induction by moving charges	15
²⁴ 2.1.2	Radiation-induced electrical pulses	17
²⁵ 2.1.3	Signal charge fluctuations	18
²⁶ 2.2	Carrier transport in a diamond sensor	18
²⁷ 2.3	Electronics for signal processing	21
²⁸ 2.3.1	Signal preamplifiers	21
²⁹ 2.3.1.1	Current-sensitive amplifier	21
³⁰ 2.3.1.2	Charge-sensitive amplifier	22
³¹ 2.3.1.3	Analogue electronic noise	23
³² 2.3.2	Analogue-to-digital converters	23
³³ 2.3.3	Digital signal processing	24
³⁴ 3	Experimental results	
³⁵	<i>Diamond irradiation study</i>	27
³⁶ 3.1	Measurement setup	28
³⁷ 3.1.1	Preamplifiers	28
³⁸ 3.1.1.1	Calibration	29
³⁹ 3.1.2	Diamond samples	30
⁴⁰ 3.1.3	Readout devices	31
⁴¹ 3.1.4	Setup for the efficiency study using β particles	31
⁴² 3.1.5	Room temperature α -TCT setup	32

CONTENTS

43	3.1.6	Cryogenic α -TCT setup	32
44	3.2	Charged particle pulses and spectra	34
45	3.2.1	Noise limitations	34
46	3.3	Radiation limitations	36
47	3.3.1	Quantifying radiation damage in diamonds	37
48	3.3.1.1	Irradiation with a $\pi_{300 \text{ MeV}}$ beam	37
49	3.3.1.2	Charge collection efficiency and charge collection distance	38
50	3.3.1.3	Irradiation damage factor	39
52	3.3.2	Long-term measurement stability	40
53	3.3.2.1	β long-term stability	41
54	3.3.2.2	α long-term stability	42
55	3.4	Temperature limitations	46
56	3.4.1	Temperature-variant α -TCT before irradiation	48
57	3.4.2	Temperature-variant α -TCT after irradiation	50
58	3.4.2.1	Collected charge as a function of temperature	51
59	3.4.2.2	Charge trapping	53
60	3.5	Conclusion	57
61	4	Charge monitoring	
62		<i>The ATLAS Diamond Beam Monitor</i>	58
63	4.1	Luminosity measurements	59
64	4.2	Diamond pixel module	60
65	4.2.1	Sensors	61
66	4.2.2	Front-end electronics	62
67	4.3	Module assembly and quality control	64
68	4.3.1	Assembly	64
69	4.3.2	Testing	65
70	4.3.3	Installation and commissioning	66
71	4.4	Performance results	67
72	4.4.1	Source tests	67
73	4.4.2	Test beam results	68
74	4.5	Operation	70
75	4.5.1	Positioning	70
76	4.5.2	Data taking during collisions	71
77	4.6	Conclusion	73
78	5	Current monitoring	
79		<i>Real-time particle identification</i>	75
80	5.1	Motivation	76
81	5.2	Requirements	76
82	5.3	Device specifications	77
83	5.4	Pulse parameters	77

CONTENTS

84	5.5 Applications	78
85	5.6 Description of the firmware	79
86	5.6.1 Design constraints	80
87	5.6.2 Analysis module	80
88	5.6.3 Vector cleaning for area and width measurements	83
89	5.6.3.1 Vector cleaning	84
90	5.6.3.2 Algorithm	85
91	5.7 Control and data interface	85
92	5.7.1 Software	86
93	5.7.2 Data readout	86
94	5.8 Performance results	88
95	5.8.1 Comparison between the charge- and current-sensitive spec-	
96	troscopy	89
97	5.9 Source calibration	89
98	5.9.1 Source measurements - scatter plots	93
99	5.9.2 Discussion	101
100	5.9.3 Space charge build-up	102
101	5.10 Applications in neutron instrumentation	104
102	5.10.1 Thermal neutron flux monitoring	104
103	5.10.1.1 Measurements	105
104	5.10.1.2 Results	106
105	5.10.2 Fusion power monitoring	106
106	5.10.3 Fast neutron monitoring	107
107	5.11 Conclusion	109

¹⁰⁸ List of Figures

¹⁰⁹ 1.1	Standard model [22]	2
¹¹⁰ 1.2	The Large Hadron Collider [20]	4
¹¹¹ 1.3	The ATLAS Experiment [38]	5
¹¹² 1.4	The TRIGA MARK II neutron reactor [15]	7
¹¹³ 1.5	The calorimeter in the n-ToF area [19]	8
¹¹⁴ 1.6	The Insertable B-Layer – a silicon particle tracker installed in the ATLAS experiment in 2014 [34]	9
¹¹⁵ 1.7	A pCVD diamond pad detector [23]	10
¹¹⁷ 2.1	In the equivalent electrical circuit diagram, electron-hole creation and drift can be modelled as a current source with a capacitor in parallel	14
¹¹⁹ 2.2	Stopping power for muons according to the Bethe-Bloch formula []	15
¹²⁰ 2.3	A point-like charge inducing current in a conductive plane	15
¹²¹ 2.4	Charge carrier drift in diamond for β/γ and for α particles	17
¹²² 2.5	Calculated intrinsic energy resolution for silicon and diamond	19
¹²³ 2.6	Introduction of space charge in the diamond bulk. The induced current signal is proportional to the effective electrical field. d is the thickness of the diamond sensor.	20
¹²⁵ 2.7	Introduction of impurities and non-uniformities into the crystal lattice due to radiation damage.	21
¹²⁶ 2.8	Simplified equivalent circuits of a current and charge amplifier	22
¹²⁷ 2.9	Input and output signal of the current amplifier	22
¹²⁸ 2.10	Input and output signal of the charge amplifier	23
¹²⁹ 2.11	Input signal digitisation and quantisation error	24
¹³⁰ 2.12	An example of an FPGA and an ASIC chip	26
¹³³ 3.1	Diagram of a diamond detector readout chain.	28
¹³⁴ 3.2	Amplifiers used for the charge and current measurements	29
¹³⁵ 3.3	Two scCVD diamond samples: A IIa 1scdhq (left) and an E6 S37 (right)	30
¹³⁶ 3.4	Positioning of the α -source on top of the sensor carrier	33
¹³⁷ 3.5	Superimposed and averaged pulses (a, b and c, current amplifier) and distributions of deposited energy (d, e, f, charge amplifier) for three types of radiation. Note the scale on the X axis of the distributions. .	35

LIST OF FIGURES

140	3.6	Diamond radiation damage - a model based on displacements per atom [26]. Added are data points for protons and pions by RD42 [35] and one data point for pions measured in the scope of this thesis.	38
141	3.7	First figure shows the CCD for S37, S79 and S52 at a range of bias voltage settings. The charge collection distance at 1 V/ μm bias voltage for the three diamond samples is then compared to the RD42 data for pion irradiation in the second figure. The data points are about 15–25 % lower than expected from the RD42 data [35].	40
142	3.8	Relative increase of charge collection over time due to priming with the ^{90}Sr radioactive source. The bias voltage for this measurement is 1 V/ μm	42
143	3.9	Relative decrease of collected charge with time for non-irradiated and irradiated diamond samples.	43
144	3.10	The signal of the irradiated and primed S79 deteriorates with time for both polarities. Every plot contains 60 superimposed pulses.	44
145	3.11	Deterioration of the pulse shapes with time	45
146	3.12	Five procedures for the “healing” process for an irradiated diamond that was exposed to α radiation at bias voltage switched on for at least 30 minutes at a rate of 10^4 s^{-1}	47
147	3.13	Varied bias voltage at a fixed temperature	48
148	3.14	Several data points between 4 K and 295 K at a bias voltage of $\pm 500 \text{ V}$	49
149	3.15	Varied bias voltage at a fixed temperature for an irradiated sample	51
150	3.16	After irradiation: several data points between 4 K and 295 K at a bias voltage of $\pm 500 \text{ V}$	52
151	3.17	Collected charge as a function of temperature	54
152	3.18	Charge carrier lifetime decreases with irradiation, but is stable across the range of temperatures between 4 K – 75 K and 150 K – 295 K. The first figure shows the carrier lifetime s a function of temperature whereas the second figure depcits the carrier lifetime averaged over all temperatures and plotted against the π irradiation dose	56
153	4.1	Diamond detectors installed in high-energy physics experiments in the last decade, sorted by the active sensor area. The first four detectors from the left are radiation monitors whereas the right two are pixel trackers.	59
154	4.2	DBM module, top-down view. Visible is the flexible PCB with signal and power connections, the silicon sensor and a part of the FE-I4. Wire bonds from the PCB to the FE-I4 and to the sensor are also visible.	60
155	4.3	A pCVD wafer. The golden dots on the surface are the electrodes that are applied during the qualification test. The wafer is measured across the surface to find the regions with the highest efficiency.	61

LIST OF FIGURES

180	4.4	FE-I4 layout, top-down view. The pink area are pixels grouped into columns, the green area below is the common logic and the red strip at the bottom are the wire bond pads.	62
181	4.5	Schematic of an analog pixel. Courtesy of the FE-I4 collaboration. . .	63
182	4.6	Module production with time	66
183	4.7	Occupancy and pseudo-efficiency scans for the silicon (left) and diamond sensor (right) to check for disconnected regions and estimate the sensor's efficiency. Shadows of the electronic components are clearly visible because fewer electrons were able to traverse through such a higher amount of material.	69
190	4.8	Measurements of pseudo-efficiency and disconnected regions for all modules that went through the QC procedure	70
191	4.9	An efficiency study of a prototype DBM diamond module in a test beam. The statistics are low (~ 10 hits/pixel) as the data was collected during a short run.	70
195	4.10	This photo highlights four telescopes installed onto the nSQPs and around the pipe	71
196	4.11	Position of the DBM in the ATLAS experiment	72
197	4.12	Occupancy of individual modules during collisions. Only 16 modules were taking data.	72
200	4.13	A diagram showing the radial distance R_0 and longitudinal distance Z_0 of the trajectory from the interaction point at the minimal distance d . Z is the axis along the beam line. Three module planes intercept a particle and reconstruct its trajectory.	73
204	4.14	These two plots show two parameters of particle tracks recorded by one of the DBM telescopes: radial and longitudinal distance of the projected tracks from the interaction point.	74
207	5.1	78
208	5.2	Firmware design structure	80
209	5.3	Code design plan	81
210	5.4	A sample pulse. The first vector shows which samples are above the width measurement height. The second vector is a clean vector. The third line shows the position of the maximum amplitude. The vector cleaning algorithm starts from the maximum amplitude and continues in both ways along the vector.	83
215	5.5	This block counts the remaining binary ones in the clean vectors and outputs this value as the pulse width.	84
217	5.6	This block masks the input data with the clean vector and sums the remaining samples.	84
219	5.7	Vector cleaning routine outputs two vectors - one forward in time and one back in time from the peak of the pulse.	84

LIST OF FIGURES

221	5.8 One logic step in the algorithm chain before and after Karnaugh min-	
222	imisation.	85
223	5.9 Abstraction levels of the controller software	86
224	5.10 This figure shows the capability of the device to analyse all arriving	
225	pulses for a range of input frequencies. The highest achievable rate	
226	with zero lost pulses is $5 \times 10^6 \text{ s}^{-1}$	88
227	5.11 These diagrams show the linearity of the measurements and their sta-	
228	bility with respect to analog noise.	90
229	5.12 Spectrum of a $^{148}\text{Gd}^{239}\text{Pu}^{241}\text{Am}^{244}\text{Cm}$ source using a Cx and a C2	
230	amplifier	91
231	5.13 Accumulated pulses for all runs	92
232	5.14 Background measurements	94
233	5.15 ^{241}Am , e^- collection. Qualifier: FWHM 7–10 ns.	95
234	5.16 ^{241}Am , h^+ collection. Qualifier: FWHM 5.5–8 ns.	96
235	5.17 ^{90}Sr	97
236	5.18 ^{60}Co	98
237	5.19 ^{239}Pu Be. Qualifiers: BW-FWHM 0.2–4 ns, FWHM 3–12 ns, Form	
238	factor 1.45	99
239	5.20 ^{239}Pu Be. Qualifiers: BW-FWHM 0.2–4 ns, FWHM 3–12 ns, Slope	
240	25–104 mV/ns	100
241	5.21 Built up space charge causes a slope which has the opposite slope for	
242	electrons and holes	102
243	5.22 Using β radiation to reduce space charge in diamond	103
244	5.23 Thermal neutrons, photons. Qualifier: FWHM 7–12 ns	106
245	5.24 Fast neutrons, thermal neutrons, photons. Qualifiers: BW-FWHM	
246	0–4 ns, FWHM 3–12 ns, Form factor 1.45, Slope 10–108 mV/ns	108

LIST OF FIGURES

²⁴⁷ Chapter 1

²⁴⁸ Introduction

²⁴⁹ The aim of the thesis is to present and discuss applications of diamond based particle
²⁵⁰ detectors.

²⁵¹ The introductory chapter paints a picture of the current state of particle physics
²⁵² research. It presents some of the research institutes that are active in this field,
²⁵³ pushing the boundaries of human knowledge further. It explains their goals and the
²⁵⁴ means with which they are achieving them. Next section describes particle detectors
²⁵⁵ in a broad sense – their history and the types existing now. One type in particular –
²⁵⁶ a diamond detector – is then described more in detail.

²⁵⁷ Second chapter discusses the properties of diamond detectors. Dissecting the
²⁵⁸ detector chain into individual parts and describing them in detail – sensors, amplifiers,
²⁵⁹ digitisers and signal processing units. We learn about energy resolution in diamond,
²⁶⁰ analog and digital noise contribution etc. Principles of signal formation are presented,
²⁶¹ starting with the famous Shockley-Ramo theorem and building from there. We will
²⁶² see that different types of radiation induce different electrical signals.

²⁶³ The base laid down in the second chapter is complemented in the third where the
²⁶⁴ measurements are presented and the results discussed. The focus is on diamond's
²⁶⁵ measurement stability with respect to irradiation damage. To carry out this study,
²⁶⁶ two diamond sensors were irradiated to two different doses, with the measurements
²⁶⁷ carried out before and after irradiation.

²⁶⁸ Building on the understanding of the behaviour of the diamond, two applications
²⁶⁹ were developed. The fourth chapter describes the Diamond Beam Monitor, a detec-
²⁷⁰ tor that makes use of the diamond's charge measurement capabilities and its high
²⁷¹ radiation hardness. This detector has been installed in one of the largest particle
²⁷² physics experiments in the world and is currently taking data. Here, its development
²⁷³ process is presented: the quality control procedures during assembly and installation,
²⁷⁴ its performance in the test environment and some recent experimental data.

²⁷⁵ The final and most important chapter describes the real-time application for par-
²⁷⁶ ticle identification. Here the shape of the electrical signal of the diamond sensor is
²⁷⁷ used to discriminate different types of radiation in real time and dead time free. The
²⁷⁸ chapter includes the description of the device's logic and algorithms, lab test results
²⁷⁹ and the application in neutron monitoring.

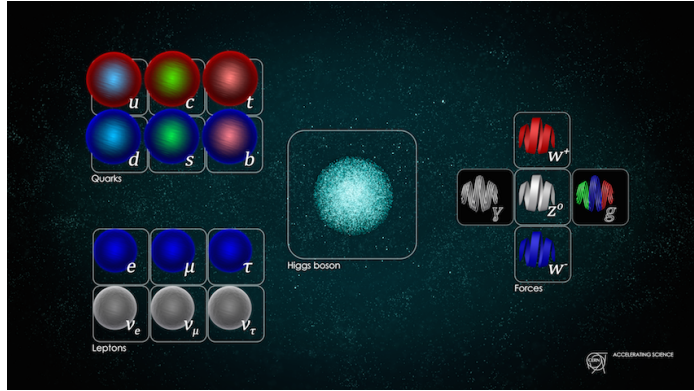


Figure 1.1: Standard model [22]

280 1.1 Fundamental research

281 This section gives a short overview of the institutes and collaborations carrying out
 282 fundamental physics research. The facilities were used for the research carried out in
 283 this thesis.

284 The aim of fundamental (even pure or basic) research is to improve the scientific
 285 theories and verify them to improve our understanding of the universe. It does not
 286 in itself focus on applying this research by developing products and is not meant to
 287 create a direct return on investment. Instead, it expands the overall knowledge of the
 288 human kind - by making the results freely available to the general public.

289 Particle physics research peers into the smallest constituents of the universe, dis-
 290 secting the atoms into quarks and electrons, catching cosmic rays and figuring out
 291 what dark matter is made up of. Particle physicists want to explain the phenomena
 292 surrounding us by studying the fundamental particles and the mechanisms governing
 293 their interactions. By understanding this, we would be able to answer difficult ques-
 294 tions; How did the universe begin? What is the invisible force (dark matter, dark
 295 energy) pushing the galaxies apart from each other? Where does mass come from?
 296 Why is there almost no antimatter in the universe? In this effort, scientists have
 297 formed several theories. One of them, the Standard Model of particles, is currently
 298 the best theory to describe the visible universe.

299 **The Standard Model** (SM) is a physics theory developed in the 1970's [37]. It
 300 was designed to explain the current experimental results. As such, it was also able to
 301 predict new discoveries and was a driving force for the scientists to invest time and
 302 money in developing new experiments. To date, it is by far the most established and
 303 verified physics theory. It explains how the basic building blocks of matter – *fermions*
 304 – interact with each other via mediators of interactions called *bosons*. There are two
 305 main families of fermions - *quarks* and *leptons*, as shown in diagram 5.22. Each group
 306 consists of six members divided into three *generations*, the first being the lightest and
 307 most stable and the last the heaviest – unstable. The nature around us is made up
 308 of the stable particles – those from the second or third generations can only be found

- 309 in cosmic rays or produced artificially using particle accelerators.
- 310 Quarks have a spin of 1/2 and a charge of either +2/3 (up, charm, top) or -1/3
311 (down, strange, bottom) while the leptons have a spin of 1/2 and a charge of either 1
312 (electron, muon, tau) or 0 (electron neutrino, muon neutrino, tau neutrino). Leptons
313 only exist individually – they do not cluster. Quarks, however, immediately form a
314 cluster of either two (unstable), three (more stable) or five (unstable). Two up and
315 one down quark make up a proton whereas two down and one up quark make up a
316 neutron.
- 317 In addition to fermions, each particle has its corresponding antiparticle – a particle
318 with the same mass but the opposite charge. If an antiparticle hits a particle, they
319 annihilate each other, producing energy in form of photons.
- 320 Bosons are the carriers of force, mediating weak (W^+ , W^- and Z bosons), strong
321 (gluons) and electromagnetic (photons) interactions. The weak interaction is respons-
322 sible for the radioactive decay of subatomic particles, thus playing an essential role in
323 nuclear fission – a process taking place in the stars. The electromagnetic interaction
324 works at a macroscopic level – it allows particles to interact via electric and magnetic
325 fields. The strong interaction is effective at distances of a femtometer and it governs
326 how quarks interact and bind with each other. An additional boson is the Higgs
327 boson and was discovered at CERN in 2012 []. It is a representation of the Higgs
328 mechanism, which gives rise to the mass (or lack thereof) of all the particles in the
329 Standard Model.

330 **1.1.1 CERN**

- 331 CERN (European Centre for Nuclear Research) [6] is a nuclear research institute
332 housing the largest particle physics laboratory in the world. It straddles the Swiss-
333 French border just outside Geneva. It was established in 1954 to bring the war-torn
334 Europe together by means of fundamental scientific research. Today, it has 22 mem-
335 ber state countries and several observer states. More than 10000 scientists, engineers,
336 technicians, students and others from all around the globe work at CERN on many
337 projects in research fields ranging from particle to nuclear physics. The scope is to
338 probe the fundamental structure of the universe and to understand the mechanisms
339 governing it. Therefore CERN’s main function is to provide the infrastructure for
340 high-energy physics experiments. These are carried out using large machines called
341 particle accelerators. These instruments boost beams of particles to high energies
342 before making them collide with each other or with stationary targets. The result-
343 ing collisions are recorded by particle detectors and later analysed by physicists. To
344 carry out research on the smallest constituents of matter, their dynamics and struc-
345 ture, very high energies are needed. This is why the most powerful accelerators are
346 used for fundamental research. The largest accelerators at CERN are the Proton
347 Synchrotron [], the Super Proton Synchrotron [36] and the Large Hadron Collider [].

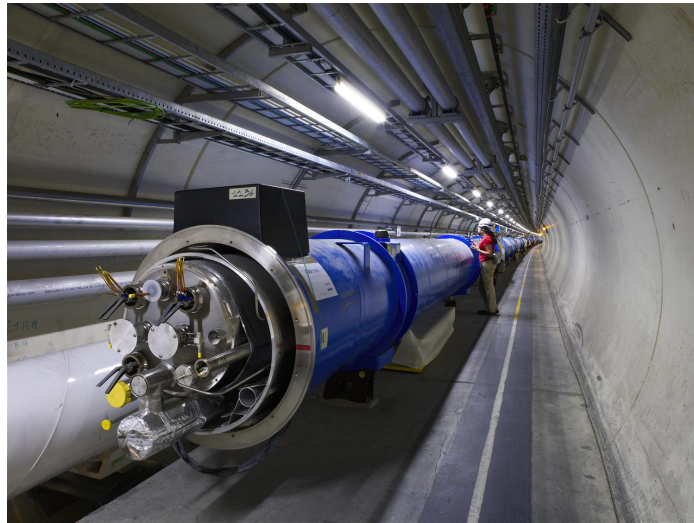


Figure 1.2: The Large Hadron Collider [20]

348 **1.1.2 Particle accelerators**

349 A particle accelerator is a machine that accelerates beams of charged particles like
350 protons, electrons, ions etc. It generates electric fields that add kinetic energy to the
351 particles, speeding them up. It then uses magnets to retain them within a defined
352 trajectory and inside the evacuated beam pipe. The trajectory can be either linear
353 (linear accelerators) or circular (circular or cyclic accelerators). The advantage of the
354 latter ones is that they can accelerate particles many times while keeping them in
355 orbit.

356 Particle accelerators are used in numerous fields ranging from fundamental and
357 material research, cancer treatment to industrial applications, such as biomedicine
358 and material processing. There are several types of accelerators existing: electro-
359 static accelerators, linear accelerators (LINACs), cyclotrons, synchrocyclotrons, syn-
360 chrotrons, synchrotron radiation sources and fixed-field alternating gradient acceler-
361 ators (FFAGs).

362 **The Large Hadron Collider** (LHC, figure 1.2) at CERN is the largest particle
363 collider in the world. It is a 27 km long circular machine set up in a tunnel deep under
364 the surface (ranging from 50 to 175 m). It accelerates two proton beams to the energy
365 of 6.5 TeV per beam before it makes them to collide with each other at four different
366 points around its circumference. The LHC was build between 1998 and 2008 and was
367 first successfully started in 2010 and operated stably until 2013 when it underwent a
368 two years long upgrade. They restarted its operation at the beginning of 2015. The
369 hair-thin particle beams travel inside two evacuated pipes with a \sim 5 cm radius. Coils
370 made up of a superconductive material are wound up around the pipes in special
371 patterns. When they are cooled down to -271 °C using liquid helium, they become
372 superconductive - the resistivity of the material drops significantly, minimising the
373 heat dissipation despite high electric currents. These produce strong magnetic fields

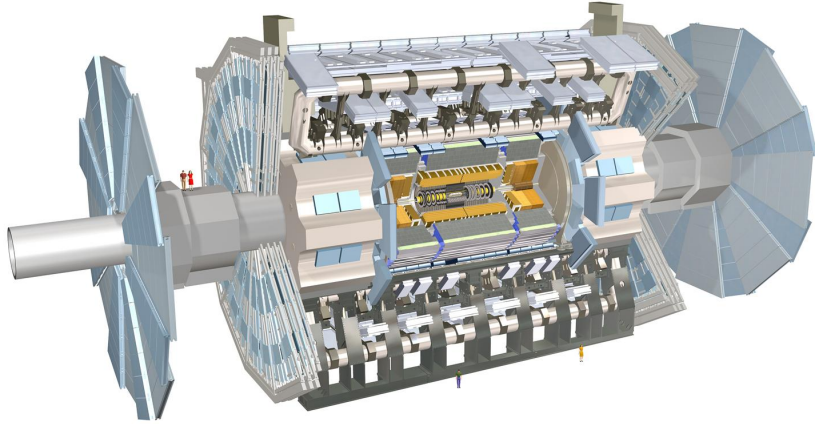


Figure 1.3: The ATLAS Experiment [38]

which bend the particles and keep them in a circular trajectory. The particles are accelerated when traversing the radiofrequency (RF) cavities with the RF frequency of 400 MHz. This oscillating frequency creates buckets – compartments for bunches of highly energetic particles – which are 2.5 ns long. Only one out of ten buckets is being filled, so the bunches are spaced at 25 ns. This defines the machine’s clock as well as the maximum rate of collisions - the bunches travelling in the opposite direction will cross at the intersections up to 40 million times per second. Currently around 20 collisions occur during every bunch crossing, making the maximum collision rate of 10^9 per second. The number of collisions will further increase in the next years, when they will increase the number of particles in every bunch and decrease the transverse spread of the bunches – squeeze them, therefore increase their density and the collision probability.

1.1.3 The ATLAS experiment

ATLAS (short for A Toroidal Lhc ApparatuS, figure 1.3) [] is a particle physics experiment at CERN. Its purpose is to verify current theories and search for new discoveries by observing and analysing high energy proton-proton collisions produced by the LHC. It is the biggest experiment at CERN by dimensions (45 m in length and 26 m in height) and the number of people involved (more than 3000 physicists and engineers). The ATLAS detector consists of many detectors, each designed to measure a specific property of the particles and photons produced during the collision. The closest to the collision point is the Inner Detector (ID), which consists of several layers of highly spatially segmented semiconductor sensors. These can record the path of the individual particles and photons. In addition, a strong magnetic field of 2 T curves the

1.1. FUNDAMENTAL RESEARCH

397 paths of the charged particles, which in turn allows the ID to identify an individual
398 particle's charge and momentum. The next two parts are the electromagnetic and tile
399 calorimeter. These detectors weigh a few thousand tonnes and measure the energy of
400 the particles that are stopping in the bulk. The only particles that make it through
401 the calorimeters are muons. These are detected by the Muon Spectrometer, a set of
402 large plates placed all around the inner layers. Last is the superconductive magnet,
403 which provides the magnetic field through the whole of ATLAS except the ID, which
404 already has its own magnets. To sum up, the Inner Detector measures the charge and
405 momenta of the particles and photons, the calorimeters measure their energies, the
406 Muon Spectrometer measures muons and the magnets provide magnetic fields, which
407 curve the trajectories of the charged particles, facilitating the charge and momentum
408 measurements.

409 A complex Trigger and Data Acquisition system (TDAQ) is in place to distribute
410 the clock signal, configure the detectors, trigger them and handle the output data.
411 They are then stored at the CERN computer centre and distributed across the globe
412 by means of the GRID – a cloud-like distributed data system.

413 The ATLAS detector has been designed to measure every collision taking place in
414 its core. With 25 ns between collisions, this makes up 40 million collisions per second.
415 In reality, the maximum achievable rate is about 300 kHz. The recorded collision
416 is called an event. Every event holds information from all the detector channels
417 within ATLAS. With $\sim 10^6$ channels, an event size is approximately 10 MB. At the
418 maximum achievable rate this means a data rate of up to 3 TB/s. Unfortunately
419 no supercomputer existing today is capable of reading in and saving such a huge
420 amount of data. This is where the trigger logic comes into play. It is programmed to
421 decide in the order of tens of nanoseconds after an event whether this is a potentially
422 interesting event or not. If so, it triggers the readout of the whole detector. This way,
423 the recorded event rate is reduced from 300 kHz to ~ 500 Hz, which is already within
424 the limits of the computing centre's capabilities.

425 1.1.4 Atominstitut, Vienna

426 Atominstitut (ATI) [2], an institute for atomic and subatomic physics, was estab-
427 lished in 1958 in Vienna as an inter-university institute. It currently houses around
428 200 people involved in a broad range of research fields: quantum, particle, neutron,
429 nuclear, radiation and reactor physics, quantum optics etc. Its central facility is a
430 TRIGA MARK II neutron reactor (described in detail below).

431 As of 2002 the ATI is part of the University of Technology in Vienna.

432 **TRIGA MARK II neutron reactor** [12] is a reactor of a swimming-pool type
433 used for training, research and isotope production. It is one of 40 such reactors
434 worldwide, produced by an californian company General Atomic in the early 60's. It
435 is capable of continuous operation at a maximum output power of 250 kW. The reactor
436 core consists of 3 kg of 20 % enriched uranium (^{235}U). The fuel moderator rods are
437 mostly made up of zirconium with low percentage of hydrogen and uranium. Both the

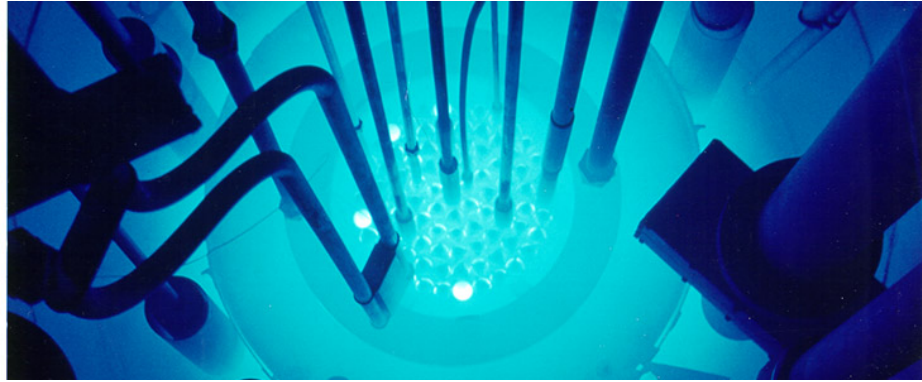


Figure 1.4: The TRIGA MARK II neutron reactor [15]

438 core and the rods are immersed in a pool of water as shown in figure 1.4 for the purpose
439 of cooling and radiation protection. The surrounding concrete walls are 2 m wide
440 with an added graphite layer for improved shielding. Four main experimental beam
441 holes are placed radially through the walls. All exits are heavily shielded to prevent
442 radiation damage to people, but still leaving enough space to set up experiments.
443 Apart from the beam holes, there are several other exits and components, e.g. a
444 thermal column for generation of thermal (low energetic) neutrons.

445 1.1.5 n-ToF

446 n-ToF (or neutron time-of-flight) [9] is a scientific collaboration with the aim of study-
447 ing neutron-nucleus interactions. Over 30 institutes and universities are currently
448 active members of this collaboration, among them Atominstitut in Vienna. n-ToF
449 is also a facility at CERN where the experiments are carried out in a 200 m long
450 experimental area. The knowledge stemming from the experimental results can then
451 be applied in various fields ranging from nuclear technology and cancer therapy to
452 astrophysics.

453 A pulsed beam of highly energetic protons (20 GeV/c) is produced by the Proton
454 Synchrotron (PS) and aimed at a fixed lead spallation target. Each proton hitting
455 the target produces around 300 neutrons of various energies. Initially highly energetic
456 neutrons are slowed down by the target and by a slab of water placed behind it. This
457 broadens their energy spectrum, which then ranges from meV (thermal neutrons) to
458 GeV (fast neutrons). The neutrons are then collimated and sent through a 185 m
459 long evacuated pipe to the experimental area, where they are made to collide with
460 another target or a sample. The radiation resulting from the collisions is detected by
461 a set of dedicated detectors around the interaction point (seen in figure 1.5). Having
462 different energies, neutrons travel with different speeds, highly energetic ones reaching
463 the target faster than those with low energies. Analysis of the collisions with a precise
464 timing allows us to determine the interaction probability with sample material as a
465 function of incident neutron energy.

1.2. PARTICLE DETECTORS

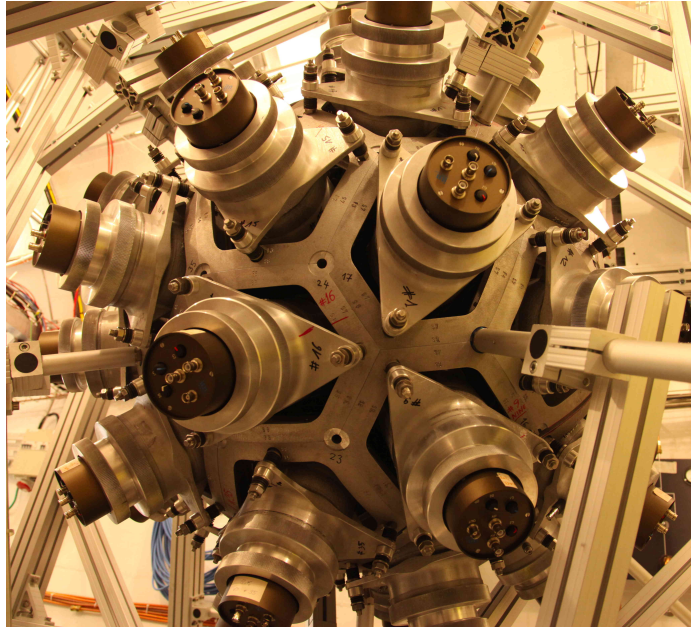


Figure 1.5: The calorimeter in the n-ToF area [19]

466 1.2 Particle detectors

467 Particle detectors, or radiation detectors, have first come into use at the end of the
468 19th century. At that time Wilhelm Röntgen used a photographic plate onto which
469 he shone X-rays. Soon after, in 1912, Victor F. Hess discovered cosmic rays during
470 a balloon flight. This paved the way for development of particle detectors. A cloud
471 chamber was designed – a chamber filled with a supersaturated vapour of water or
472 alcohol. If a highly energetic particle traversed the chamber, the mixture ionised,
473 creating condensation nuclei. These traces were visible and were photographed. All
474 the subsequent particle detectors relied on the same principle of interaction between
475 the particles – ionisation. The bubble chamber invented in 1952 used a superheated
476 transparent liquid – a liquid heated just below its boiling point. A particle ionised
477 the liquid, forming microscopic bubbles along its trajectory. Then followed the spark
478 chamber and the wire chamber where the particle ionised the gas, causing a spark
479 between two parallel plates at a high potential difference. These are nowadays used in
480 museums as showcases. Next were ionisation chambers, which measured the induced
481 current of the free ionised charges moving in an externally applied electric field.
482 Finally in the 1960s, semiconductor detectors were introduced. Their principle of
483 operation is similar to that of an ionisation chamber, with the difference that a semi-
484 conductive material is used as an ionisation medium instead of gas. Every technology
485 has its advantages and disadvantages. Nowadays an ensemble of several types of
486 detectors is used as a single detector system. There are many considerations that
487 need to be taken into account when designing such a system: detector geometry,
488 segmentation, event rate, efficiency, readout, support structures, cabling, cooling,
489 cost etc.



Figure 1.6: The Insertable B-Layer – a silicon particle tracker installed in the ATLAS experiment in 2014 [34]

On large, particle detectors can be divided in two groups: tracking detectors and calorimeters. The former are designed to measure trajectories (momentum) of particles and photons with a minimal impact on their flight path or energy. They must be built with a high spatial resolution and lightweight. Typically they are semiconductor detectors. The calorimeters, on the other hand, measure the energy of the particles/photons by stopping them. This means they need to be heavy and dense. A typical physics experiment nowadays would consist of a tracking detector enclosed by a calorimeter. This way both the momentum and energy are derived, measuring energy, charge and trajectory of every particle/photon.

1.2.1 Semiconductor detectors

Semiconductor particle detectors are devices that use a semiconductor for detecting radiation. They work on the principle of an ionisation chamber. An incident particle or a photon ionises the atoms in the crystal lattice. The freed charges start drifting in an externally applied electric field, inducing current on the electrodes. The charges are freed if the deposited energy is higher than the energy band gap. There are many semiconductor materials currently existing, each with a different band gap. Germanium (Ge), for instance, has a band gap of 0.67 eV, which means that most of the electrons at the room temperature will already be in an excited state. Diamond's 5.5 eV band gap, on the other hand, is too high for the visible light to excite the electrons. Silicon with an energy gap of 1.12 eV has been the material of choice for the majority of semiconductor applications, including radiation detectors. Semiconductor detectors are most widely used for tracking applications, like the Insertable B-Layer (see figure 1.6) [39], which was installed in ATLAS Experiment in 2014. They can be produced into light and thin sensors, they have a fast signal response, they are highly efficient and highly resistant to radiation damage. They also allow for a fine spatial segmentation to increase the tracking resolution. Semiconductor sensors come

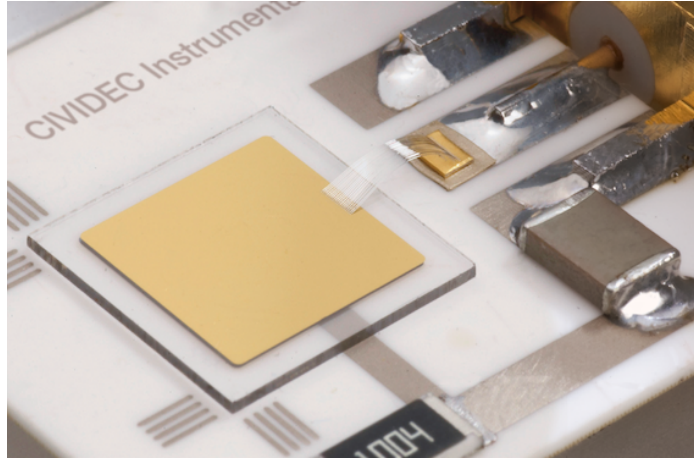


Figure 1.7: A pCVD diamond pad detector [23]

in several configurations. The simplest type is a pad – a single plate measuring 25 mm². Pads are used for particle counting and radiation monitoring. Next is a strip detector, a more finely segmented detector made out of long parallel sensing areas or strips. Each strip has its own signal line for readout. Usually the strip detectors are used in pairs – one detector is placed on top of the other at a 90° angle to increase spatial resolution in both axes. The third and the most finely segmented is a pixel detector, consisting of a 2D array of independent sensing areas. In tracking applications, pixel detectors are used where the detection resolution is the highest. Due to their high production cost and a high number of signal channels, they can only cover limited areas. Strip detectors are cheaper to produce and can be used to cover larger areas in several consecutive layers.

1.2.2 Diamond sensors

Diamond has been known for over two millennia, valued for its mechanical properties and its appearance. When we learnt how to synthesise it, diamond found its way to a broad range of industries which exploited its optical and electrical properties. The discovery of the Chemical Vapour Deposition (described below) as a new synthesis process gave rise to a range of new applications. From being used on machines for drilling tunnels it found its way to electronics, high-power switching devices, electrochemical systems, radiation sensors, quantum computing etc. Recently it was found that it also exhibits superconductivity. This thesis focuses on the use of diamond for radiation detection. Compared to a natural diamond, a detector-grade CVD diamond has almost no impurities (foreign atoms like nitrogen or boron). The carbon lattice is very uniform, which improves its electrical properties. It is an almost perfect insulator, but behaves as a semiconductor under certain conditions. Compared to silicon, the most widely used semiconductor material for radiation detection, it has many advantages, which are described in detail in chapter ???. Figure 1.7 shows a diamond pad detector produced by CIVIDEC Instrumentation GmbH.

543 **Chemical vapour deposition** (CVD) [] is a process where a material is deposited
544 from a gas onto a substrate, involving chemical reactions. It is often carried out un-
545 der high pressure and high temperatures. It takes place in enclosed chambers called
546 furnaces with careful regulation of the temperature, pressure and gas mixture. Syn-
547 synthetic diamond is grown at 700–900 °C with a mixture of hydrogen and methane
548 gas. At this temperature the molecules dissociate into carbon and hydrogen atoms.
549 The carbon atoms are the building blocks and are deposited on the surface of the
550 substrate. However, they would rather form graphitic bonds as they are more stable
551 than diamond bonds. Nevertheless, with high pressure, high temperature and with
552 added abrasive atomic hydrogen, the graphitic double bonds are broken up and con-
553 verted into diamond bonds. The speed of the growth can be anywhere between 0.1
554 and 10 micron per hour. The detector grade samples are grown at a rate of the order
555 of 1 micron per hour. They can grow up to several millimetres in thickness. Their
556 width, however, depends entirely on the substrate used. Diamond can be deposited
557 on various materials: diamond, silicon, tungsten, quartz glass etc. The substrate
558 material must be able to withstand the high temperatures during the CVD process.
559 The diamond substrate does not need any surface pre-treatment. Carbon atoms form
560 bonds with atoms in the existing crystal structure. This is the homoepitaxial growth
561 where the newly deposited atoms retain the orientation of the structure in the sub-
562 strate. Other non-diamond substrates, however, need to be pre-treated, usually by
563 being polished using diamond powder. Some powder particles remain on the surface,
564 acting as seeds for the growth of small crystals or grains. These grains grow and
565 at some point merge with the adjacent ones, making up a compact material. The
566 lower side is later polished away. These diamonds are called *polycrystalline* (pCVD)
567 whereas those grown on a diamond substrate are *single crystal* (sCVD) diamonds.
568 The area of the former can be large - up to 0.5 m² or more compact 15 cm² in the case
569 of detector grade diamonds. The sCVD diamonds, on the other hand, can currently
570 only measure up to 1.5 cm².

⁵⁷¹ Chapter 2

⁵⁷² Signal formation in diamond

⁵⁷³ This chapter describes the fundamentals of signal formation in a diamond sensor, as
⁵⁷⁴ well as its use as a particle detector. This is described in section 2.1 where energy
⁵⁷⁵ deposition and signal formation mechanism are explained. Then some examples of
⁵⁷⁶ ionisation are shown. Later, some of the internal lattice defects that effect the signal
⁵⁷⁷ are described. The final section contains the description of the remaining part of the
⁵⁷⁸ signal chain – signal amplifiers, digitisers and devices for signal processing. Noise
⁵⁷⁹ contributions are discussed at every stage of the signal chain.

⁵⁸⁰ There are many types of radiation sensors existing, but in this chapter we will
⁵⁸¹ focus on semiconductors, in particular on diamond sensors. Diamond is a good insu-
⁵⁸² lator, but behaves as a semiconductor in certain cases. In fact, the main principle of
⁵⁸³ operation is the same for diamond, silicon and other semiconducting materials – ion-
⁵⁸⁴ isation. An incident highly energetic charged particle ionises the atoms in the lattice,
⁵⁸⁵ freeing electrons and holes, which then drift towards positively and negatively charged
⁵⁸⁶ electrodes, inducing an electrical signal. A sensor converts the energy deposited by a
⁵⁸⁷ particle or a photon to an electrical signal.

⁵⁸⁸ Silicon is currently considered as the industry standard for particle detection.
⁵⁸⁹ However, there are some disadvantages of using silicon instead of diamond, due to
⁵⁹⁰ significant differences in the material properties. In particular, the properties of silicon
⁵⁹¹ change significantly with radiation. For instance, the leakage current increases, which
⁵⁹² in turn increases shot noise and can lead to a thermal runaway. In addition, due to
⁵⁹³ induced lattice defects, which act as charge traps, its charge collection efficiency starts
⁵⁹⁴ dropping quickly. Both are true for diamond as well, but on a much smaller scale.

⁵⁹⁵ Table 5.2 compares the properties of diamond and silicon. Some of these values
⁵⁹⁶ will be revisited and used in the course of this thesis.

Property	Diamond	Silicon
Band gap energy E_g (eV)	5.5	1.12
Electron mobility μ_e ($\text{cm}^2 \text{ V}^{-1} \text{ s}^{-1}$)	1800	1350
Hole mobility μ_h ($\text{cm}^2 \text{ V}^{-1} \text{ s}^{-1}$)	1200	450
Breakdown field (V cm^{-1})	10^7	3×10^5
Resistivity ($\Omega \text{ cm}$)	$> 10^{11}$	2.3×10^5
Intrinsic carrier density (cm^{-3})	$< 10^3$	1.5×10^{10}
Mass density (g cm^{-3})	3.52	2.33
Atomic charge	6	14
Dielectric constant ϵ	5.7	11.9
Displacement energy (eV/atom)	43	13 – 20
Energy to create an e-h pair (eV)	13	3.6
Radiation length (cm)	12.2	9.6
Avg. signal created/ μm (e)	36	89

597

598

Table 2.1: Comparison diamond – silicon []

599 **2.1 Principles of signal formation in semiconduc-
600 tors**

601 There are several ways the particles can interact with the sensor: via bremsstrahlung [],
 602 elastic or inelastic scattering (e-h pair production). Bremsstrahlung is radiation cre-
 603 ated when a particle is deflected from its original path due to attraction of the core of
 604 an atom. This is in principle an unwanted effect in semiconductors as it decreases the
 605 spatial resolution of the sensor. Elastic scattering is deflection of the particle's tra-
 606 jectory without energy loss. Inelastic scattering is the interaction through which the
 607 atom is ionised and an electron-hole pair is created. All these effects are competing
 608 and are dependent on the particle's mass, momentum etc.

609 Semiconductors are materials that are conductive only under specific
 610 conditions. They can be made up of atoms with four electrons in their valence band
 611 (e.g. silicon–Si, carbon–C or germanium–Ge) or as combinations of two or more
 612 different materials (e.g. gallium arsenide–GaAs). The atoms in the lattice form
 613 valence bonds with adjacent atoms, making solid crystal structures. These bonds
 614 can break up if sufficient external energy is applied. The electron that was forming
 615 the bond is kicked out, leaving behind a positively charged ion with a vacancy in its
 616 valence band (see figure 2.1a). A free electron-hole pair is thus created. The free
 617 electron travels through the crystal until it is caught by another hole. Similarly, the
 618 hole also “travels” through the material. Its positive charge attracts a bound electron
 619 in the vicinity, which breaks from the current bond and moves to the vacancy, leaving
 620 a new hole behind. The process continues, making it look like the vacancy – the hole
 621 – is traveling through the material.

622 The electrons need to absorb a certain energy to get kicked out of the atomic
 623 bond – to get ionised. The minimal energy required to excite (ionise) an electron in
 624 a semiconductor is equal to the energy gap E_g . Typical widths of the forbidden gap
 625 are 0.7 eV in Ge, 1.12 eV in Si, 1.4 eV in GaAs and 5.5 eV in Di. Due to the small

2.1. PRINCIPLES OF SIGNAL FORMATION IN SEMICONDUCTORS

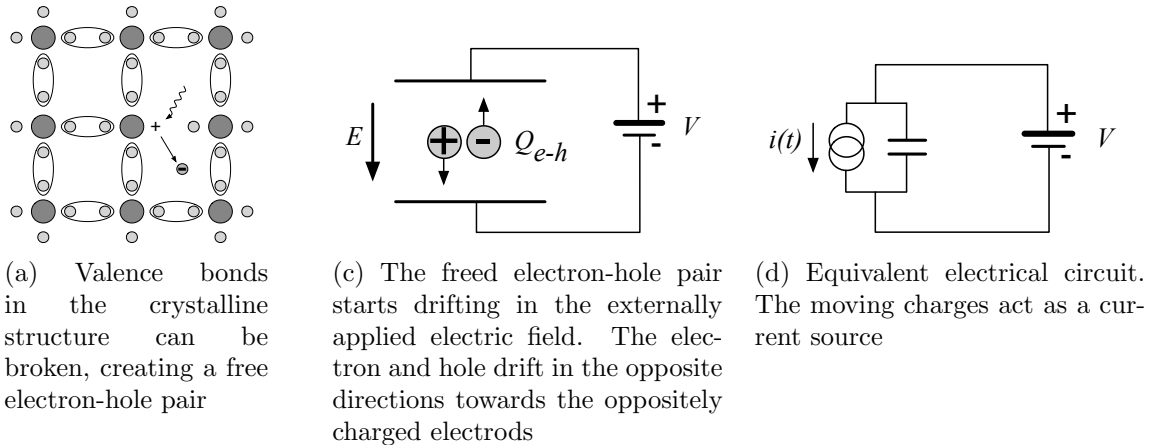


Figure 2.1: In the equivalent electrical circuit diagram, electron-hole creation and drift can be modelled as a current source with a capacitor in parallel

band gap in semiconductors some electrons already occupy the conduction band at room temperature (RT). The intrinsic carrier concentration n_i in semiconductors is given as

$$n_i = T^{3/2} \cdot \exp\left(-\frac{E_g}{2kT}\right) \quad (2.1)$$

wherein $k = 1.381 \times 10^{-23} \text{ m}^2 \text{ kg s}^{-2} \text{ K}^{-1}$ is the Boltzmann constant and T is the temperature.

If an external electric field is applied to the crystalline structure, the free electrons and holes drift toward the positive and negative potential, respectively (see figure 2.1c). While drifting, the charges couple with the electrodes, inducing current in the circuit, which is explained by the Shockley–Ramo theorem (see subsection below). The charges recombine upon reaching the electrodes.

Energy deposition of α radiation and heavy ions

Energy deposition of β and γ radiation The mean energy loss of a particle traversing the detector with respect to its momentum is given with the the Bethe-Bloch equation []:

$$-\left\langle \frac{dE}{dx} \right\rangle = \frac{4\pi}{m_e c^2} \cdot \frac{n z^2}{\beta^2} \cdot \left(\frac{e^2}{4\pi\epsilon_0} \right)^2 \cdot \left[\ln \left(\frac{2m_e c^2 \beta^2}{I \cdot (1 - \beta^2)} \right) - \beta^2 \right] \quad (2.2)$$

The resulting function for a muon (a heavy electron) is shown in figure 2.2. At the momentum of around 300 MeV/c the particle deposits the lowest amount of energy. That is called a minimum ionising particle or a MIP.

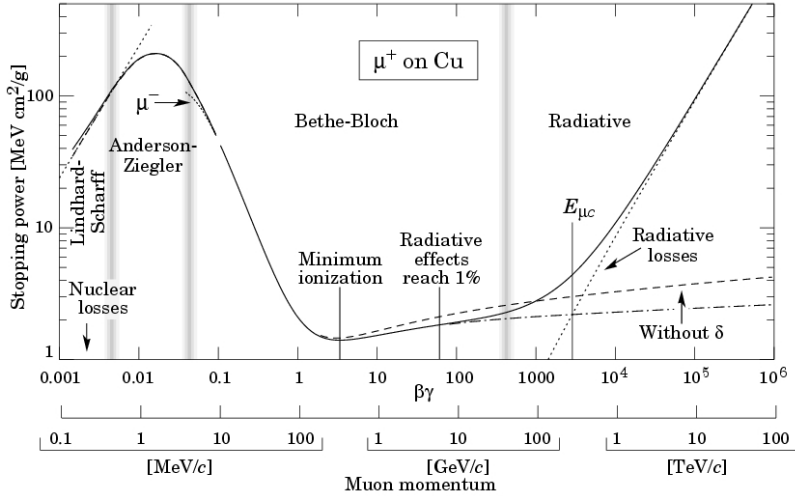
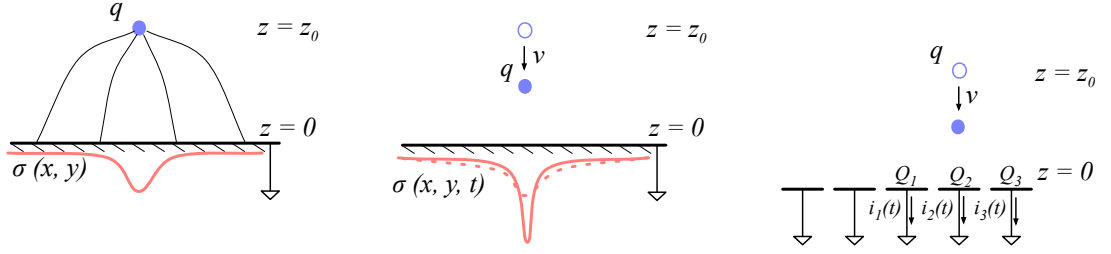


Figure 2.2: Stopping power for muons according to the Bethe-Bloch formula []



(a) Newly created point charge couples with the conductive plane
 (b) When the charge drifts, the charge density in the plane changes
 (c) The changing charge density in the small regions of the plane induces current

Figure 2.3: A point-like charge inducing current in a conductive plane

2.1.1 Signal induction by moving charges

The book [17] gives a simple introduction to understanding signal induction in a conducting plane by a point-like charge. The idea behind it lies in the coupling of the charge with the electrode. The electrode can be in this case modelled as an infinite conducting plane. When the point charge q is created (e.g. an electron-hole pair created via ionisation), its electrostatic field lines immediately couple with the electrode, as seen in figure 2.3a. The electric field on the metal surface due to a point-like charge q at the distance z_0 equals

$$E_z(x, y) = \frac{qz_0}{2\pi\epsilon_0(x^2 + y^2 + z_0^2)^{\frac{3}{2}}} \quad E_y = E_z = 0. \quad (2.3)$$

A mirror charge appears on the conducting plane, with a charge density distribution

$$\sigma(x, y) = \epsilon_0 E_z(x, y) = \frac{qz_0}{2\pi(x^2 + y^2 + z_0^2)^{\frac{3}{2}}}. \quad (2.4)$$

2.1. PRINCIPLES OF SIGNAL FORMATION IN SEMICONDUCTORS

652 The charge density integrated over the whole plane gives the mirror charge Q , which
 653 has the opposite value of the point charge q :

$$Q = \int_{-\infty}^{\infty} \int_{-\infty}^{\infty} \sigma(x, y) dx dy = -q. \quad (2.5)$$

654 Now we segment the plane into infinitely long strips with a width w whereby each
 655 of the strips is grounded (figure 2.3c). With the charge density distribution 2.4, the
 656 resulting mirror charge on a single strip Q_2 directly below the point charge ($x =$
 657 $0, y = 0$) will be equal to

$$Q_2(z_0) = \int_{-\infty}^{\infty} \int_{-w/2}^{w/2} \sigma(x, y) dx dy = -\frac{2q}{\pi} \arctan\left(\frac{w}{2z_0}\right) \quad (2.6)$$

658 If the charge starts moving towards the conducting plane, the mirror charge density
 659 distribution also changes (see figure 2.3b). This results in the $Q_2[z_0(t)]$ to change
 660 with time, inducing an electric current $i_n(t)$:

$$i_n(t) = -\frac{d}{dt} Q_2[z_0(t)] = -\frac{\partial Q_2[z_0(t)]}{\partial z_0} \frac{\partial z_0(t)}{\partial t} = \frac{4qw}{\pi[4z_0(t)^2 + w^2]} v. \quad (2.7)$$

661 The movement of the point-like charge therefore induces current in the conducting
 662 plane. The induced current is linearly dependent on the velocity of the point-like
 663 charge.

664 W. Shockley [42] and S. Ramo [40] independently proposed a theory which explains
 665 how a moving point charge induces current in a conductor. The Shockley-Ramo
 666 theorem can therefore be used to calculate the instantaneous electric current induced
 667 by the charge carrier or a group of charge carriers. It can be used for any number of
 668 electrodes. It states that the current $I_n^{\text{ind}}(t)$ induced on the grounded electrode n by
 669 a point charge q moving along a trajectory $\mathbf{x}(t)$ equals

$$I_n^{\text{ind}}(t) = -\frac{dQ_n(t)}{dt} = -\frac{q}{V_w} \nabla \Psi_n[\mathbf{x}(t)] v(t) = -\frac{q}{V_w} E_n[\mathbf{x}(t)] v(t), \quad (2.8)$$

670 where $\mathbf{E}_n(\mathbf{x})$ is the electric field in the case where the charge q is removed, electrode n
 671 is set to voltage $V_w = 1$ and all other electrodes are grounded. $\mathbf{E}_n(\mathbf{x})$ is also called the
 672 *weighting field* of electrode n and is defined as the spatial differential of the *weighting*
 673 *potential*: $\mathbf{E}_n(\mathbf{x}) = \nabla \Psi_n(\mathbf{x})$. In the case of two parallel electrodes, the weighting field
 674 is $E_w = -\frac{d\Psi}{dx} = -1/d$, where d is the distance between the electrodes. The resulting
 675 induced current is therefore

$$i(t) = \frac{q}{d} v_{\text{drift}}(x, t), \quad (2.9)$$

676 whereby v_{drift} is the drift velocity of the point-like charge and d is the distance between
 677 the electrodes.

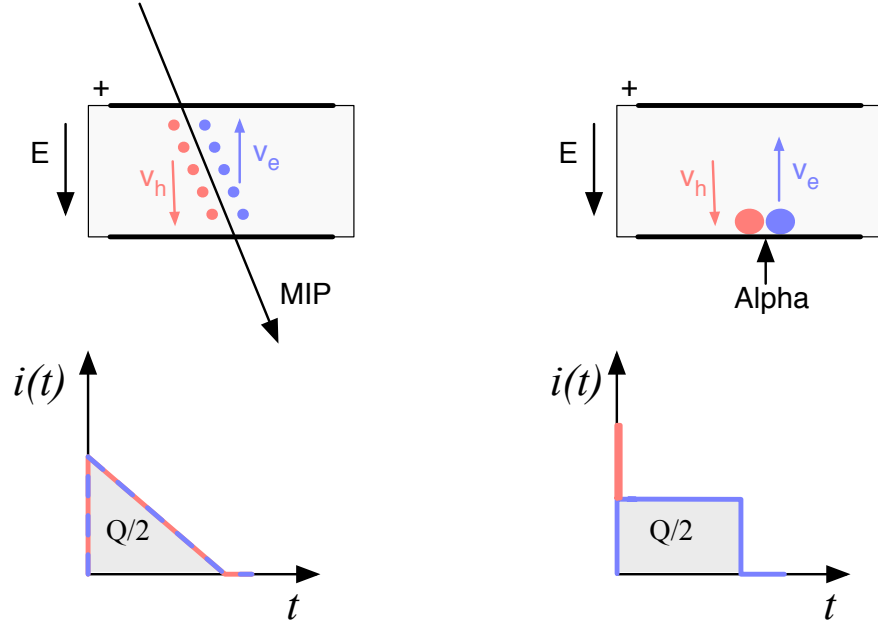


Figure 2.4: Charge carrier drift in diamond for β/γ and for α particles

678 2.1.2 Radiation-induced electrical pulses

679 When a highly-energetic particle travels through the sensor, it interacts with atoms
 680 in the lattice. It ionises the valence electrons, creating electron-hole (e-h) pairs on its
 681 way. It can either deposit only a fraction of its energy and fly exit the sensor on the
 682 other side or it can get stopped in the bulk, depositing all of its energy. A special
 683 case is when it interacts with the core of the atom in the middle of the sensor via
 684 a nuclear interaction. All these various types interactions produce different amounts
 685 and different spatial distributions of e-h pairs. The induced electrical current will
 686 therefore differ for different types of interaction. Two most frequent types are shown
 687 in figure 2.4. The first diagram shows the interaction of a minimum ionising particle
 688 (an electron or a proton) or in some cases a photon, if it is energetic enough. The
 689 electrons and holes are created all along the trajectory of the particle and imme-
 690 diately start drifting towards the positive and negative electrode, respectively. At
 691 the beginning, all charges drift and contribute to the induced current. Those closest
 692 to the electrodes have a very short drift path and recombine quickly, reducing the
 693 induced current. Gradually all the charge carriers recombine. The resulting current
 694 signal is a triangular pulse with a sharp rising edge and a linear falling edge. The
 695 accumulated charge Q_s equals to the sum of the contributions of the positive and
 696 negative charge carriers. The second type of interaction happens when the particle
 697 is stopped in the diamond close to the point of entry. Most of its energy is deposited
 698 in a small volume close to the electrode. A cloud of charge carriers is created and
 699 the charges with the shorter path to the electrode recombine almost instantly. The

2.2. CARRIER TRANSPORT IN A DIAMOND SENSOR

carriers of the opposite charge, however, start drifting through the sensor to the other electrode. In an ideal diamond sensor, their velocity is constant throughout the drift up until they recombine on the other side. The contribution of the first charge cloud is a peak with a short time. The cloud drifting through the sensor, on the other hand, induces a current signal with a flat top. The resulting signal has a shape of a rectangle, with a spike in the beginning. This spike is filtered out in a real device because it is too fast for the electronics existing currently. The accumulated charge Q_s is equal to a half of the deposited charge by the stopped particle.

The two aforementioned types of interactions have well defined signal responses. Nuclear interactions on the other hand yield various results. The resulting signal shape depends on the decay products of the interaction – they can be α , β or γ quanta, inducing a mixed shaped signal.

2.1.3 Signal charge fluctuations

Two of the important sensor characteristics are the magnitude of the signal and the fluctuations of the signal at a given absorbed energy. They determine the relative resolution $\Delta E/E$. For semiconductors the signal fluctuations are smaller than the simple statistical variance $\sigma_Q = \sqrt{N_Q}$, where N_Q is the number of released charge pairs (ratio between the total deposited energy E_0 and the average energy deposition E_i required to produce an electron-hole pair). [2] shows that the variance is $\sigma_Q = \sqrt{FN_Q}$, where F is the Fano factor [2] (0.08 for diamond and 0.115 for silicon [2]). Thus, the variance of the signal charge is smaller than expected, $\sigma_Q \approx 0.3\sqrt{N_Q}$. The resulting intrinsic resolution of semiconductor detectors is

$$\Delta E_{FWHM} = 2.35\sqrt{FEE_i} \quad (2.10)$$

wherein $E_i(Si) = 3.6$ eV and $E_i(C) = 13$ eV. E.g., for an α particle with energy $E_\alpha = 5.486$ MeV the calculated resolution in diamond is equal to $\Delta E_{FWHM} = 5.6$ keV. This defines the maximum achievable resolution for energy spectroscopy with semiconductors. Figure 2.5 shows the calculated energy resolution function for silicon and diamond.

2.2 Carrier transport in a diamond sensor

This section describes the carrier transport phenomena in diamond. This theory provides the basis for discussion about the measurements in chapter ??.

Free charge carriers in a semiconductor get thermally excited and scatter in random directions with a thermal velocity v_{th} [2]. Their integral movement due to thermal excitation equals zero. Their transport is instead by means of drift and diffusion. Diffusion is caused by the concentration gradient. In its presence the carriers tend to scatter in the direction of the lower concentration. Drift on the other hand is caused by an externally applied electrical field. In that case the carriers move in parallel to

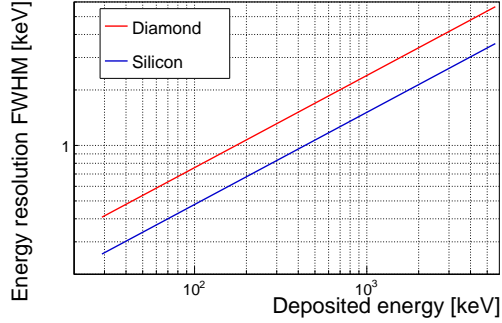


Figure 2.5: Calculated intrinsic energy resolution for silicon and diamond

to the field lines. In a sensor with a high applied field the diffusion contribution is negligible.

Diffusion The concentration profile dissolves with time forming a Gaussian distribution with variance $\sigma(t) = \sqrt{Dt}$ [1].

Drift velocity and mobility The charge carriers drift through the diamond bulk with a drift velocity $v_{\text{drift}}(E)$ [1], which is proportional to the electric field E at low electric fields: $v_{\text{drift}} = \mu E$. The proportionality factor μ is defined as the mobility in $\text{cm}^2\text{V}^{-1}\text{s}^{-1}$. For higher fields, however, the velocity saturates. The final equation for v_{drift} is therefore

$$v_{\text{drift}}(E) = \mu(E)E = \frac{\mu_0 E}{1 + \frac{\mu_0 E}{v_{\text{sat}}}} \quad (2.11)$$

where μ_0 is the low field mobility and v_{sat} is saturation velocity. The drift velocity can be retrieved experimentally via the transit time measured with the Transient Current Technique (TCT). This technique enables the measurement of transit time t_t of the carriers through the sensor with the thickness d .

$$v_{\text{drift}}(E) = \frac{d}{t_t(E)}. \quad (2.12)$$

The velocities for holes and electrons usually differ. In diamond, the holes travel 30 % faster than electrons [1]. The measurements in chapter ?? empirically confirm this statement.

Velocity saturation At higher drift velocities the carriers lose more energy to the lattice. They induce increasingly more lattice vibrations (phonon transport) with increased velocity. There is a velocity limit above which the carriers cannot reach – velocity saturation. Thesis [1] defines this velocity to be $v_{\text{sat}}^e = v_{\text{sat}}^h = (14.23 \pm 0.12) \times 10^6 \text{ cm/s}$ for both positive and negative charge carriers.

Space charge Poisson's equation shows that

$$\frac{d^2\Phi(x)}{dx^2} = \frac{dE(x)}{dx} = \frac{\rho(x)}{\epsilon} \quad (2.13)$$

2.2. CARRIER TRANSPORT IN A DIAMOND SENSOR

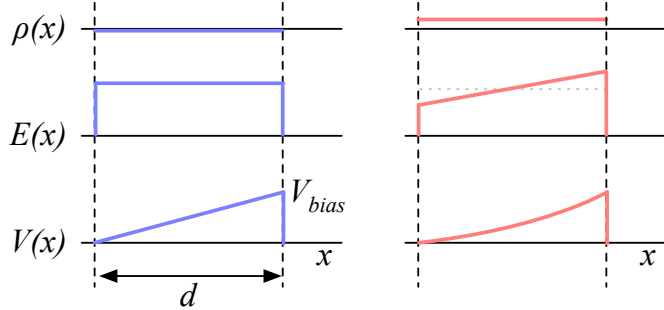


Figure 2.6: Introduction of space charge in the diamond bulk. The induced current signal is proportional to the effective electrical field. d is the thickness of the diamond sensor.

where $\rho(x)$ is the space charge distribution, E is the electrical field and Φ is the voltage potential. In an ideal diamond, the externally applied high voltage potential on the two electrodes decreases linearly through the bulk. The electrical field is therefore constant throughout the sensor and the space charge distribution across it equals 0. However, in some cases space charge is introduced in the bulk, uniformly or non-uniformly. It can do so by means of trapping of charge carriers in the non-uniformities in the lattice or it can already be introduced during the production of the diamond material. The space charge can be either permanent or changing – sometimes it is possible to reduce it by means of priming. All in all, it is very important to reduce it because it affects the shape of the electrical signal. Since the drift velocity of the charge carriers is proportional to the electrical field, the charges change their velocity while drifting through the space charge region. Figure 2.7 compares the voltage potential, electrical field, space charge for an ideal sensor and for that with a uniformly distributed positive space charge.

Radiation damage The diamond crystal lattice is very strong and uniform. However, when the highly energetic particles or photons impinge the diamond, they can damage the crystal structure. Figure ?? shows several examples of the lattice damage:

- a) foreign interstitial (e.g. H, Li),
- b, c) foreign substitutional (e.g. N, P, B),
- d) vacancy and
- e) self interstitial.

These non-uniformities – traps – form new energy levels in the forbidden gap. The drifting charge carriers are stopped by these traps, which in effect reduces the induced current. The energy level of the trapped carrier is reduced from the conduction band to the energy level of the trap. Different types of lattice damage have different energy levels. The release time depends on the level (shallow, deep trap).

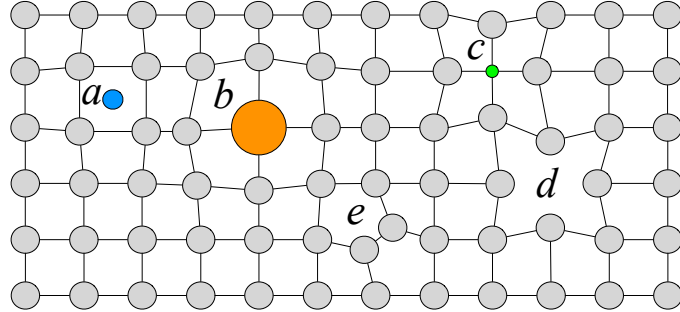


Figure 2.7: Introduction of impurities and non-uniformities into the crystal lattice due to radiation damage.

784 2.3 Electronics for signal processing

785 This section describes the electronics of a detector, starting with a description of
 786 signal amplifiers and then discussing the digitisation and signal processing. All these
 787 stages are necessary to extract information from the sensor. First, the signal has to be
 788 amplified. Then it is digitised and finally processed in a specially designed processor
 789 or a logic unit.

790 2.3.1 Signal preamplifiers

791 The signal charge generated in the sensor by a single highly energetic particle or
 792 photon is of the order of fC. The induced current is ranging between 10^{-8} A (β, γ
 793 radiation) and 3×10^{-7} A (α radiation). Signals as low as these have to be pre-
 794 amplified before processing. Depending on the measurement, several types of signal
 795 amplifiers can be used. The preamplifiers have to be designed carefully to minimise
 796 electronic noise while maximising gain – thus maximising the signal-to-noise ratio
 797 (SNR). In addition, they have to have a high bandwidth limit because the signals
 798 from the diamond sensors are very short. A critical parameter is the total capac-
 799 tance, i.e. sensor capacitance and input capacitance of the preamplifier. The SNR
 800 improves with a lower capacitance. Several types of amplifiers can be used, all of
 801 which affect the measured pulse shape. They behave differently for resistive or ca-
 802 pacitive sources. Given that semiconductors are capacitive sources, we will focus on
 803 these. Two preamplifiers are used most commonly, a current and a charge amplifier.
 804 Both are described below in detail.

805 2.3.1.1 Current-sensitive amplifier

806 Figure 2.8a shows the equivalent circuit of a capacitive source and a current ampli-
 807 fier. An amplifier operates in current mode if the source has a low charge collection
 808 time t_c with respect to the $R_i C_d$ time constant of the circuit. In this case the sensor
 809 capacitance discharges rapidly and the output current i_o is proportional to the in-

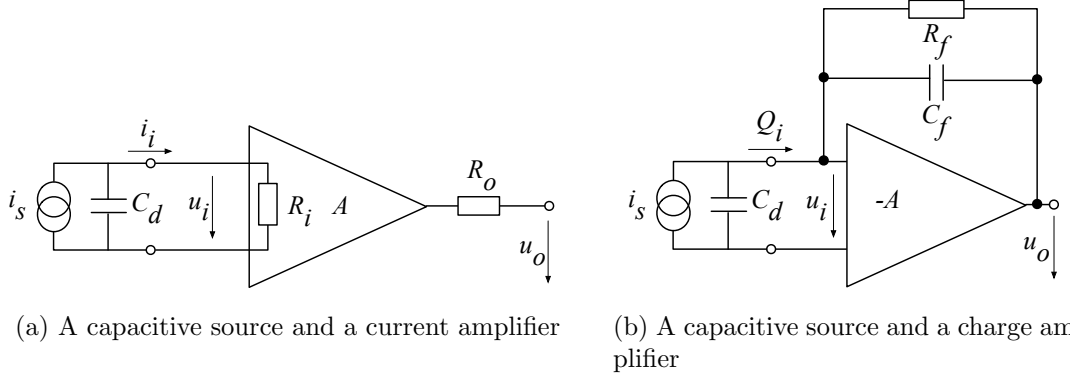


Figure 2.8: Simplified equivalent circuits of a current and charge amplifier

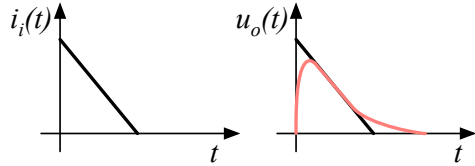


Figure 2.9: Input and output signal of the current amplifier

stantaneous current i_i . The amplifier is providing a voltage gain, so the output signal voltage u_o is directly proportional to the input voltage u_i :

$$u_o(t) = A \cdot R_i \cdot i_s(t). \quad (2.14)$$

The detector capacitance C_{det} together with the input resistance of the amplifier R_i defines the time constant of the signal (see figure 2.9). The higher the C_{det} is, the slower will be the response of the amplifier. For the case of the diamond sensor, which has the capacitance of the order of 2 pF and the input resistance of 50 Ω , the resulting time constant is $\tau = 10^{-10}$ s. This yields the signal rise time $t_r \sim 2.2\tau = 0.22$ ns.

2.3.1.2 Charge-sensitive amplifier

In order to measure integrated charge in the sensor, a feedback loop is added to the amplifier (see figure 2.8b). The feedback can be used to control the gain and input resistance, as well as to integrate the input signal. The charge amplifier is in principle an inverting voltage amplifier with a high input resistance.

In an ideal amplifier the output voltage u_o equals $-Au_i$. Therefore the voltage difference across the capacitor C_f is $u_f = (A + 1)u_i$ and the charge deposited on the capacitor is $Q_f = C_f u_f = C_f(A + 1)u_i$. Since no current can flow into the amplifier, all of the signal current must charge up the feedback capacitance, so $Q_f = Q_i$.

In reality, however, charge-sensitive amplifiers respond much slower than is the duration of the current pulse from the sensor. In addition, a resistor is added to the

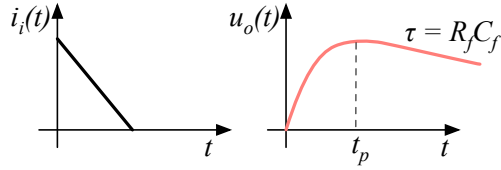


Figure 2.10: Input and output signal of the charge amplifier

828 feedback line in parallel to the capacitor. The resistor and capacitor define the decay
 829 time constant of the pulse (see figure 2.10). This is necessary to return the signal to
 830 its initial state and ready for a new measurement.

831 2.3.1.3 Analogue electronic noise

832 Electronic noise determines the ability of a system to distinguish signal levels. The
 833 analogue signal contains a lot of information, which can quickly be erased or altered
 834 if the signal properties change. It is therefore instrumental to understand the noise
 835 contributions to the signal to qualify the information it carries. There are several
 836 noise contributions, of which the important ones are listed below. The thermal noise
 837 is the dominant noise contribution in the use case for diamond detector signal ampli-
 838 fication and therefore defines the limitations of the detector system. Thermal noise
 839 or Johnson–Nyquist [] noise is generated by the random thermal motion of charge
 840 carriers in the conductor. The frequency range of the thermal noise is from 0 to
 841 ∞ with a more or less uniform distribution. Therefore this is nearly a white noise.
 842 The resulting signal amplitude has a Gaussian distribution. The RMS of the noise
 843 amplitude is defined as

$$u_{\text{RMS}} = \sqrt{4k_B RT \Delta f} \quad (2.15)$$

844 where k_B is the Boltzmann constant, R is the resistance of the conductor, T its
 845 temperature and Δf the frequency range. This equation shows that it is possible to
 846 reduce the noise RMS by either (1) reducing the frequency range, (2) reducing the
 847 resistance of the conductor or (3) cooling the conductor.

848 Contributions of shot noise, flicker noise and burst noise and other types are not
 849 significant relative to the thermal noise. However, the contributions of external factors
 850 can severely deteriorate the signal. This means the noise produced by capacitive or
 851 inductive coupling with an external source, which causes interference in the signal.
 852 These effects can be reduced by shielding the electronics and avoiding ground loops.

853 2.3.2 Analogue-to-digital converters

854 An analogue-to-digital converter (ADC) is a device that converts the analogue elec-
 855 trical signal on the input to its digital representation - a series of digital values. This
 856 involves a quantisation – *sampling* of the signal at a defined sampling period, resulting

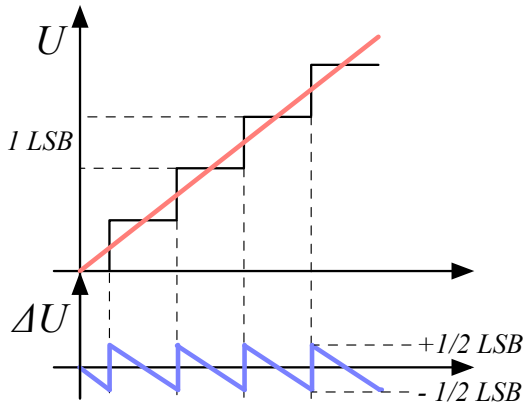


Figure 2.11: Input signal digitisation and quantisation error

in a sequence of samples at a discrete time period and with discrete amplitude values. The resolution of the ADC is the number of output levels the ADC can quantise to and is expressed in bits. For instance, an ADC with a resolution $n = 8$ bit will have the dynamic range $N = 2^n = 256$ steps. The resulting voltage resolution Q_{ADC} at the input voltage range of $V_{\text{ADC}} = \pm 50$ mV is then equal to

$$Q_{\text{ADC}} = \frac{V_{\text{ADC}}}{2^n} = \frac{100 \text{ mV}}{2^8 \text{ steps}} = 0.39 \text{ mV/step}. \quad (2.16)$$

With a sampling period of $t_s = 1$ ns this will produce the sampling rate of $f_s = 1$ GSFS (gigasample per second).

Quantisation error and quantisation noise (or a round-off error) is a contribution to the overall measurement error due to digitisation (rounding). It is defined as a difference between the actual analog value and a digitised representation of this value. The error is defined by the least significant bit (LSB), as seen in figure 2.11. Typically, the input signal amplitude is much larger than than the voltage resolution. Therefore the quantisation error is not directly correlated with the signal and has an approximately uniform distribution []:

$$\Delta Q_{\text{ADC}} = \frac{1}{\sqrt{12}} \text{ LSB} \sim 0.289 \text{ LSB}. \quad (2.17)$$

For the example above the quantisation error will be $\Delta Q_{\text{ADC}} = 0.289 \cdot 0.39 \text{ mV} = 0.11 \text{ mV}$. The error depends strongly on the linearity of the ADC, but this will not be discussed in this document as the devices used have ADCs with a linear response.

2.3.3 Digital signal processing

The digitised signal can be processed to extract useful information. Therefore after the signal amplification and digitisation the signal is routed in a device which handles

877 the analysis. The signal can either be processed immediately (in real time) or it can
878 be saved to a data storage for analysis at a later stage (offline). The devices carrying
879 out the processing can be multipurpose (e.g. Field programmable gate arrays) or
880 dedicated (e.g. application-specific integrated circuits). Each of the two has its
881 advantages and disadvantages, which are listed below.

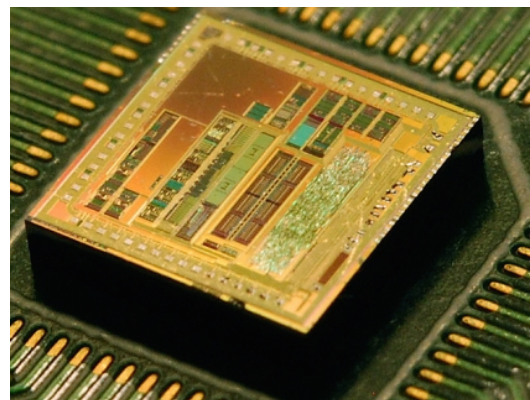
882 **Field programmable gate array** (FPGA) is an integrated circuit designed to be
883 reprogrammable and reconfigured after manufacturing. It consists of a set of logic
884 gates that can be interconnected in numerous combinations to carry out a logic op-
885 eration. Many such logic operations can take place in parallel, making the FPGA a
886 powerful tool for signal processing. FPGAs are often used during system develop-
887 ment or in systems in which the requirements might change with time. They can
888 be reprogrammed in the order of seconds. In addition, the logic design only needs
889 minor changes when migrating to a newer version of the FPGA chip of the same
890 vendor. They also offer faster time-to-market with comparison to application-specific
891 solutions, which have to be developed. On the other hand, the price per part can be
892 significantly higher than for the application-specific solutions. Also, their other major
893 disadvantages are a high power consumption and a relatively low speed. However,
894 today's solutions are capable of clock speeds of the order of 500 MHz. Together with
895 the integrated digital signal processing blocks, embedded processors and other mod-
896 ules, they are already very powerful and versatile. All in all, FPGAs are a good choice
897 for prototyping and limited production, for projects with a limited requirements for
898 speed and complexity.

899 **Application-specific integrated circuit** (ASIC) is an integrated circuit designed
900 for a specific use. The design cannot be modified after chip production, as compared
901 to FPGAs. On the other hand, the ASICs can be optimised to perform a required
902 operation at a high speed and at a low power consumption. In addition, due to the
903 specific design the size of the chip can be much smaller. ASICs can be designed
904 as hybrid chips, containing both a digital and an analog part. To update the chip,
905 the design has to be submitted to a foundry, which produces the new chips with a
906 turnover time of 4—6 weeks. The costs of a submission start at \$ 50 000, but the
907 price per part can be reduced significantly with a high volume. To sum up, ASICs
908 are used for high volume designs with well defined requirements where some stringent
909 constraints in terms of power consumption and speed have to be met.

2.3. ELECTRONICS FOR SIGNAL PROCESSING



(a) Xilinx Virtex 5 FPGA [13]



(b) ASIC [1]

Figure 2.12: An example of an FPGA and an ASIC chip

⁹¹⁰ Chapter 3

⁹¹¹ Experimental results

⁹¹² *Diamond irradiation study*

⁹¹³ This chapter contains the measurement results of data taken with diamond sensors.
⁹¹⁴ First the measurement setup is described (section 3.1). Then the measured particle
⁹¹⁵ spectra are shown in 3.2. This is followed by a study of effects of irradiation damage
⁹¹⁶ on the electrical signal of the diamond detector and its lifetime. The last section
⁹¹⁷ shows the results of the measurements of irradiated diamond samples at cryogenic
⁹¹⁸ temperatures. The aim of these studies is to find the operational limitations of dia-
⁹¹⁹ mond detectors for spectroscopy and tracking applications. The studies compare the
⁹²⁰ experimentally acquired data with the theory from the previous chapter and define
⁹²¹ limitations of the diamond detectors in terms of noise, radiation and temperature.

⁹²² Diamond sensors are mainly used for two types of measurements: particle counting
⁹²³ and spectroscopy. The first type of measurements depends on the sensor's efficiency –
⁹²⁴ the ability to detect all or at least a known percentage of radiation quanta (particles
⁹²⁵ or photons) that hit it. The energy of the radiation is not so important; what bears
⁹²⁶ the information is the rate and the spatial distribution. Here the radiation does
⁹²⁷ not necessarily stop in the bulk, but rather continues its way. In spectroscopy, on
⁹²⁸ the other hand, the idea is that a particle stops within the sensor, depositing all
⁹²⁹ its energy, which is then measured via the freed charge carriers. The aim of the
⁹³⁰ experiments described in this chapter is to:

- ⁹³¹ 1. Quantify the efficiency of the sCVD diamond in counting mode,
- ⁹³² 2. Quantify the degradation of efficiency with respect to the received radiation
⁹³³ dose,
- ⁹³⁴ 3. Quantify the macroscopic effects on charge carrier behaviour with respect to
⁹³⁵ the received radiation dose and
- ⁹³⁶ 4. Define limitations for its use in spectroscopy.

⁹³⁷ The results discussed here show that there are several limitations for using diamond as
⁹³⁸ a measurement device. All of them need to be taken into account for the measurement

3.1. MEASUREMENT SETUP

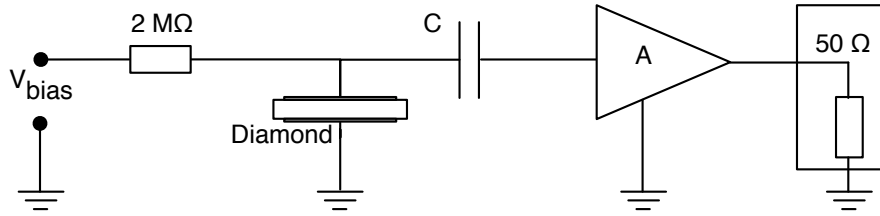


Figure 3.1: Diagram of a diamond detector readout chain.

device to perform reliably and stably. The first step is to build a setup that is insensitive to external electromagnetic interferences and minimises electrical noise in the system. The setup needs to be calibrated before use. Then, the measurement conditions have to be defined, such as the temperature, the type of radiation and its flux. This allows us to estimate the lifetime of the detector and predict the longterm change of the signal. This change can then be accounted for when interpreting the output data.

3.1 Measurement setup

To get reliable measurement results, great care has to go towards designing a measurement setup that minimises the noise in the measurements. Shielding has to be applied wherever possible. For instance, aluminium foil can be wrapped around the exposed parts of the system to shield them from external radio-frequency (RF) interferences. In addition, the sensors have to be covered to prevent the light from shining directly onto them. The incident photons can deposit enough energy to increase the leakage current of the detector.

The measurements using diamond that are explained in these chapters were carried out using several measurement setups, but they are all similar in terms of the electrical signal chain. The measurement chain consists of three main parts: a diamond sensor, a signal preamplifier and a readout device, as seen in diagram 3.1. The signals propagating along the analogue chain (before being digitised by the readout device) are fast – in the GHz bandwidth range – and with low amplitudes – of the order of tens of μV . This gives rise to importance of RF shielding. Also, the connection between the carrier and the preamplifier has to be as short as possible to avoid capacitive signal losses in the transmission line. Finally, the system needs to be grounded properly.

3.1.1 Preamplifiers

Two preamplifiers are used for the measurements, one sensitive to charge and the other to current. *CIVIDEC Cx* (figure 3.2a) is a charge sensing amplifier. Its high SNR (equivalent noise charge of $300 + 30\text{ pF}^{-1}\text{ e}^-$ and a reported gain of $\sim 12\text{ mV/fC}$) makes it a good choice for spectroscopic measurements with diamond

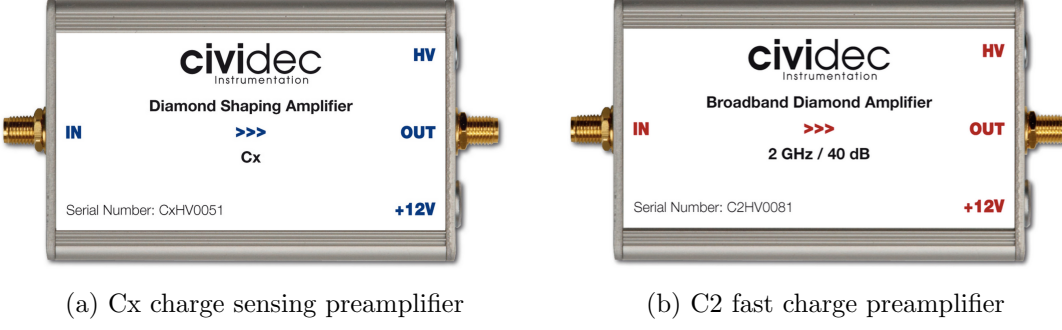


Figure 3.2: Amplifiers used for the charge and current measurements

968 sensors. *CIVIDEC C2* (figure 3.2b) is a fast current preamplifier with a 2 GHz band-
969 width limit. It is used for TCT measurements because of its fast response and a good
970 SNR. Both are embedded in an RF-tight aluminium box to reduce the noise pickup.
971 Both have an AC coupled input and an output with a 50Ω termination.

972 3.1.1.1 Calibration

973 The amplifiers have to be calibrated before use to determine their gain. Both are
974 calibrated using a square signal generator with a known amplitude step of $U_{\text{in}} =$
975 (252 ± 5) mV. A 2 GHz oscilloscope with a 10 GS/s sampling is used to carry out
976 these measurements.

977 In the case of the Cx charge sensitive amplifier, the signal is routed through a
978 capacitor with a calibration capacitance $C_{\text{cal}} = (0.717 \pm 0.014)$ pF and then to the
979 input of the amplifier. The pulse area behind the capacitor is $a_{\text{cal}} = (5.0 \pm 0.5)$ pVs,
980 with the signal amplitude on the output amounting to $U_{\text{Cx}} = (1.95 \pm 0.05)$ V. The
981 input voltage step combined with the calibration capacitance yields a calibration
982 charge $Q_{\text{cal}} = C_{\text{cal}} \cdot U_{\text{in}} = (181 \pm 5)$ fC. The gain of the Cx amplifier is therefore
983 $A_{\text{Cx}}^Q = \frac{U_{\text{Cx}}}{Q_{\text{cal}}} = (9.3 \pm 0.4)$ mV/fC or $A_{\text{Cx}}^a = \frac{U_{\text{Cx}}}{a_{\text{cal}}} = (390 \pm 40)$ mV/pVs. The area-based
984 amplification factor has a higher uncertainty ($\sim 10\%$) than the amplitude-based
985 factor ($\sim 4\%$) due to the measurement limitations of the oscilloscope. Nevertheless,
986 it can be used as an estimate for the integrated charge of a current pulse.

987 To calibrate the C2 current amplifier, only the amplitude gain has to be measured.
988 The input signal amplitude has to be such that it keeps the output amplitude within
989 the amplifier's linear range, that is ± 1 V. The signal from the generator is therefore
990 routed through a 36 dB attenuator to decrease its amplitude to $U_{\text{inAtt}} = (3.95 \pm$
991 $0.05)$ mV. Two amplifiers with different gains have been measured, because both
992 are used for the measurements at different times. The output of the first amplifier
993 amounts to $U_{\text{C2-1}} = (860 \pm 5)$ mV. This yields the amplification gain equal to $A_{\text{C2-1}} =$
994 $\frac{U_{\text{inAtt}}}{U_{\text{C2-1}}} = (217 \pm 3)$. The second amplifier has the output equal to $U_{\text{C2-2}} = (632 \pm 5)$ mV
995 with the gain equal to $A_{\text{C2-2}} = (152 \pm 3)$.

3.1. MEASUREMENT SETUP

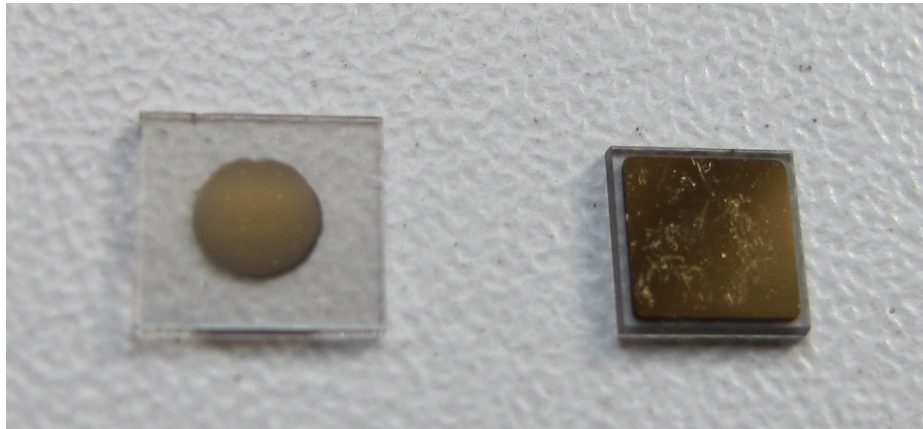


Figure 3.3: Two scCVD diamond samples: A IIa 1scdhq (left) and an E6 S37 (right)

3.1.2 Diamond samples

Detector-grade diamonds are very difficult to produce, mostly because it is very difficult to ensure a high enough purity of the lattice. The sensor samples used for these studies were bought at Element Six (E6) [5]. They all have the same standard dimensions. sCVD diamonds with dimensions $4.7 \times 4.7 \text{ mm}^2$ are already sufficiently large for most of the beam monitoring applications and still affordable. One of the samples with dimensions of $5.6 \times 5.3 \text{ mm}^2$ produced by IIa Singapore [7] was also sent to CERN to be characterised. The target thickness for all the samples is $500 \mu\text{m}$. Diamonds this thick yield a high enough signal-to-noise ratio for MIPs to be measured by the electronics. Table 3.1 shows all the samples used for this study. Two of them were later irradiated with 300 MeV pions and then compared to the pre-irradiated state. Irradiation doses for damaging the material need to be high – above 10^{12} particles per cm^2 to be able to observe change in the sensor's behaviour.

1009	Name	Type	Producer	Dimensions [mm^2]	Thickness [μm]	Electrode	Irradiated
	S37	sCVD	E6	4.7×4.7	548	Cr/Au	no
	S50	sCVD	E6	4.7×4.7	537	Cr/Au	no
1010	S52	sCVD	E6	4.7×4.7	515	Cr/Au	$1 \times 10^{14} \pi \text{ cm}^{-2}$
	S79	sCVD	E6	4.7×4.7	529	Cr/Au	$3.63 \times 10^{14} \pi \text{ cm}^{-2}$
	ELSC	sCVD	E6	4.7×4.7	491	Cr/Au	no
	1scdhq	sCVD	IIa	5.6×5.3	460	Cr/Au	no

1011 Table 3.1: Diamond sensor samples used

The diamond samples have quoted impurity densities of $\leq 2 \times 10^{14} \text{ cm}^{-3}$ and nitrogen incorporation of $\leq 1 \text{ ppb}$. The electrodes were added by various companies and institutes. For instance, S52 was metallised by a company DDL (now defunct) while the Physics Department of the University of Firenze, Italy metallised the S79. There are also several techniques for producing the electrodes. The DDL contacts consist of three layers: DLC (diamond-like carbon)/Pt/Au with 4/10/200 nm thicknesses, respectively. The metallisation for S79, on the other hand is made up of Cr/Au with

a total thickness of ~ 400 nm. The area coverage also differs from sample to sample. Diamonds must not be metallised until the very edge as the proximity of contacts with a high potential can lead to sparking. However, the areas not covered by the metallisation are less efficient because the fringe fields at the edges are not as strong as in the middle. This effectively reduces the sensitive area of the sensors. In the diamonds used here the effective area was anywhere from 9 mm^2 to 18 mm^2 . Leakage current through the bulk was below 1 ns, but increased for the irradiated samples. The capacitance was of the order of (2.0 ± 0.3) pF.

3.1.3 Readout devices

Electrical signals in diamond detectors are in the GHz frequency range. To preserve this information, the readout device has to have a high bandwidth limit. For instance, a 250 MHz limit is enough for the spectroscopic measurements with the Cx charge amplifier, but might be insufficient for the current measurements with the C2 amplifier. Two devices are used take data shown in this chapter. The first choice is a 2 GHz LeCroy WaveRunner 204MXi-A. This specific model has a high enough limit for the fast current preamplifier signals. It offers a versatile solution for analogue signal readout – it is fast to set up and reliable. It is very convenient for use in lab tests and for experiments where small amounts of data are taken and where speed is not crucial. However, its slow acquisition speed turns out to be a bottleneck in the test beam experiment. Its initial 100 Hz readout rate decreases to a mere 20 Hz within 20 minutes, because every single trigger is saved as a separate file and the Windows operating system is not capable of handling 10000+ files in a single directory easily. This is why it has been exchanged with a DRS4 [4], an analogue readout device developed by PSI, Switzerland. This compact device is capable of recording up to four waveforms at a time at a steady rate of up to 500 Hz. Its 700 MHz bandwidth limitation is sufficient for the signal from the charge amplifier.

3.1.4 Setup for the efficiency study using β particles

The efficiency study of the diamond sensors has been carried out at CERN in the North Hall test beam facility. There a straight high-energy particle beam of $\pi_{120}\text{ GeV}$ is provided to the users to calibrate their detectors. The beam had a transverse spread of $\sigma = 10$ mm in both axes. The particle rate is of the order of $10^4 \pi \text{ cm}^{-2} \text{ s}^{-1}$. A diamond sensor embedded in a PCB carrier has been placed in the beam spot perpendicular to the beam and connected via an SMA connector directly to a charge amplifier (described below). The amplified signal is read out using a LeCroy oscilloscope and a DRS4 analogue readout system (both described below). A computer is used as a controller and data storage for the readout device. A beam telescope is used as a reference detector. It is a device that helps to cross-check the measurements of the devices under test (DUTs) and to carry out spatially resolved studies on the DUTs. It consists of several pixellated sensor planes placed in series, which can track a particle's trajectory with a precision of a few μm . The sensor planes are positioned

3.1. MEASUREMENT SETUP

in front of the DUT and behind it. Then the beam telescope acts as a trigger system – it triggers the readout of both the telescope data and DUT data when both the planes in front and behind the DUT recorded a hit by the incident particle. A particle detected by all the planes within the DUT window and the DUT itself counts towards its efficiency whereas a hit missed by the DUT means that the DUT is not 100 % efficient. To discard the hits that miss the DUT completely, a region of interest (ROI) can be chosen in the beam telescope planes. The equation for calculating the sensor efficiency is therefore

$$\epsilon = \frac{N_{\text{DUT}} \wedge N_{\text{telescope}}}{N_{\text{telescope}}} \quad (3.1)$$

for an ROI smaller than the sensitive region of the diamond.

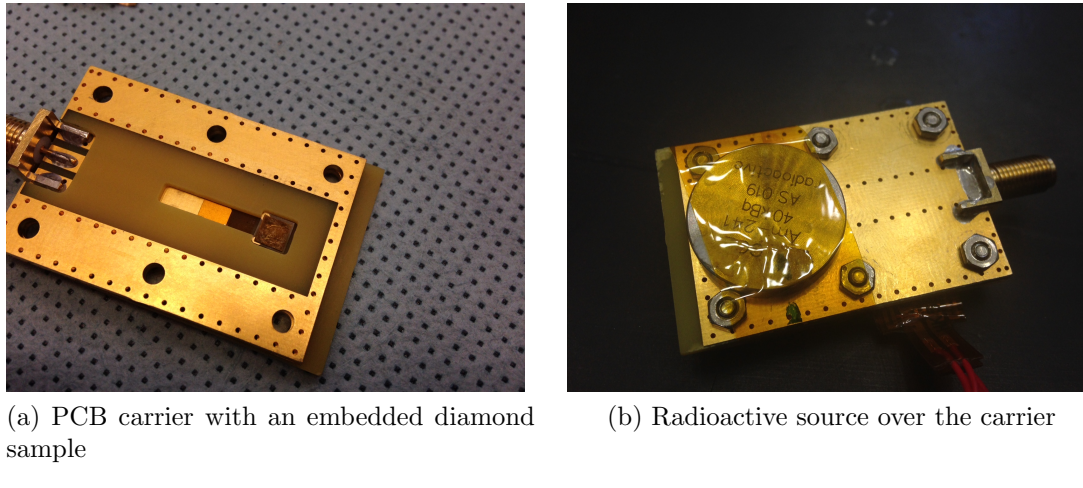
3.1.5 Room temperature α -TCT setup

This TCT study is a follow-up of an extensive diamond TCT study at cryogenic temperatures [28]. The room-temperature TCT measurements have been carried out in the lab. The setup consists of a diamond sensor embedded in a PCB carrier, a current amplifier and an oscilloscope. To measure α particles, their energy loss during their trajectory has to be minimised. Therefore the diamond is placed inside a vacuum chamber. The chamber is a steel tube with a diameter of 5 cm. On one side it is connected to a vacuum pump via a steel pipe. A feedthrough with an SMA connector is placed on the other side. A C2 current amplifier is connected directly onto the feedthrough. The amplified output is connected to the oscilloscope via an SMA cable. An ^{241}Am source with a diameter of 2 cm and a height of 0.5 cm is fixed onto the sensor carrier (figure 3.4a, figure 3.4b). Then the carrier is inserted in the chamber and fixed in place using an air-tight clamp. The pump can then be switched on. It is capable of providing the inside pressure as low as 10^{-4} mbar after approximately one hour of operation, but measurements can take place even after five minutes of evacuation, at around 10^{-3} mbar. The most important thing to bear in mind is to switch the bias voltage of the sensor OFF during the process of evacuation, because the gas becomes more conductive at the pressure of the order of 10^{-1} mbar, which is at the bottom of Paschen's curve [21]. A failure to switch off the bias voltage may cause a spark between the signal and ground line, destroying the amplifier.

3.1.6 Cryogenic α -TCT setup

The experiment at cryogenic temperatures has been carried out in the cryolab at CERN. The room-temperature TCT setup has to be modified to allow for measurements at temperatures as low as 2 K. It consists of three parts:

1. a cryostat – a thermally insulated cylinder capable of containing liquid helium,
2. an inlet – an air-tight mechanical tube with valves and feedthroughs at the top that is lowered in the liquid helium and



(a) PCB carrier with an embedded diamond sample
(b) Radioactive source over the carrier sample

Figure 3.4: Positioning of the α -source on top of the sensor carrier

1095 3. the diamond sample embedded in a PCB carrier with a fitted temperature
1096 sensor, a heater and cables leading to the feedthroughs.

1097 The setup is described in detail in [28].

1098 When the diamond sample is placed in the PCB carrier and the ^{241}Am source is in
1099 place, the inlet is sealed and lowered in the empty cryostat. Then the inside volume
1100 of the inlet is evacuated to down to 10^{-5} mbar while the liquid helium is flowing into
1101 the cryostat. To improve the thermal contact between the diamond and the coolant,
1102 a small amount of helium gas is added inside the evacuated inlet, setting the vacuum
1103 to around 10^{-3} mbar. This value changes with time, because the gas condenses on
1104 the walls of the inlet, reducing the number of floating particles. For this reason the
1105 helium gas has to be added on an irregular basis. Every addition causes a significant
1106 undershoot of the sample temperature, which had to be corrected for using a heater
1107 placed on the back of the PCB carrier. Also, the added gas deteriorates the vacuum
1108 inside the inlet. It is very important to monitor the pressure so as not to let it rise
1109 above 10^{-2} mbar. The gas at this pressure is significantly more conductive and could
1110 cause a short circuit between the two diamond plates or in the SMA connectors,
1111 destroying the amplifier. Furthermore, at approximately 60 K the helium gas has to
1112 be evacuated from the inlet to avoid a potential explosion due to the expansion of
1113 the gas with temperature.

1114 When the sample is cooled to the minimum temperature achievable by means
1115 of liquid helium without over-pressurising it (4.2 K), the measurements start. A
1116 temperature sensor placed on the back of the PCB carrier is used to measure the
1117 temperature of the sample. After every temperature data point, the current through
1118 the heater placed in the PCB next to the diamond sample is increased, warming up
1119 the sample. The initial temperature time constant of the order of tenths of seconds at
1120 low temperatures increases with temperature. Even more so when helium is evacuated
1121 from the inlet at 60 K, removing the thermal bridge between the wall of the inlet and
1122 the diamond sample. At the room temperature (RT), the time constant increases to

3.2. CHARGED PARTICLE PULSES AND SPECTRA

1123 the order of minutes.

1124 3.2 Charged particle pulses and spectra

1125 In previous chapter the ionisation profiles for different types of radiation were dis-
1126 cussed. It is known that β and γ radiation induces a triangular electric pulse whereas
1127 α radiation induces a rectangular one. However, their amplitude, width and rise/fall
1128 time depend heavily on the type of interaction with the diamond, the purity of the
1129 diamond and the bandwidth of the amplifier and the oscilloscope. This section shows
1130 the signal pulses of α , β and γ radiation with their respective energy distributions for
1131 the case of a diamond detector. Then follows a discussion of effects of noise on these
1132 measurements.

1133 A CIVIDEC C2 current amplifier together with the LeCroy oscilloscope (both
1134 with a bandwidth limit of 2 GHz) has been used to record the pulse shapes whereas
1135 the Cx charge amplifier is used for charge measurement. A 2 GHz bandwidth limit
1136 defines the minimum rising time equal to $t_r \simeq \frac{0.34}{BW} = \frac{0.34}{2 \times 10^9} = 170$ ps, therefore
1137 the system is capable of measuring pulses with a minimum FWHM $\simeq 170$ ps. This
1138 already makes it impossible to measure the initial peak in the α response due to the
1139 two flavours of charge carriers travelling. If a charge carrier travelling through the
1140 bulk takes $t_{t1} \sim 6$ ns to get to the electrode on the other side ($d_1 \sim 500$ μm), the
1141 carrier with the opposite charge and a shorter path to the closer electrode – max.
1142 $d_2 \sim 10$ μm – only takes $t_{t2} \sim \frac{d_2}{d_1} t_{t1} = 120$ ps. A drift time this short induces a
1143 current pulse that is too narrow for the C2 amplifier or the oscilloscope to be able to
1144 observe.

1145 Figure 3.5 shows a set of pulses and an averaged pulse for α , β and γ radiation
1146 using an ^{241}Am , ^{90}Sr and ^{60}Co source, respectively. The particles are measured with
1147 the non-irradiated sCVD diamond S37. α particles always produce the same signal
1148 pulse, but with a high noise RMS. The averaging suppresses the noise while still
1149 retaining most the information. It does, however, smear the rising and falling edge,
1150 increasing the rise time. The t_r is now of the order of 0.5 ns. Both β and γ pulses
1151 look similar – triangular and with a wide range of amplitudes. Here the pulse count
1152 is low, so the pulses with a high amplitude are not recorded. A trigger set very high
1153 would be needed to “catch” them with the oscilloscope.

1154 3.2.1 Noise limitations

1155 Noise is a major limiting factor in particle detection. It defines the minimum measurable
1156 particle energy and the minimum measurement resolution. It is hence important
1157 to minimise the electric noise in the detector signal. The major noise contribution
1158 comes from poor shielding from external electromagnetic sources. These often cause
1159 ringing, whereby the signal oscillates with a frequency defined by the external source.
1160 The ringing makes high-frequency measurements impossible. Another source of noise
1161 is the sensor itself. In the case of silicon, natural light increases the number of ther-

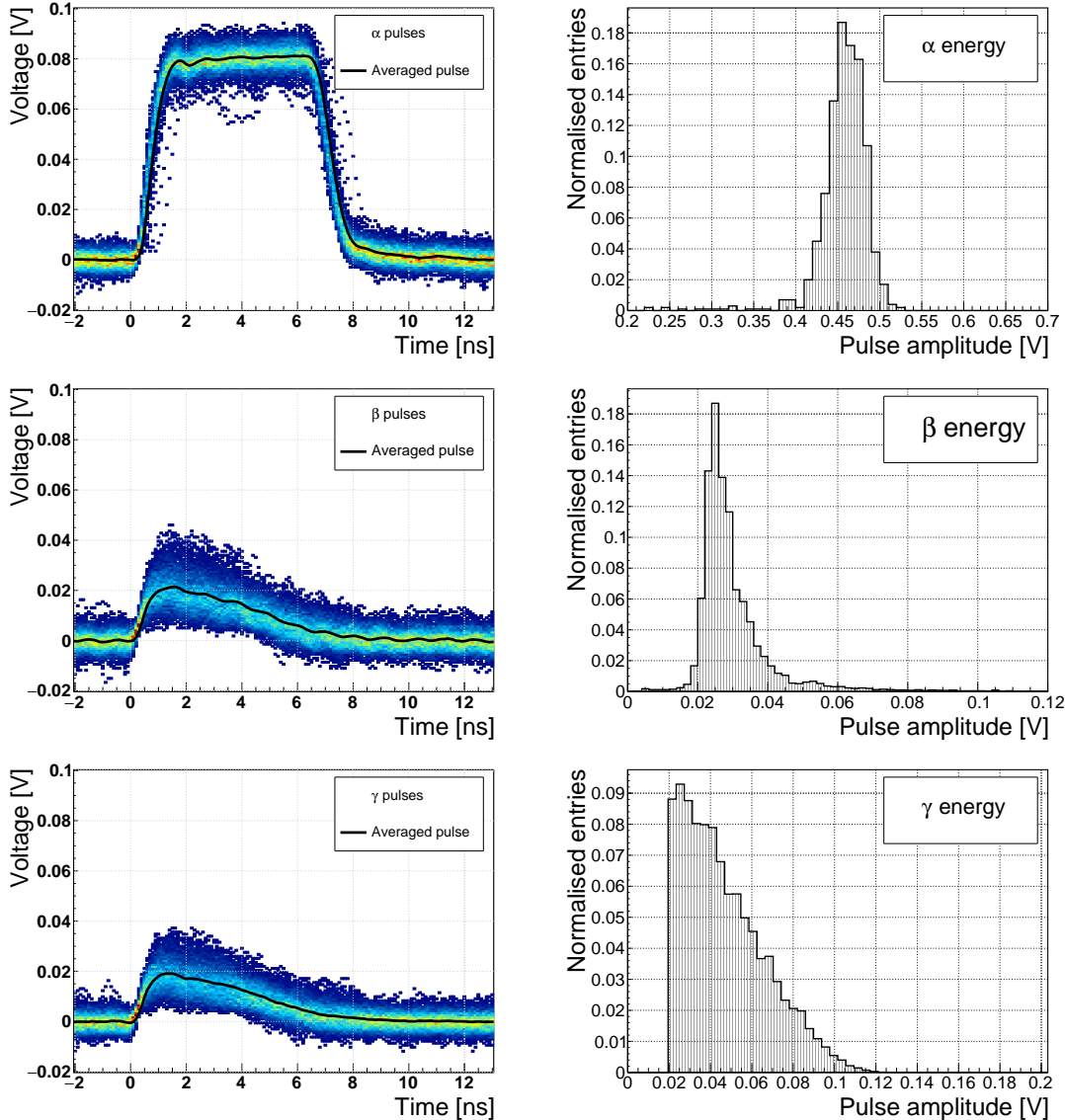


Figure 3.5: Superimposed and averaged pulses (a, b and c, current amplifier) and distributions of deposited energy (d, e, f, charge amplifier) for three types of radiation. Note the scale on the X axis of the distributions.

1162 mally excited free charge carriers, increasing the leakage current. This is not the
 1163 case for diamond, which is with its high energy band gap insensitive to visible light.
 1164 Nevertheless, any noise produced by the sensors is amplified by the signal amplifiers,
 1165 which add an additional noise of the analogue electrical circuit to the amplified
 1166 signal. Finally, the digitisers add the quantisation noise to the digitised signal. If
 1167 the measurement range is significantly higher than the actual measured signal, the
 1168 quantisation noise can be a significant contributor to the decrease of the overall mea-
 1169 surement resolution.

3.3. RADIATION LIMITATIONS

3.3 Radiation limitations

Exposure to ionising radiation degrades sensors. It deforms the lattice by displacing the atoms. Various types of lattice defects can be created in diamond, similar to those in silicon: vacancies, interstitials etc. [31] These deformations introduce new discrete energy levels between the valence and conduction band. Charge carriers drifting in their vicinity can get trapped, their energy falling to the energy level of the trap. Their emission back to the conduction band depends on how deep the trap is (how far away from the conduction band it is). The carriers caught in the shallow traps of the order of 100 meV below the conduction band are excited back up already by means of the thermal excitation. This phenomenon has a short time constant, dependant on the environmental temperature. Those stopped by deep traps near the middle of the band gap need more energy and thus more time to be emitted to either the conduction or valence band. Some charge carriers remain trapped for long periods. If they build up in a certain region of the diamond, their charge starts affecting the surrounding electric field – space-charge forms. It can either help or counteract the field, depending on the polarity of the carrier.

The energy band jumping goes the other way, too. The carriers in the valence band may use the intermediate energy levels as “stepping stones” to jump to the conduction band and start drifting in the externally applied electric field. This is called the leakage current.

The electrons and holes stopped in these traps cause a decrease of the induced current on the electrodes. This yields a lower integrated charge in an irradiated sensor than that in a non-irradiated one. Charge collection efficiency is therefore correlated with the level of irradiation.

This section contains a study of the effects of pion ($\pi_{300 \text{ MeV}}$) irradiation on the charge collection efficiency of sCVD diamond detectors. To carry out this study, two diamond samples have been irradiated to doses of $1 \times 10^{14} \pi \text{ cm}^{-2}$ (S79) and to $3.63 \times 10^{14} \pi \text{ cm}^{-2}$ (S52). Then a test beam campaign has to be carried out to observe the charge collection efficiency at different bias voltage settings. The efficiency values acquired are used to determine the effective drop in efficiency with respect to received radiation dose. This is to test if the collected charge Q is inversely proportional to the received dose Φ . A procedure defined by a collaboration researching diamond behaviour RD42 has been applied to the measured values to extract the damage factor. The next subsection contains measurements and results of a long-term stability study using α and β particles. In particular, the charge collection efficiency as a function of time is measured during the measurements with β and α radiation. To investigate this effect on the scale of charge carriers, the change of TCT pulses with time is observed. Finally, a procedure that improves the pulse shape and with it the charge collection is proposed.

3.3.1 Quantifying radiation damage in diamonds

Radiation damage varies with the type of radiation (particles or photons) and its energy. There are several models existing [27, 26] that try to explain the impact of irradiation and to provide *hardness factors* to compare the radiation damage between different particles. The standard way is to convert the damage into *neutron equivalent* [14]. Some models have been extensively verified with simulations and with experiments. In these experiments charge collection in sensors is measured before and after irradiation. This procedure is repeated several times, with a measurement point taken after every irradiation. When a set of measurements of charge collection is plotted against the radiation dose received by a specific particle at a specific energy, a damage factor k_λ can be extracted. Damage factors have to be measured across a range of energies and types of radiation to properly quantify the damage in the sensors. They are then compared against the simulations to verify that the experimental observations are in line with the theory.

Diamond is an expensive material and the technology is relatively new as compared to silicon. Therefore not many institutes are carrying out diamond irradiation studies. To join the efforts, the RD42 collaboration [11] was formed. It gathers the experimental data from diamond irradiation studies. Unlike with silicon, the experimental results so far show no significant correlation with the NIEL (non-ionising energy loss) model [27], which correlates detector efficiency with the number of lattice displacements. Therefore an alternative model was proposed [26], correlating the diamond efficiency with the number of displacements per atom (DPA) in the bulk. The idea is that if the recoil energy of an incident particle is higher than the lattice binding energy (42 eV for diamond), the atom is displaced from its original position. The newly formed vacancy acts as a trap for drifting charge carriers. The more displacements that form in the bulk, the higher is the probability that a drifting carrier will get trapped, effectively reducing the induced signal. However, different types of particles interact differently with the bulk. In addition the mechanisms of interaction at low energies are different to those at high energies. To assess the damage for individual particles at a range of energies, simulations need to be run first. The simulation shown in [26] shows the DPA model for a range of energies of proton, pion and neutron irradiation in diamond. Figure 3.6 contains the simulation results as well as the superimposed empirical results of several irradiation studies. According to the figure, a 300 MeV pion beam damages the diamond bulk twice as much as a 24 GeV proton beam. The data points obtained by RD42 are also added to the figure. They have been normalised to damage by 24 GeV protons. Finally, the data point measured in the scope of this thesis has been added for comparison. The derivation is done below.

3.3.1.1 Irradiation with a $\pi_{300 \text{ MeV}}$ beam

The samples were irradiated at the Paul Scherrer Institute (PSI) [10] by means of a beam of pions with an energy of 300 MeV (kinetic energy 191.31 MeV) and with a

3.3. RADIATION LIMITATIONS

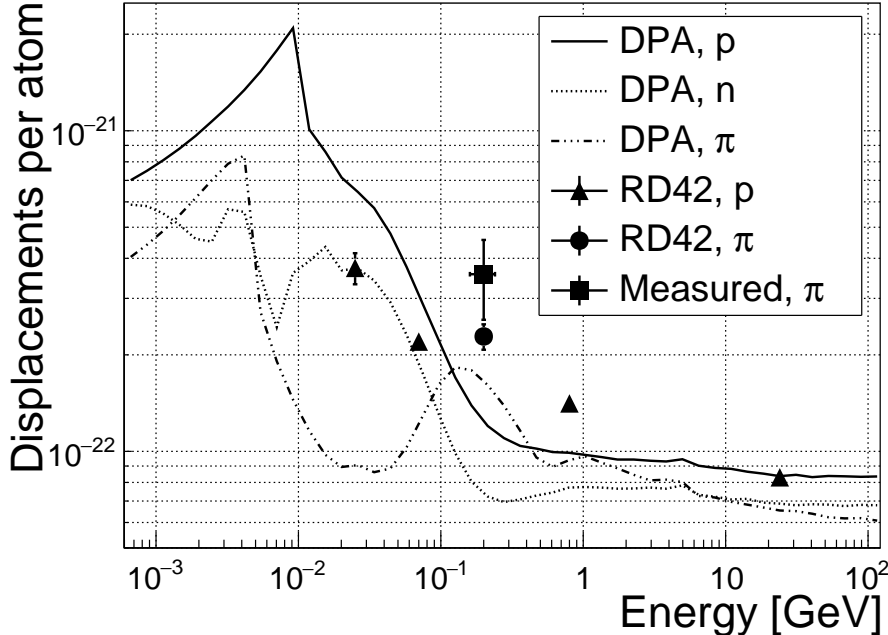


Figure 3.6: Diamond radiation damage - a model based on displacements per atom [26]. Added are data points for protons and pions by RD42 [35] and one data point for pions measured in the scope of this thesis.

flux of up to $1.5 \times 10^{14} \pi \text{ cm}^{-2}$ per day. The system has a 10 % uncertainty on the beam energy. In addition, their quoted uncertainty on the measurement has an error of ± 20 %. Looking at the pion damage curve in figure 3.6, $\pi_{300 \text{ MeV}}$ point sits on a steep section of the DPA curve. This means that a deviation in beam energy can have a significant effect on the damage.

Two diamond samples, S52 and S79, were put in the $\pi_{300 \text{ MeV}}$ beam in the 2014 PSI irradiation campaign; S52 to $(1 \pm 0.21) \times 10^{14} \pi \text{ cm}^{-2}$ and S79 to $(3.63 \pm 0.77) \times 10^{14} \pi \text{ cm}^{-2}$. During the process, the golden electrodes got slightly activated, but the activation decayed in two weeks.

3.3.1.2 Charge collection efficiency and charge collection distance

Three diamonds – non-irradiated S37 and irradiated S52 and S79 – were tested in a $\pi_{120 \text{ GeV}}$ test beam in the SPS North Experimental Area at CERN [18] before and after irradiation. The goal was to estimate the charge collection efficiency (CCE) and charge collection distance (CCD) as a function of irradiation dose. The samples were primed (pumped) prior to data taking using a ^{90}Sr radioactive source. The data were then taken at a range of bias voltages ranging from 30 V to 900 V, yielding between 0.06 V/ μm and 1.8 V/ μm electrical field in the bulk. Every data point contained approximately 5×10^4 measured particles. The charge deposited by the particles was measured using a CIVIDEC Cx charge preamplifier. As expected, the integrated

1269 amplitude spectrum followed a landau distribution. Its most probable value (MPV)
1270 was used to calculate the most probable collected charge Q_i :

$$Q_i [e^-] = \frac{Q_i [fC]}{1.6 \times 10^{-4}} = \frac{MPV [mV]}{A [mV/fC]} \cdot 6.241 \times 10^4 \quad (3.2)$$

1271 where $A = 9.2 \text{ mV/fC}$ is the preamplifier gain factor. The CCD was then calculated
1272 using the average number of electron-hole pairs produced per micrometer in diamond
1273 $\delta_d = 36 \text{ e-h } \mu\text{m}^{-1}$ (from table 5.2):

$$CCD = \frac{Q_i}{\delta d} \quad (3.3)$$

1274 The resulting CCD for the three measured samples at bias voltages ranging from
1275 $0.2\text{--}1.6 \text{ V } \mu\text{m}^{-1}$ is shown in figure 3.7a. S37 exhibits a full collection distance already
1276 at $0.4 \text{ V } \mu\text{m}^{-1}$ whereas the irradiated samples have a more gentle increase of CCD
1277 with increasing bias voltage. It is evident that at $1 \text{ V } \mu\text{m}^{-1}$ the maximum CCD has
1278 not been reached in the case of S79 and S52. Nevertheless, to compare the measured
1279 data point with those provided by RD42, the CCD at $1 \mu\text{m}$ has to be taken.

1280 3.3.1.3 Irradiation damage factor

1281 The irradiation damage factor k is a way to quantify irradiation damage of a specific
1282 particle at a specific energy. Via this factor different types of irradiation can be
1283 compared. It is obtained experimentally by measuring the CCD of a number of
1284 samples at various irradiation steps and fitting the equation 3.5 to the data. λ is the
1285 measured CCD, λ_0 is the CCD of a non-irradiated sample and Φ the radiation dose.
1286 As a reference, the damage factor for 24 GeV protons is set to $1 \times 10^{-18} \mu\text{m}^{-1} \text{ cm}^{-2}$.

$$\frac{1}{\lambda} = \frac{1}{\lambda_0} + k_\lambda \cdot \Phi \quad (3.4)$$

$$\lambda = \frac{\lambda_0}{k_\lambda \lambda_0 \Phi + 1} \quad (3.5)$$

1287 The data points with the maximum CCD obtained in the test beam measurements
1288 are plotted against radiation dose received (see figure 3.7b). Equation 3.5 is fitted
1289 to the data points and a damage factor $k_\lambda = (4.4 \pm 1.2) \times 10^{-18} \mu\text{m}^{-1} \text{ cm}^{-2}$ was
1290 obtained. This value is for a factor of two higher than the damage factor obtained by
1291 RD42. This could be due to an insufficient priming time ahead of the measurement.
1292 In addition, the diamond samples have not been polished and re-metallised after
1293 irradiation, as is the case for the RD42. Also, with only two samples measured, the
1294 statistical uncertainty is high. Nevertheless, it can be concluded that the 300 MeV
1295 pions damage the diamond bulk more than the 24 GeV protons.

3.3. RADIATION LIMITATIONS

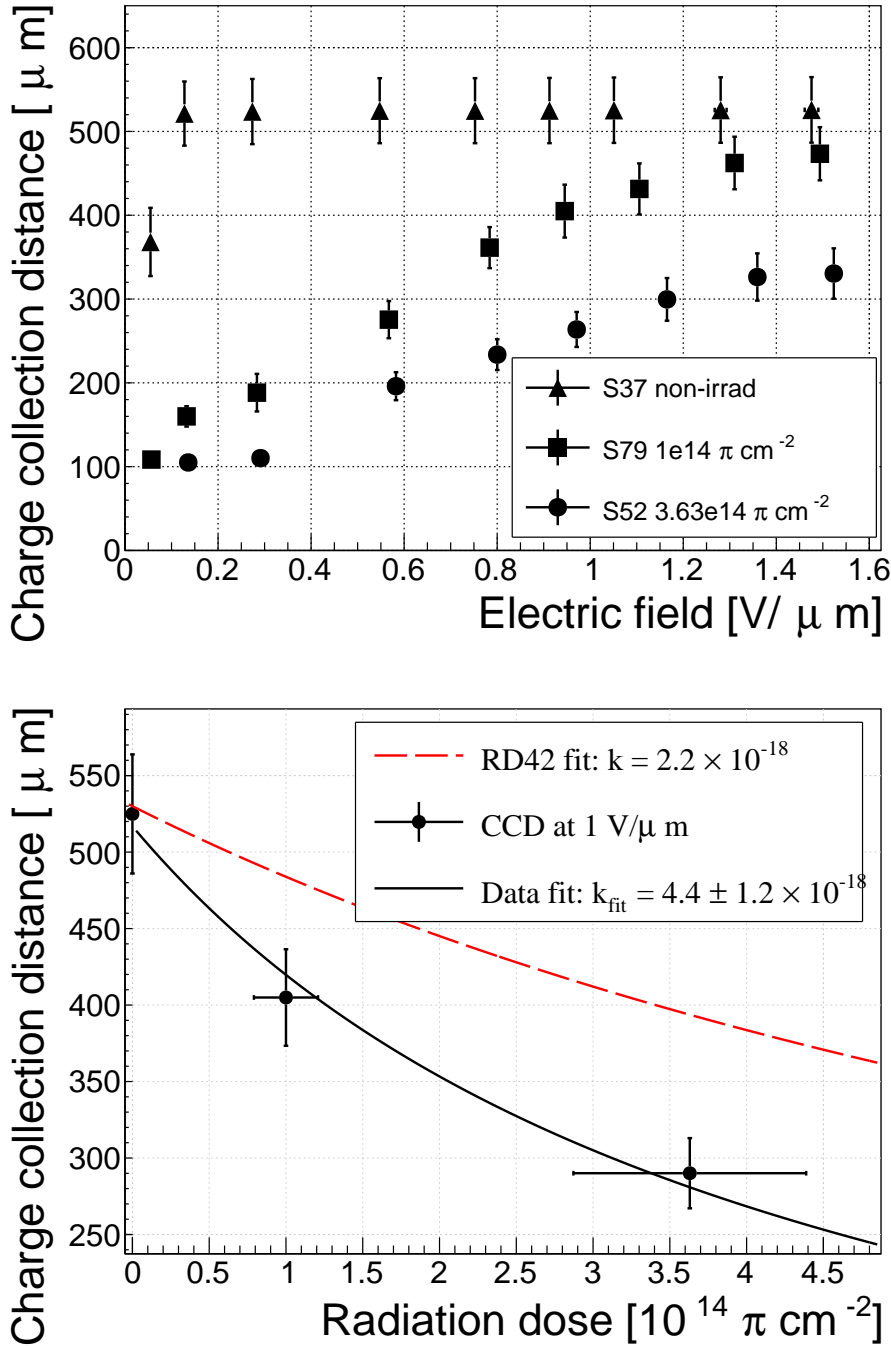


Figure 3.7: First figure shows the CCD for S37, S79 and S52 at a range of bias voltage settings. The charge collection distance at 1 V/μm bias voltage for the three diamond samples is then compared to the RD42 data for pion irradiation in the second figure. The data points are about 15–25 % lower than expected from the RD42 data [35].

¹²⁹⁷ **3.3.2 Long-term measurement stability**

¹²⁹⁸ An important requirement for particle detectors is a stable performance over long
¹²⁹⁹ periods of time. For instance, the charge collection for a defined radiation type and

1300 quantity must not change over time or has to change in a predicted way. Diamonds
1301 are stable as long as their environment and their operating point does not change
1302 significantly. The stability of diamond detectors depends on many factors (material
1303 purity, polishing process, electrode material, irradiation damage etc.). The aim is
1304 to study the behaviour of diamond under controlled conditions, with the goal to
1305 understand its limitations. One of these limitations is for sure the received radiation
1306 dose as it can affect the long-term stability of the sensor during operation.

1307 The three diamond samples (S37, S79 and S52) have been exposed to two different
1308 types of ionising radiation for a longer period to see if their behaviour changes over
1309 time. Two parameters have been observed in particular:

- 1310 1. Charge collection of β particles and
- 1311 2. Charge collection and ionisation profile of α particles.

1312 The results in this and in the next section will show that, in both cases, priming plays
1313 an important role in improving the diamond measurement stability.

1314 3.3.2.1 β long-term stability

1315 The diamond samples have undergone a long-term stability test using β radiation.
1316 This has been done using a ^{90}Sr source emitting ~ 2 MeV electrons at a rate of
1317 approximately $10^4 \text{ e}^- \text{ cm}^{-2}$. To simulate the initial conditions in HEP experiments,
1318 the sensors must not be primed before starting the measurements. The measurement
1319 setup consists of a diamond sample (S37, S52 or S79) with the Cx spectroscopic
1320 amplifier, a silicon diode with a C6 amplifier for a trigger and a ^{90}Sr source on
1321 top. A particle emitted by the source traverses the sensor bulk and hits the silicon
1322 diode, triggering the analogue signal readout. The source is left on the top for the
1323 course of the experiment. The measurements, however, are taken at discrete times.
1324 For every data point, approximately 10^4 triggers are recorded. The offline analysis
1325 of the recorded signal pulse amplitudes yields a landau distribution for every data
1326 point. The most probable value (MPV) of the distribution is proportional to the
1327 collected charge by the diamond sensor. The resulting graph of charge collection over
1328 time (see figure 3.8) shows that the charge collection efficiency improves when the
1329 diamond sensor is primed with a β source. This is especially evident in the case of
1330 the two irradiated samples. S79 achieves close to a full efficiency whereas S52 reaches
1331 about 50 %. Both increases are significant. At a received dose of approximately
1332 4×10^6 particles the signal stabilises. As expected, the signal of the non-irradiated
1333 S37 does not change with time – this pure sCVD diamond sample has the maximum
1334 collection distance from the start of the measurement.

1335 It should be noted that the ~ 2.28 MeV electrons emitted by this source are not
1336 MIPs; their charge deposition is higher than that of an electron MIP, according to the
1337 Bethe-Bloch distribution [16]. Nevertheless, for the purpose of these measurements
1338 this energy was adequate since only the relative change in charge collection was of
1339 our interest.

3.3. RADIATION LIMITATIONS

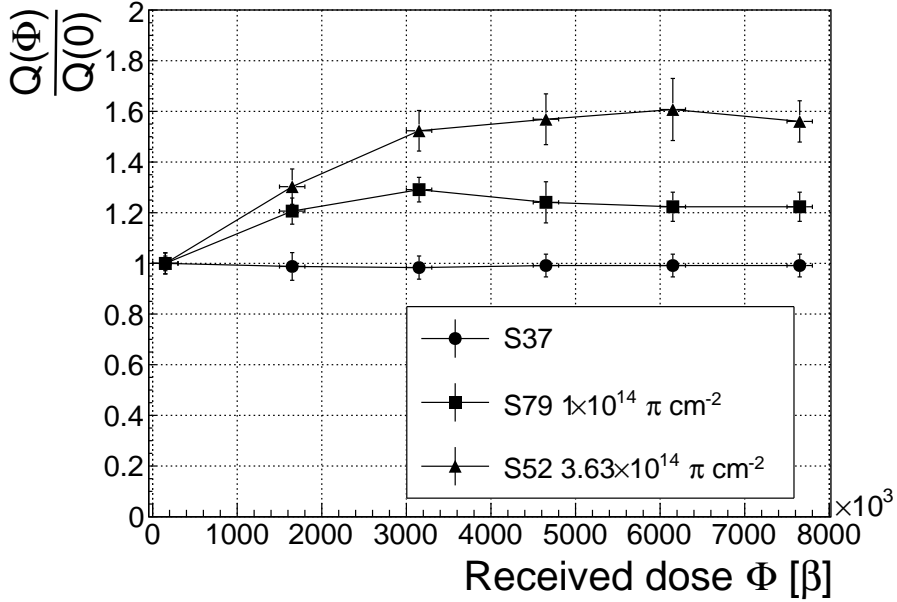


Figure 3.8: Relative increase of charge collection over time due to priming with the ${}^{90}\text{Sr}$ radioactive source. The bias voltage for this measurement is 1 V/ μm .

To sum up, diamond is a good choice for β radiation detection. Even if damaged by radiation, it reaches a stable charge collection at a received dose of $\sim 4 \times 10^6$ MIP particles. The efficiency decreases with a high irradiation dose (effects visible above 10^{12} MIP cm^{-2}). However, the decrease can be accounted for if the damage factor and the rate and energy of the particles are known. γ radiation has a similar impact on the diamond as the β because the ionisation mechanism is the same. The incident photons, if they interact with the diamond, prime the bulk, causing the increase in charge collection efficiency. The difference, however, is that the interaction probability (cross section) is lower for gammas [41, 25].

3.3.2.2 α long-term stability

This part discusses the stability of irradiated diamond sensors during α measurements. An ${}^{241}\text{Am}$ source is used, emitting α particles with a mean energy of 5.5 MeV. It is safe to assume that they will behave differently than when subject to β radiation. This is due to the point-like charge carrier creation when an α particle penetrates the bulk and stops at a depth of $\sim 14 \mu\text{m}$ (for a 5.5 MeV particle). The deposited energy produces $\frac{5.5 \text{ MeV}}{13.6 \text{ eV}} = 4 \times 10^5$ e-h pairs. Compared to a MIP, which produces an MPV of $500 \mu\text{m} \times 36 \text{ e-h } \mu\text{m}^{-1} = 18 \times 10^3$ e-h pairs in a $500 \mu\text{m}$, the collected charge is for a factor of 22 higher. In addition, the energy is deposited in a small volume – $14 \mu\text{m}$ in depth and $\sim 20 \text{ nm}$ radially [28]. This dense distribution of charge carriers affects their behaviour at the start of the drift. Furthermore, carriers of only one polarity drift through the sensor while those of the opposite polarity almost instantly

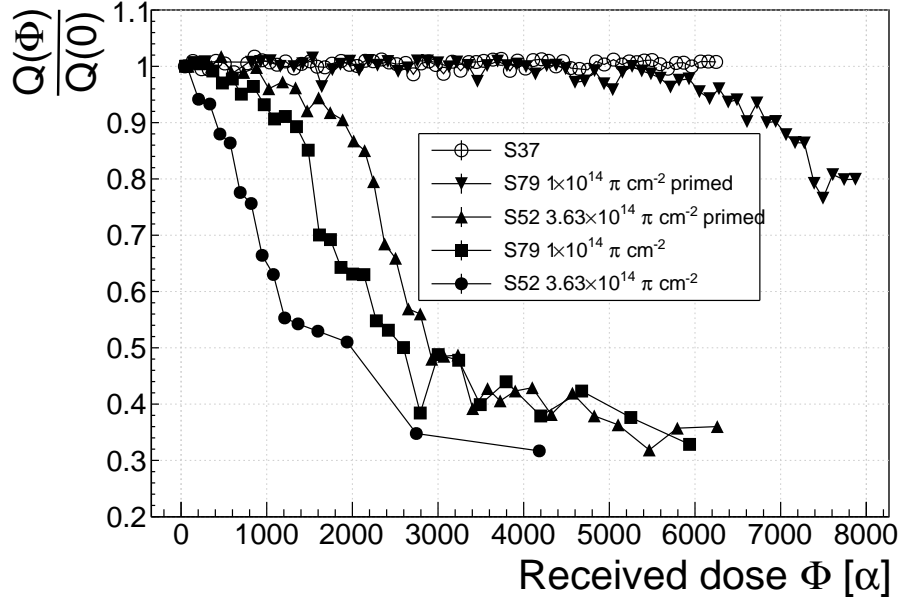


Figure 3.9: Relative decrease of collected charge with time for non-irradiated and irradiated diamond samples.

1361 recombine with the adjacent electrode. Taking into account that the diamond bulk
1362 has been damaged by irradiation, these two phenomena might have an effect on the
1363 operation of the detector on a macro scale.

1364 The first test has been carried out using the Cx spectroscopic amplifier, with
1365 the bias voltage of the samples set to +500 V. Figure 3.9 shows the results of 6500
1366 recorded hits at a rate of ~ 7 particles per second. The collected charge $Q(\Phi)$ for
1367 the non-irradiated sample is stable as compared to the initial collected charge $Q(0)$
1368 (plotted as a relative value $\frac{Q(\Phi)}{Q(0)}$). It is expected that the irradiated samples will have
1369 a lower charge collection efficiency than the non-irradiated sample. However, their
1370 initial efficiency suddenly drops after a certain period of time. The initial efficiency
1371 after priming with β particles is higher than that without priming, but eventually it
1372 deteriorates again. In addition, the spread of measured energies increases significantly.
1373 Finally, the particle counting rate decreases with the decreased efficiency.

1374 To investigate this sudden drop in efficiency, the current pulse shapes using a
1375 C2 current amplifier have to be observed (see figure 3.10). The shape of the pulse
1376 holds more information about the charge carrier properties in the sensor than solely
1377 the value of the integrated charge. This time only the primed S79 sample has been
1378 tested. Both hole and electron collection are observed to determine whether they
1379 behave differently or not. The sample has been measured long enough for the pulse
1380 shapes to start changing. The data in figures 3.10 show that the initially stable pulses
1381 start deteriorating – suddenly several different shapes start appearing, some still very
1382 similar to those from the beginning while the others with almost zero amplitude.

1383 Some charges get stopped in the charge traps in the bulk for a long time, building

3.3. RADIATION LIMITATIONS

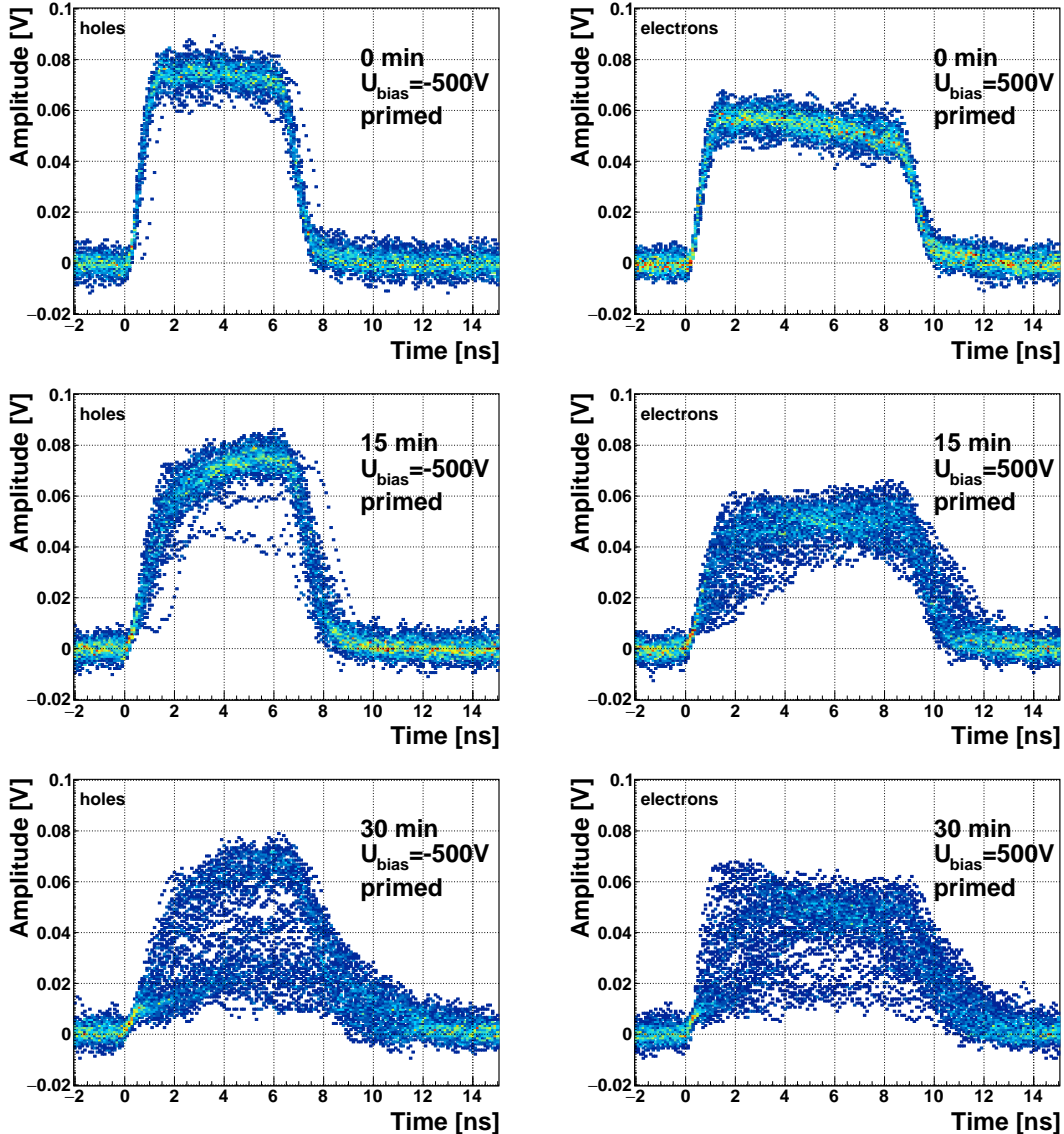


Figure 3.10: The signal of the irradiated and primed S79 deteriorates with time for both polarities. Every plot contains 60 superimposed pulses.

1384 up regions of space charge. The built up space charge affects the electric field, making
 1385 it non-uniform. The non-uniform field in turn affects the drifting carriers, slowing
 1386 them down or speeding them up, depending on the field gradient. Since the movement
 1387 of the carriers is inducing the electric current, the field gradient can be observed in
 1388 the signal.

1389 The second test with the C2 current amplifier has been carried out as follows: At
 1390 the beginning of the test when the diamond is still operating stably, 60 pulses are
 1391 recorded. An average pulse is calculated. This is a reference pulse for the subsequent
 1392 measurement points. Then an RMS of the single pulses with respect to the reference
 1393 pulse is calculated and the values are summed together (σ_{ref}).

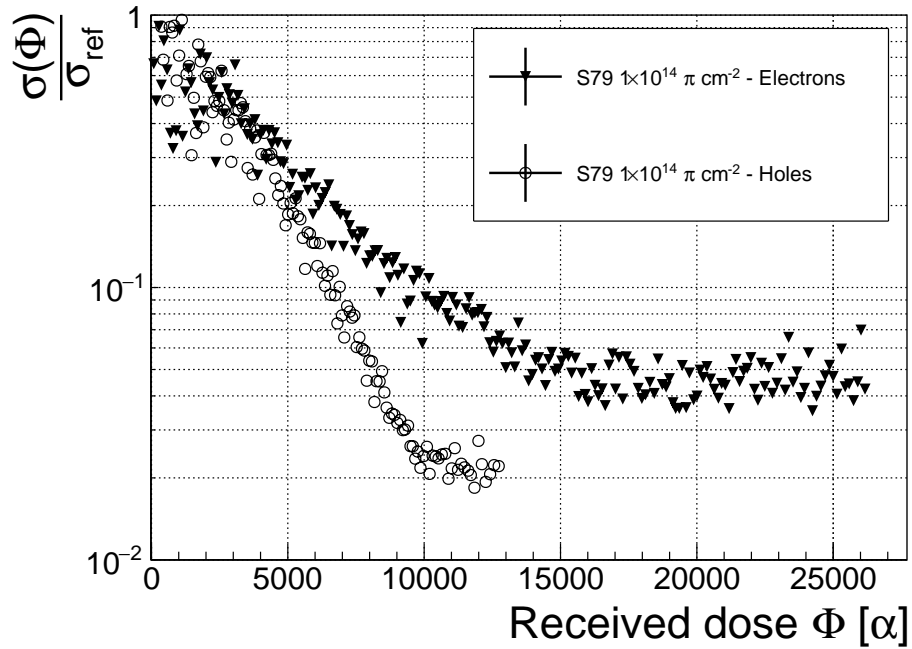


Figure 3.11: Deterioration of the pulse shapes with time

1394 All the subsequent data points also consist of a set of 60 pulses. At every data point
 1395 the summation of the RMS values of the individual pulses with respect to the initial
 1396 averaged pulse is calculated (σ). The ratio between the initial σ_{ref} and discrete values
 1397 σ gives a measure of change of the pulse shape with respect to the reference pulse at
 1398 the start of the measurement. Figure 3.11 shows the ratio $\frac{\sigma_{\text{ref}}}{\sigma(\alpha \text{ dose})}$. From the data
 1399 obtained it can be concluded that initial pulse shape quickly starts deteriorating. In
 1400 fact, the deterioration of the shape follows an approximate exponential decay function,
 1401 which can be fitted to the data. The resulting decay constants for electrons and holes
 1402 are $\tau_e = (4400 \pm 150) \alpha^{-1}$ and $\tau_h = (3300 \pm 140) \alpha^{-1}$. The electrons retain the initial
 1403 shape for longer. The deteriorated shapes also seem to be for a factor of 2 better
 1404 than those of the holes.

1405 Finally, an effort has been made to find a way for the pulse shapes to return to
 1406 their initial state. Five methods are listed:

- 1407 1. Removing the source and leaving the bias voltage switched on,
- 1408 2. Removing the source and switching the bias voltage off,
- 1409 3. Priming with γ at a rate of $400 \text{ s}^{-1} \text{cm}^{-1}$ without applied bias voltage,
- 1410 4. Priming with β at a rate of $1000 \text{ s}^{-1} \text{cm}^{-1}$ with applied bias voltage and
- 1411 5. Priming with β at a rate of $1000 \text{ s}^{-1} \text{cm}^{-1}$ without applied bias voltage.

1412 The diamond sample S79 is first primed using a ^{90}Sr source for about one hour.
 1413 Then the bias voltage is switched on and an ^{241}Am source is put on top. The pulses

3.4. TEMPERATURE LIMITATIONS

produced by the incident α particles have a proper rectangular pulse at the beginning, but then start changing – first gradually and later increasingly more in an erratic way, as described in the text above. After approximately 30 minutes, one of the methods is tested. When a “healing” procedure is started, a set of 60 pulses is taken at irregular points of time to observe the change in the pulse shape and to assess the quality of the “healing” procedure. Then the bias voltage is switched off and the sample is primed again to reset its state before starting with the next run.

The results depicted in figure 3.12 show that the methods (3) and (5) improve the shape, method (2) helps slowly, (1) does not show any change with time and (4) at first improves, but then significantly degrades the shape. The effect observed in method (4) has already been described in [32]. The “healing” process therefore depends on the rate of radiation, the bias voltage and the time of exposure. The ionising radiation creates free charges, which quickly recombine close to the place of generation. It is likely that they also release the charges trapped during the measurement, reducing the overall effect of the space charge. The traps get filled with both flavours of carriers, thus they are neutralised. The pulse shape gradually returns to its initial state.

Procedure	Source	Bias voltage	Effectiveness
1	/	ON	no
2	/	/	slow
3	^{60}Co	/	YES
4	^{90}Sr	ON	no
5	^{90}Sr	/	YES

Table 3.2: Effectiveness of healing procedures

In summary, the shape of the pulses caused by α radiation changes with time for irradiated samples. The shape of the pulses gets distorted and becomes erratic. Charge collection decreases and its spread increases. This happens even faster for non-primed diamonds. To “heal” the diamond – to bring the pulse shapes back to their initial shape – the sample must be primed using a β or a γ source for several minutes at the bias voltage set to 0 V. Switching to the inverse polarity for a few seconds helps a bit, but in a long run distorts the signal, which cannot get back to its initial shape.

3.4 Temperature limitations

A test has been carried out to evaluate the effect of temperature changes on the output signal of the diamond sensors. A cryostat filled with liquid helium is used to cool down the sensor during the measurement process. The current signal response to α -particles is measured at 18 temperature points between 4 K and 295 K. At every temperature point, a set of 300 pulses is read out at various bias voltages. Resulting data show that the charge collection is stable down to 150 K, where it starts decreasing and stabilises again at about one third of the initial value at 75 K. This behaviour was first measured and discussed by H. Jansen [28].

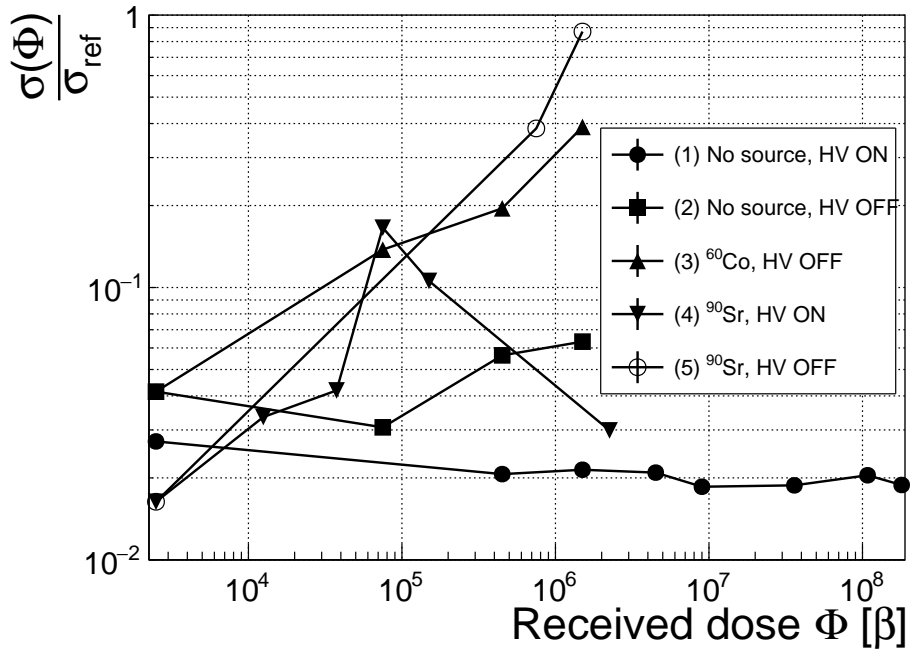


Figure 3.12: Five procedures for the “healing” process for an irradiated diamond that was exposed to α radiation at bias voltage switched on for at least 30 minutes at a rate of 10^4 s^{-1} .

The band gap energy in diamond is equal to $E_g = 5.5 \text{ eV}$ while the average energy to produce an electron-hole pair is $E_{e-h} = 13.25 \text{ eV}$. This means there is excessive energy deposited in the diamond bulk. The incident α -particle stops within $\sim 10\text{--}15 \mu\text{m}$ of the bulk, transferring all its energy to the lattice during deceleration. A part of this energy directly ionises the carbon atoms, creating free electron-hole pairs. The positively charged hole and the negatively charged electron in the hole attract each other via the Coulomb force and may undergo a bonding process during which a phonon is emitted.

The remaining energy, however, is converted into lattice vibrations (phonons [45, 28]). This means that the lattice within the ionisation volume (approximately $\sim 15 \mu\text{m} \times \sim 2 \text{ nm}$ in size) is briefly heated up. The hot plasma then cools down to the temperature of the surrounding material by heat dissipation, (i.e. phonon transport). The free electron binds the free hole into a bound state (not recombination) – the exciton [33]. The exciton binding energy is 80 meV. At higher temperatures, the lattice provides enough energy to excite the electron from the exciton state back to the conduction band. At lower temperatures, however, the exciton lifetime increases, which means that it will take a longer time for the electrons to get re-excited to the conduction band. The re-excitation lifetime at room temperature is $\sim 30 \text{ ps}$, increasing to $\sim 150 \mu\text{s}$ at 50 K [28]. This means that some of the bound electrons will not even start drifting within the period of $\sim 10 \text{ ns}$, which is the expected carrier drift time. When they are finally freed, the current they induce is already hidden in the electronics noise.

3.4. TEMPERATURE LIMITATIONS

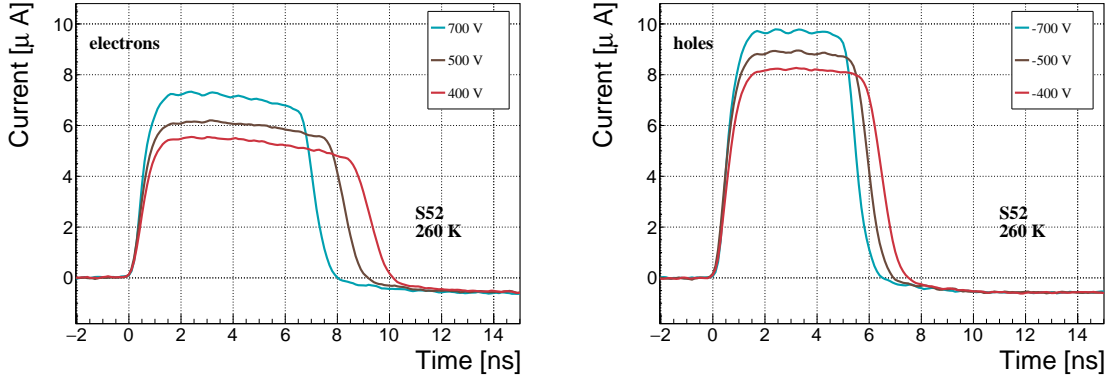


Figure 3.13: Varied bias voltage at a fixed temperature

1470 The effective area of the observed current pulse is therefore smaller than that of a
 1471 pulse induced by all the carriers drifting at the same time. This in effect reduces the
 1472 measured collected charge. The longer the time constant, the lower the measured
 1473 collected charge, as shown in figure 3.17 below.

1474 3.4.1 Temperature-variant α -TCT before irradiation

1475 Three sCVD diamond samples have been tested at a range of temperatures using
 1476 the α -TCT technique. At each temperature point, the bias voltage is set to several
 1477 positive and negative values. A set of 300 pulses is recorded at every data point
 1478 and averaged offline. The resulting averaged pulses of sample S37 at the 260 K
 1479 temperature point and a bias voltage of ± 400 V, ± 500 V and ± 700 V are shown in
 1480 figure 3.13. The pulses induced by holes as charge carriers are shorter than those
 1481 induced by electrons, which means that holes travel faster in diamond. The area of
 1482 the pulse, however, is the same for both polarities, which corresponds to the fact that
 1483 the same amount of charges is drifting in both cases.

1484 Figure 3.14 shows pulses at a bias voltage set to ± 500 V across the range of
 1485 temperatures between 4 K and 295 K – room temperature (RT). Several conclusions
 1486 can be drawn by observing their shape. First, the pulse shapes change with decreasing
 1487 temperature. The pulse time gets shorter, hinting at the faster carrier drift velocity
 1488 v_{drift} . Second, between 150 K and 75 K there is a significant change in shape - the
 1489 time constant of the rising edge increases significantly and the pulse area decreases.
 1490 From 75 K down to 4 K there is no significant observable change. Last, the top of
 1491 the pulse at the S52 is not flat, which means that a portion of the drifting charge is
 1492 lost along its way. This is due to charge trapping, likely by means of crystal defects
 1493 or impurities.

*CHAPTER 3. EXPERIMENTAL RESULTS
DIAMOND IRRADIATION STUDY*

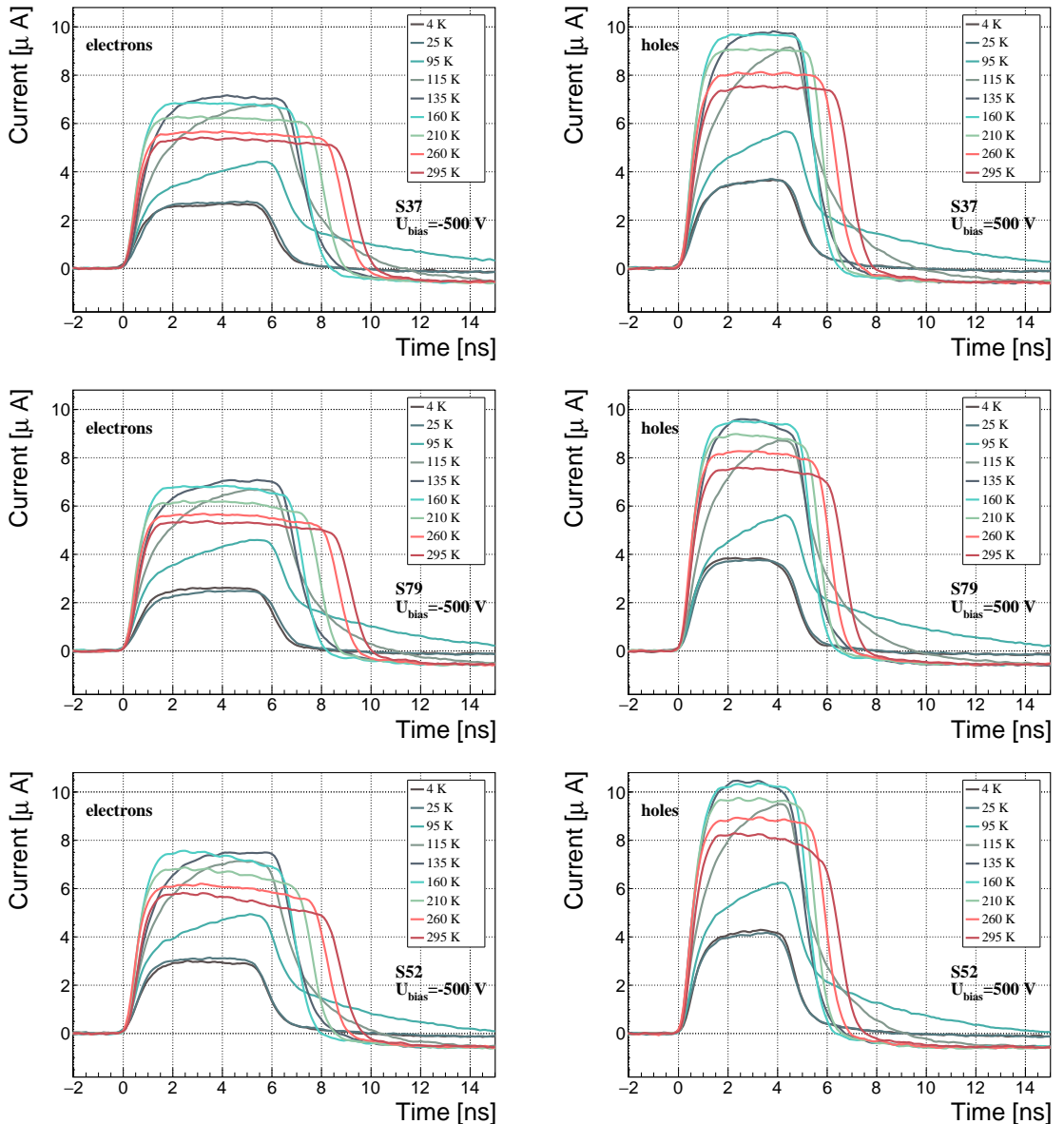


Figure 3.14: Several data points between 4 K and 295 K at a bias voltage of ± 500 V

3.4. TEMPERATURE LIMITATIONS

3.4.2 Temperature-variant α -TCT after irradiation

The irradiated S79 and S52 have been re-tested in the cryostat after irradiation. The aim was to see how their pulse shapes change with decreasing temperature, in particular the decaying top of the pulses (see figure 3.15). The decay time gives information on trapping of charge carriers while travelling through the diamond bulk. A variation of the decay time constant as a function of temperature might help to reveal the type and depth of the charge traps. To observe these effects or lack thereof, a number of requirements has to be met. First, the diamond samples are intentionally not primed prior to the experiment because priming would improve the pulse shapes and possibly change the decay time constant of the signal. Second, keeping in mind that the pulse shape of irradiated diamonds changes with time, the duration of the measurement of an individual data point has to be short – of the order of 30 seconds. Last, the sequence of the bias voltage settings is important, the reason for which is explained below.

Unfortunately it is not possible to avoid temporal pulse changes. For instance, one measurement point takes approximately one minute. After the measurement, the bias voltage polarity is swapped for a few seconds to bring the diamond back into its initial state. But a few seconds with respect to a minute is not enough. Therefore, when the bias voltage is set to the next value, there is still some residual effect of the previous measurement. Similar to the effects of polarisation, this effect is also decreasing the pulse height. This can be observed in figure 3.15, which shows the resulting pulses of S52 for bias voltages of ± 200 V, ± 300 V, ± 400 V and ± 500 V at 230 K and 260 K. In this case the measurements sequence is: 230K (200 V, 300 V, 400 V, 500 V, -500 V, -400 V, -300 V), 260 K (-200 V, -300 V, -400 V, -500 V, 500 V, 400 V, 300 V). The changes in pulse shapes for holes at 230 K and 260 K cannot be attributed to the temperature change. Instead, the explanation could lie in diamond “polarisation”. This means that, when exposed to an electric field with α measurements ongoing, the diamond builds up an internal electric field of inverse polarity, which effectively reduces the overall electric field. This internal field does not dissipate when the external bias voltage is switched off. It can be said that the diamond becomes “polarised”. When switching the polarity of the external bias voltage, the internal and external electric field point in the same direction at the beginning, increasing the overall electric field and with it the pulse height. In figure 3.15, this happens when switching from 500 V (figure 3.15a) to -500 V (figure ??) at 230 K. The built up polarisation contributes to the pulse having a sharp rising edge and a high amplitude. This effect decays during the next two voltage points. There would be a handful of ways to avoid this polarisation effect in the data:

1. After every data point invert the bias voltage and leave it to return to a neutral state for the same amount of time,
2. Make a hysteresis of data points, going from minimum negative to maximum positive bias several times,

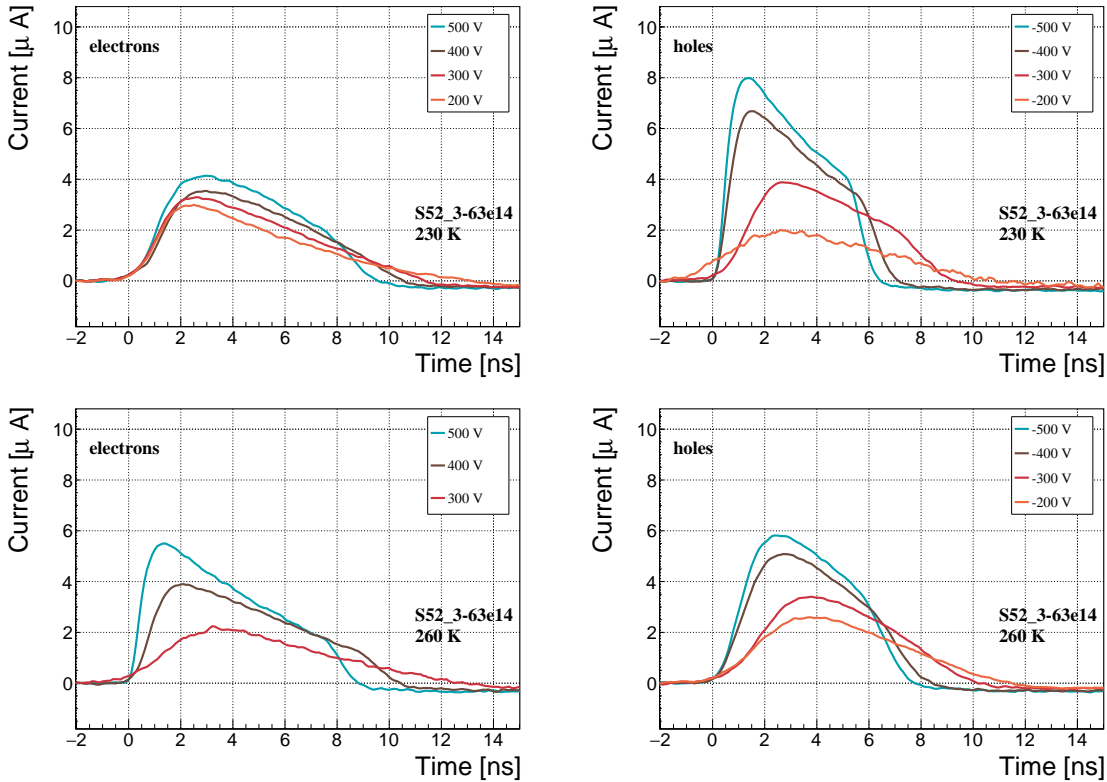


Figure 3.15: Varied bias voltage at a fixed temperature for an irradiated sample

1536 3. Reduce the measurement time at every bias voltage setting.

1537 Unfortunately, options (1) and (2) are very time consuming and would increase the
1538 overall experiment time to over one day. The third option would worsen the resulting
1539 averaged pulses. In the end an alternative option was chosen: alternating the start-
1540 ing bias voltage and the sequence at every temperature point. With this option, a
1541 meaningful systematic error in analysing the pulse shapes can be attained.

1542 Figure 3.16 shows the irradiated S52 and S79 as well as the non-irradiated S37
1543 for comparison, all at a bias voltage of ± 500 V and at several temperature points
1544 between 4 K and RT. It is evident that the radiation damage affected the shape of
1545 the pulses across all temperatures.

1546 3.4.2.1 Collected charge as a function of temperature

1547 The area below the current pulse is proportional to the charge collected by the dia-
1548 mond detector. The collected charge is observed as a function of temperature. First,
1549 the amplitude values of the averaged pulses at a bias voltage of ± 500 V and across the
1550 temperature range between 4 K and 295 K have to be integrated. Then a calibration
1551 factor is used to derive the charge for all data points. This factor is obtained using
1552 a Cx charge-sensitive amplifier. The resulting values for electrons and holes are plot-
1553 ted in figures 3.17a and 3.17b, respectively. Thesis [28] gives a model that explains

3.4. TEMPERATURE LIMITATIONS

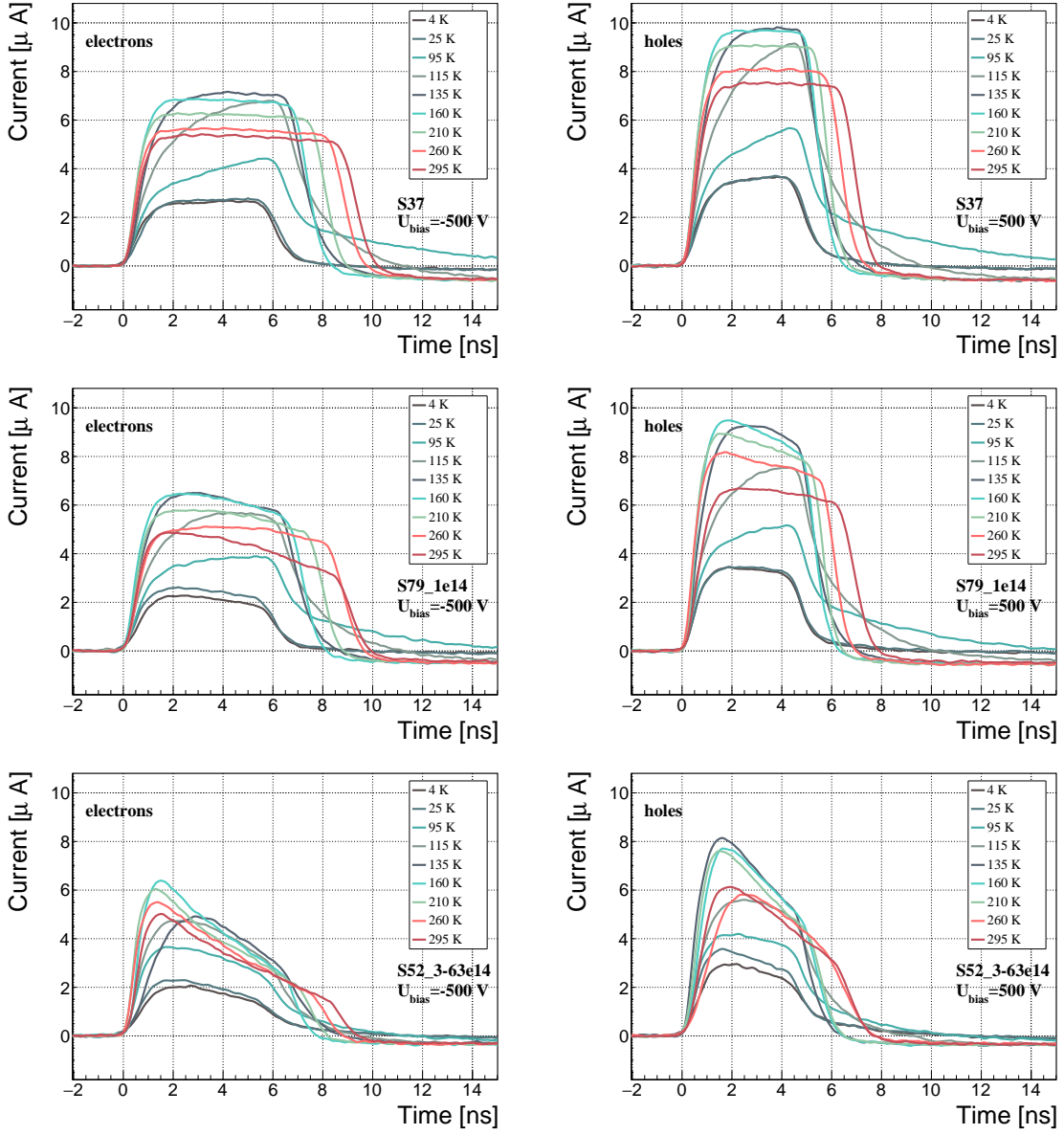


Figure 3.16: After irradiation: several data points between 4 K and 295 K at a bias voltage of ± 500 V

1554 the drop in charge below 150 K. The new contribution are the data points for the
 1555 irradiated samples. The values for them are lower than those of non-irradiated
 1556 samples, which is expected.

1557 The values for all samples are fairly stable in the range between 4 K and 75 K
 1558 and between 150 K and 295 K. However, in the values for the irradiated S52 some
 1559 excursions can be observed. This is due to the sequence of the measurement steps,
 1560 which introduced a hysteresis effect and is explained in the preceding text.

1561 The collected charge drops significantly from 150 K down to 75 K. In the non-
 1562 irradiated samples the values in the lower temperature range are approximately 0.30

of the values at the high range. For the irradiated ones this difference is lower – a factor of 0.35 for S79 and 0.5 for S52. An interesting detail is that the ratio between the values for non-irradiated samples and their irradiated counterparts at the lower range is different than at the higher range. Looking at the values for the electron collection in figure 3.17a: for S52 the lower ratio is equal to 1.28 and the higher equal to 1.7. For S79 these ratios are 1.00 and 1.09, which means that the difference in charge collection between 4 K and 75 K before and after irradiation is negligible.

3.4.2.2 Charge trapping

The carriers drifting through the bulk get stopped by the charge traps with a certain probability. This trapping happens uniformly throughout the diamond, decreasing the number of carriers in the charge cloud. Therefore the absolute number of trapped carriers decreases. At the same time the absolute number of trapped carriers per unit of length decreases. The resulting function for the number of drifting carriers per unit of length is a decaying exponential function:

$$I(t) = I(0) \cdot e^{-\frac{t-t_0}{\tau}} + I_0, \quad (3.6)$$

where $I(0)$ is the initial induced current, I_0 is the end current, t is time, t_0 is temporal displacement of the pulse and τ is the decay time constant. This value tells how long it takes before the amplitude of the pulse decreases to 63 % of its initial height.

The decaying exponential function has been fitted to the decaying top of the averaged pulses at bias voltages of ± 400 V and ± 500 V across all temperatures excluding the transitional range between 75 K and 150 K. The resulting decay time constants τ for an individual temperature point are not equal, which stems from the fact that the pulses change with time due to “polarisation”. This counts as a systematic error. Therefore the fitted τ for ± 400 V and ± 500 V are averaged into one value representing the measurement at that temperature point. Figure 3.18a shows the fitted τ for the five samples between 4 K and 295 K. In principle, the time constants should be infinite for a perfect and non-irradiated sample. Here a slightly tilted top of the pulse due to space charge is already successfully fitted with an exponential function, resulting in a τ of the order of (200 ± 20) ns⁻¹. Consequently the fitting method is not adequate for non-irradiated samples. For the irradiated samples, the fit becomes increasingly more meaningful. As seen in figure 3.18a, the fitted values of the irradiated samples are fairly stable across all temperatures. There is a slight increase in the decay time constant of the S52 from (6.0 ± 0.5) ns⁻¹ above 150 K to (8.5 ± 0.9) ns⁻¹ below 75 K. On the other hand, this step is not observable in the S79 data. With only one sample exhibiting this behaviour, the effect is not significant enough. Judging by the data acquired, the samples would need to be irradiated to doses above $1 \times 10^{14} \pi \text{ cm}^{-2}$ to quantify this effect in detail. So far this effect will not be regarded as significant for the scope of this thesis. Building on this assumption, the conclusion is that the signal decay time constant for irradiated sCVD diamond is constant across the temperature range between 4 K and 195 K, excluding the transitional range between 75 K and 150 K.

3.4. TEMPERATURE LIMITATIONS

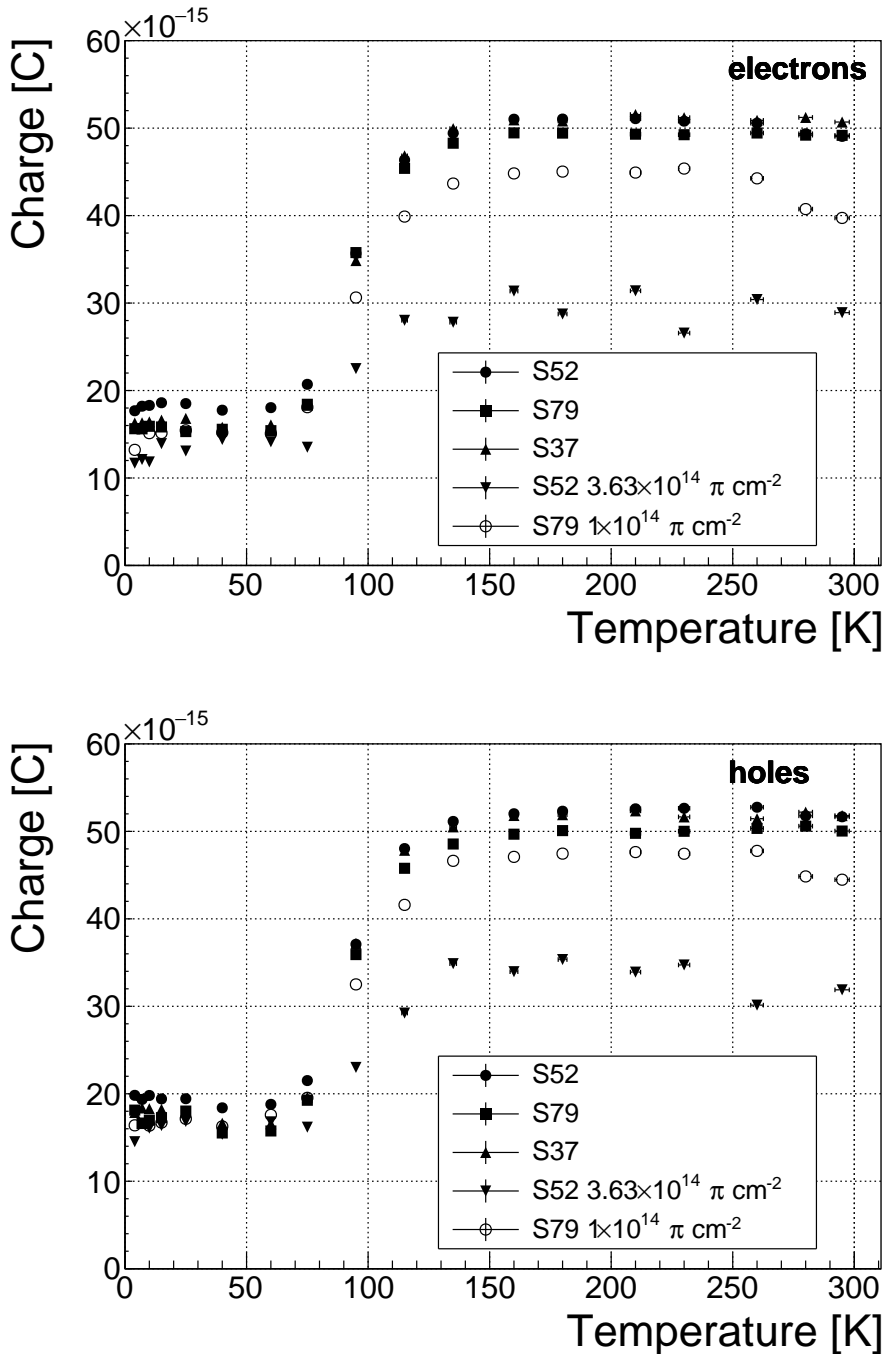


Figure 3.17: Collected charge as a function of temperature

¹⁶⁰³ Taking into account the conclusions above, all the values can be averaged into one
¹⁶⁰⁴ decay constant. Figure 3.18b shows these values for all samples as a function of the
¹⁶⁰⁵ received $\pi_{300 \text{ MeV}}$ radiation dose. To estimate the carrier lifetime with respect to the
¹⁶⁰⁶ radiation dose received, a similar model is used than that in section 3.5. This model
¹⁶⁰⁷ states that the inverse of the carrier lifetime is linearly decreasing with increasing

CHAPTER 3. EXPERIMENTAL RESULTS
DIAMOND IRRADIATION STUDY

1608 radiation dose:

$$\frac{1}{\tau} = \frac{1}{\tau_0} + \kappa_\tau \cdot \Phi \quad (3.7)$$

1609

$$\tau = \frac{\tau_0}{\kappa_\tau \tau_0 \Phi + 1} \quad (3.8)$$

1610 where τ_0 is the lifetime for a non-irradiated sample (real lifetime, therefore of the order
1611 of 400 ns^{-1}), τ is the lifetime of an irradiated sample, Φ is the received radiation dose
1612 and κ_τ the lifetime degradation factor. For these data the fitted factor is equal to
1613 $\kappa_\tau = (3.6 \pm 0.8) \times 10^{-16} \text{ s cm}^2 \pi_{300 \text{ MeV}}^{-1}$. Using this factor, the steepness of the decay
1614 in the pulse shape with respect to radiation dose can be estimated. This can help
1615 when designing a system where current pulse shape is an important factor.

3.4. TEMPERATURE LIMITATIONS

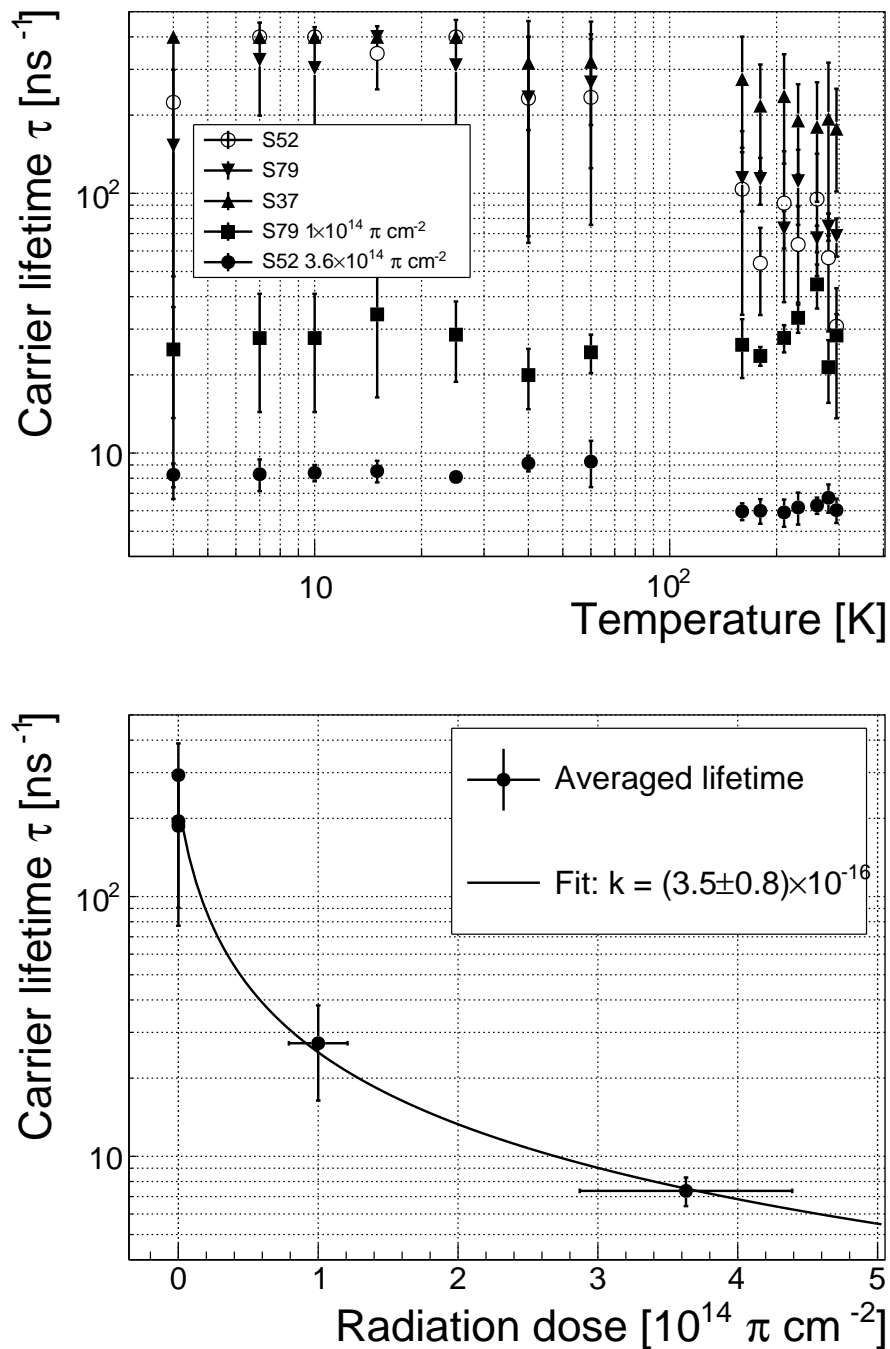


Figure 3.18: Charge carrier lifetime decreases with irradiation, but is stable across the range of temperatures between 4 K – 75 K and 150 K – 295 K. The first figure shows the carrier lifetime τ as a function of temperature whereas the second figure depicts the carrier lifetime averaged over all temperatures and plotted against the π irradiation dose

1616 **3.5 Conclusion**

1617 This chapter gives an overview of the capabilities and limitations of diamond as
1618 a particle detector. Three effects on diamond were studied – noise, radiation and
1619 temperature, the focus being on the latter two.

1620 Two sCVD diamond detectors were irradiated with 300 MeV pions. They were
1621 tested alongside a non-irradiated sample to observe the changes in the ability to detect
1622 α , β and γ radiation. Their charge collection efficiency was measured in a test beam
1623 facility using . The results were compared to the results from the RD42 collaboration
1624 and a DPA model. A radiation damage factor $k_\lambda = (3.0 \pm 1.0) \times 10^{-18} \mu\text{m}^{-1} \text{cm}^{-2}$ was
1625 obtained for $\pi_{300 \text{ MeV}}$ particles. The data point was not in agreement with the data
1626 provided by RD42 nor with the model. However, the irradiation process and the low
1627 number of tested samples hold a relatively high statistical uncertainty. In addition,
1628 there was no diamond surface treatment done in between the measurements, as is the
1629 case in the study conducted by RD42. The results obtained in the course of these
1630 measurements will also be fed into the existing pool of data in the RD42 collaboration.

1631 The next step was to test the long-term capabilities for α detection. The shape
1632 of the ionisation profile was investigated to determine the behaviour of the charge
1633 carriers in the irradiated diamond. An exponential decay was observed in the pulses
1634 of irradiated samples, proving that there are charge traps in the bulk that were created
1635 during irradiation. Then a long-term stability test was carried out. The results show
1636 that the irradiated diamond detectors do not provide a stable and reliable long-term
1637 measurement of α particles. This might be due to a space-charge build-up in the
1638 bulk, which changes the electric field, affecting the charge carriers. A procedure to
1639 improve the pulse shape using β and γ radiation was proposed.

1640 Finally, the diamond sensors were cooled down to temperatures between 4 K and
1641 295 K. Their response to α particles was observed. The results of the non-irradiated
1642 and irradiated samples were compared. The effect of reduction for the number of
1643 drifting charges due to exciton recombination was observed in both sets of data.
1644 The second set had a superimposed effect of charge trapping during the drift, which
1645 was represented by an exponential decay in the signal. The decay time constant
1646 did not change with temperature. Therefore all temperature points for individual
1647 samples were averaged and the decay time constants were plotted against the received
1648 radiation dose. A damage factor equal to $\kappa_\tau = (3.5 \pm 0.8) \times 10^{-16} \text{ s cm}^2 \pi_{300 \text{ MeV}}^{-1}$ for
1649 non-primed diamonds was defined.

1650

Chapter 4

1651

Charge monitoring

1652

The ATLAS Diamond Beam Monitor

1653 Particle detectors in high energy physics experiments need to meet very stringent
1654 specifications, depending on the functionality and their position in the experiment.
1655 In particular, the detectors close to the collision point are subject to high levels of
1656 radiation. Then, they need to operate with a high spatial and temporal segmentation
1657 to be able to precisely measure trajectories of hundreds of particles in very short
1658 time. In addition, they need to be highly efficient. In terms of the structure, their
1659 active sensing material has to be thin so as not to cause the particles to scatter
1660 or get stopped, which would worsen the measurements. This also means that they
1661 have to have a low heat dissipation so that the cooling system dimensions can be
1662 minimised. Finally, they need to be able to operate stably for several years without
1663 an intervention, because they are buried deep under tonnes of material and electronics.

1664 The material of choice for the inner detector layers in the HEP experiments is
1665 silicon. It can withstand relatively high doses of radiation, it is highly efficient (of the
1666 order of $\sim 99.9\%$) and relatively low cost due to using existing industrial processes
1667 for its production. Its downside is that, with increasing irradiation levels, it needs to
1668 be cooled to increasingly low temperatures to ensure a stable operation. This is not
1669 the case with diamond. In addition, diamond has a lower radiation damage factor,
1670 which means it can operate in a radiation-heavy environment for a longer period.

1671 The ATLAS Diamond Beam Monitor (DBM) [] is a novel high energy charged
1672 particle detector. Its function is to measure luminosity and beam background in the
1673 ATLAS experiment. Given its position in a region with a high radiation dose, di-
1674 amond was chosen as the sensing material. The monitor's pCVD diamond sensors
1675 are instrumented with pixellated FE-I4 front-end chips. The pCVD diamond sensor
1676 material was chosen to ensure the durability of the sensors in a radiation-hard envi-
1677 ronment and the size of its active area. The DBM is not the first diamond detector
1678 used in HEP, but it is the largest pixellated detector installed so far (see figure 4.1).
1679 It was designed as an upgrade to the existing luminosity monitor called the Beam
1680 Conditions Monitor (BCM) [] consisting of eight diamond pad detectors, which is

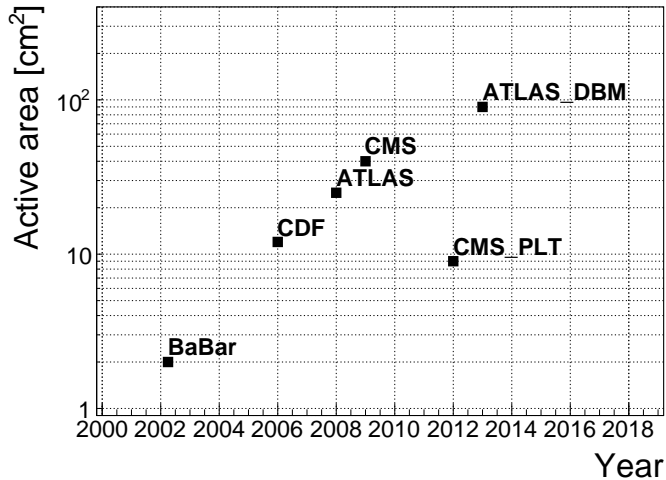


Figure 4.1: Diamond detectors installed in high-energy physics experiments in the last decade, sorted by the active sensor area. The first four detectors from the left are radiation monitors whereas the right two are pixel trackers.

able to perform precise time-of-flight (ToF) measurements. The DBM complements the BCM's features by implementing tracking capability. Its pixelated front-end electronics significantly increase the spatial resolution of the system. Furthermore, the DBM is able to distinguish particle tracks originating in the collision region from the background hits. This capability is a result of its projective geometry pointing towards the interaction region. This chapter first describes the principles of luminosity measurements. It then explains how the DBM will carry out this task. Finally, some results from tests and from the real collisions are presented.

When a particle traverses a sensor plane, a hit is recorded in the corresponding pixel. Thus, a precise spatial and timing information of the hit is extracted. With three or more sensors stacked one behind the other, it is also possible to define the particle's trajectory. This is the case with the DBM. Its projective geometry allows the particles to be tracked if they traverse the sensor planes. The DBM relates the luminosity to the number of particle tracks that originate from the collision region of the ATLAS experiment. Particles that hit the DBM from other directions are rejected as background radiation.

4.1 Luminosity measurements

Luminosity is one of the most important parameters of a particle collider. It is a measurement of the rate of particle collisions that are produced by two particle beams. It can be described as a function of beam parameters, such as: the number of colliding bunch pairs, the revolution frequency, the number of particles in each bunch and the transverse bunch dimensions. The first four parameters are well defined. However, the transverse bunch dimensions have to be determined experimentally

4.2. DIAMOND PIXEL MODULE

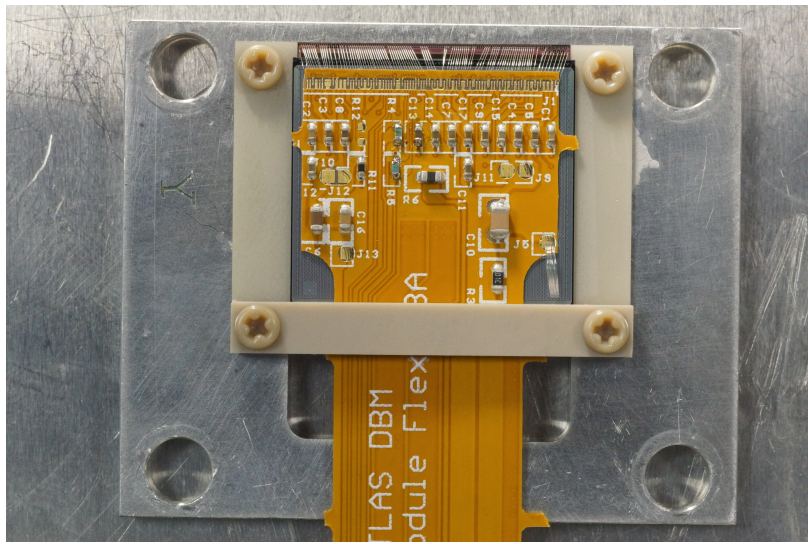


Figure 4.2: DBM module, top-down view. Visible is the flexible PCB with signal and power connections, the silicon sensor and a part of the FE-I4. Wire bonds from the PCB to the FE-I4 and to the sensor are also visible.

1704 during calibration. The ATLAS experiment uses the *van der Meer scan* [1] during
1705 low-luminosity runs to calibrate the luminosity detectors. This scan is performed
1706 by displacing one beam in a given direction and measuring the rate of interactions
1707 as a function of the displacement. Transverse charge density of the bunches can be
1708 estimated on the basis of the interaction rate. The calibrated luminosity detectors
1709 can then operate during high-luminosity runs.

1710 One approach to luminosity monitoring is to count the number of particles pro-
1711 duced by the collisions. The luminosity is then proportional to the number of detected
1712 particles. A detector has to be capable of distinguishing individual particles that fly
1713 from the interaction point through the active sensor area. If the detector has at least
1714 three layers, it can reconstruct the particles' tracks, which in turn yields more infor-
1715 mation on their trajectory. This is one reason why detectors with a high timing-
1716 and spatial segmentation are more suitable for these applications. The second reason
1717 is that, with a high spatial segmentation, the detector will not saturate even at high
1718 particle fluencies.

1719 4.2 Diamond pixel module

1720 The two most important parts of the diamond pixel module (seen in figure 4.2) are
1721 the sensor, which detects ionising radiation, and the pixellated front-end chip, which
1722 collects the ionised charge with a high spatial segmentation, processes the recorded
1723 data and sends them to the readout system. This section describes these two main
1724 parts of the module and their interconnection.

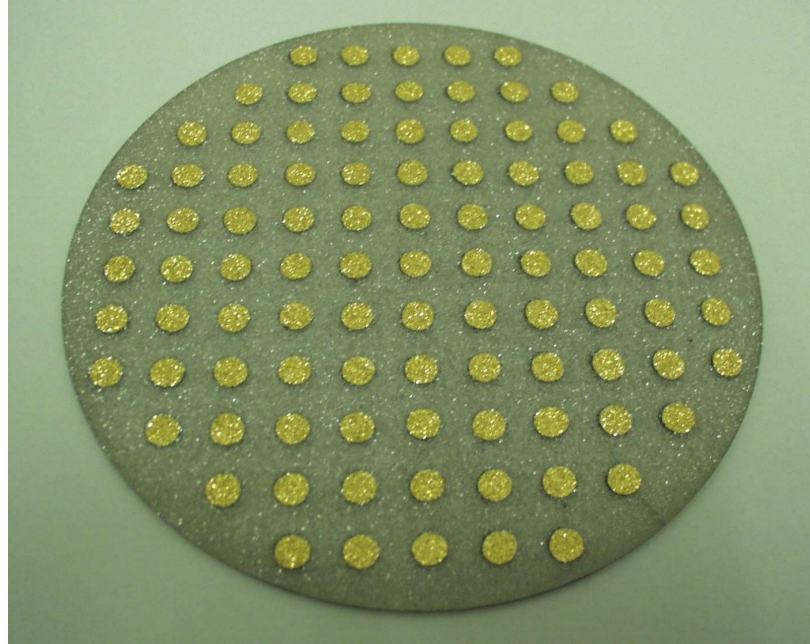


Figure 4.3: A pCVD wafer. The golden dots on the surface are the electrodes that are applied during the qualification test. The wafer is measured across the surface to find the regions with the highest efficiency.

1725 **4.2.1 Sensors**

1726 The DBM modules are instrumented with two types of sensors – pCVD diamond and
1727 silicon. The silicon sensors are used as a fallback solution because there were simply
1728 not enough high-quality diamond sensors available. In addition, a comparative study
1729 of irradiation damage between silicon and diamond can be made with such a hybrid
1730 system.

1731 **Diamond sensors** The target material for this application is pVCD diamond. The
1732 reason for this is that the active area of an individual sensor must be approximately
1733 4 cm^2 , which is too large for the sCVD diamond. pCVD material is also a bit
1734 cheaper, which makes a detector with a large active area more feasible to build. The
1735 material is provided by three companies: DDL, E6 and II-IV and it is grown in
1736 15 cm wafers, as seen in figure 4.3. The target thickness of the wafers is 500 μm and
1737 the minimum required charge collection efficiency is 40 % ($\text{CCD} \geq 200 \mu\text{m}$). They
1738 need to be operated at bias voltages between 600–1000 V. On one side there is a
1739 single gold electrode applied across the whole surface. On the other side a pixellated
1740 metallisation is added.

1741 **Silicon sensors** are standard $n^+ - in - n$ planar sensors with a 200 μm thickness
1742 and were mostly fabricated at CiS [], a company from Erfurt, Germany. They are
1743 designed to have nearly a 100 % efficiency when non-irradiated. Their bulk resistivity
1744 is between 2–5 $\text{k}\Omega\text{cm}$ and they were diffusion oxygenated at 1150 °C for 24 hours to

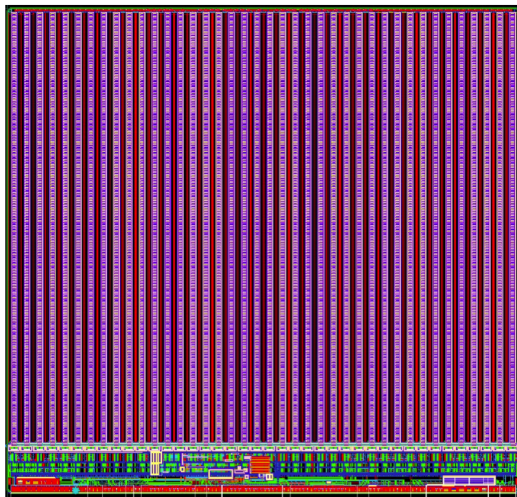


Figure 4.4: FE-I4 layout, top-down view. The pink area are pixels grouped into columns, the green area below is the common logic and the red strip at the bottom are the wire bond pads.

increase their radiation hardness. One side is segmented into pixels. Guard rings at the edges of the sensor provide a controlled drop in potential, reducing the possibility of shorts at maximum design bias voltages of the order of 1000 V.

4.2.2 Front-end electronics

The FE-I4 (front-end version four) [1] is an ASIC pixel chip designed specifically for the ATLAS pixel detector upgrade. It is built as a successor to the current pixel chip FE-I3, surpassing it in size of the active area ($4\times$ larger) as well as the number of channels/pixels ($10\times$ more). 336 such FE-I4 modules are used in the newly installed pixel layer called the Insertable B-Layer (IBL) [2]. The DBM is also instrumented with these chips. The FE-I4's integrated circuit contains readout circuitry for 26880 pixels arranged in 80 columns on a $250\text{ }\mu\text{m}$ pitch and 336 rows on a $50\text{ }\mu\text{m}$ pitch. The size of the active area is therefore $20.0\times16.8\text{ mm}^2$. This fine granularity allows for a high-precision particle tracking. The chip operates at 40 MHz with a 25 ns acquisition window, which corresponds to the spacing of the particle bunches in the LHC. It is hence able to correlate hits/tracks to their corresponding bunch. Furthermore, each pixel is capable of measuring the deposited charge of a detected particle by using the Time-over-Threshold (ToT) method. Finally, the FEI4 has been designed to withstand a radiation dose up to 300 MGy. This ensures a longterm stability in the radiation hard forward region of the ATLAS experiment.

Each pixel is designed as a separate entity. Its electrical chain is shown in figure 4.5. The bump-bond pad – the connection to the outside of the chip – is the input of the electrical chain, connected to a free-running amplification stage with adjustable shaping using a 4-bit register at the feedback branch. The analog amplifier is designed to collect negative charge, therefore electrons. The output is routed through

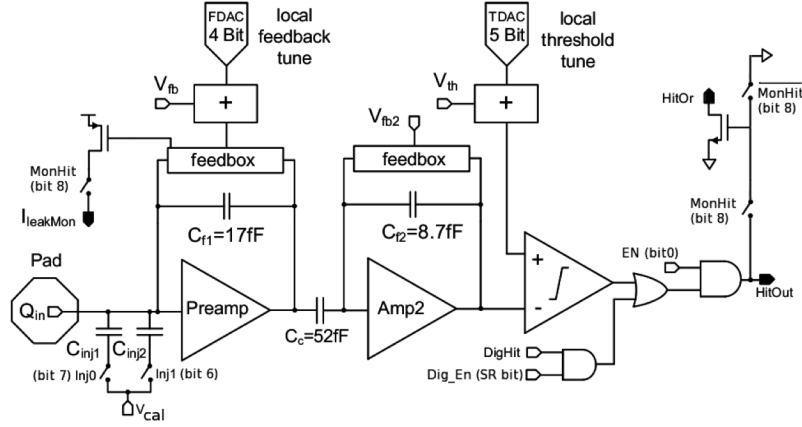


Figure 4.5: Schematic of an analog pixel. Courtesy of the FE-I4 collaboration.

1769 a discriminator with an adjustable threshold. This value in effect defines the level at
 1770 which the circuit will detect a hit. In addition, there is a counter of the clock cycles
 1771 (25 ns sampling) during which the signal is above the discriminator threshold. The
 1772 value of the counter is proportional to the collected charge. The logic gates at the end
 1773 of the chain are used to enable/disable the pixel and to issue a so-called HitOr flag –
 1774 this signal is set whenever at least one of the pixels was hit and is used as a trigger
 1775 for the readout. The output of the chain – HitOut – is routed into the logic of the
 1776 chip where it is buffered and eventually sent out to the readout system. The module
 1777 receives all its commands from the system via a 40 MHz LVDS line. The commands
 1778 are either settings for the pixel registers or triggers that start the data readout. The
 1779 data are sent via an LVDS line at up to 320 Mbit/s, but by default at 160 Mbit/s,
 1780 four times faster than the clock of the device. This allows the chip to clear out its
 1781 buffers before new data are recorded, thus avoiding dead time and data pile-up. The
 1782 FE-I4 has been successfully tested for trigger rates of up to 300 kHz.

1783 The DBM uses pCVD diamond with $d_C = 500 \mu\text{m}$ thickness and silicon with
 1784 $d_{Si} = 200 \mu\text{m}$ thickness as a sensor material. The resulting most probable value
 1785 (MPV) of the deposited charge for a minimum ionising particle (MIP) is calculated
 1786 with the formula $Q_S = d \cdot E_{e-h}$ and equals 18000 electrons and 17800 electrons,
 1787 respectively, at a full charge collection efficiency. Unfortunately this is not the case
 1788 with the pCVD material, whereby the expected charge collection efficiency is of the
 1789 order of 50 % – around 9000 e. This value further decreases with received irradiation
 1790 dose. Therefore in order to detect the particles depositing energy on the far left side
 1791 of the landau spectrum, the threshold has to be set to a significantly lower value.
 1792 On the other hand, if the threshold set too low, it also detects the electronic noise
 1793 and stores a false noisy hit. With the typical noise amplitudes being in the range of
 1794 120–200 e, a safe threshold range would be between $Th = 1000\text{--}3000$ e. The target
 1795 for the DBM is to lower the threshold down to 800 e.

1796 The analog amplifier is implemented in two stages to get a fast rise time at a low
 1797 noise and a low power consumption. The output signal of the analog amplifier has a

4.3. MODULE ASSEMBLY AND QUALITY CONTROL

triangular shape with a fast rise time and a long decay. The shape can be adjusted by tuning the amplifier feedback loop. Its length is proportional to the collected charge, but it needs to be calibrated first. This is done by means of two injection capacitors, $C_{\text{inj}1}$ and $C_{\text{inj}2}$, seen in figure 4.5 with well defined capacitances. First, the charge $Q_{\text{cal}} = V_{\text{cal}} \cdot (C_{\text{inj}1} + C_{\text{inj}2})$ is injected into the analog chain. Then the length of the output pulse is measured and finally the feedback value is changed to either lengthen or shorten the pulse in order to get to the required duration t_{cal} . The typical values are $Q_{\text{cal}} = 5000 - 16000$ e at the time $t_{\text{cal}} = 5 - 10$ ToT. The target values depend on the sensor, the type of a radioactive source and the application. Therefore the initial threshold Th at 1 ToT and the calibrated value Q_{cal} at t_{cal} ToT give us a linear scale of collected charge with respect to time over threshold. However, in practice this relation is nonlinear for lower thresholds, but since the goal of the measurements is to track the particles rather than to measure their deposited energy precisely, this is sufficient.

4.3 Module assembly and quality control

Parts for the detector arrived separately and were assembled into modules at CERN’s DSF lab after being checked for production faults. The assembled modules underwent a series of quality control (QC) and burn-in tests to determine their quality, efficiency and long-term stability.

4.3.1 Assembly

A single-chip module consists of a pixel module, a flexible PCB and the supporting mechanics (a ceramic plate and an aluminium plate). The chip arrives already bump-bonded to the sensor, be it diamond or silicon. First it is glued to the ceramic plate on one side and to the PCB on the other using either Araldite 2011 or Staystik 672/472. The choice of glue was a topic of a lengthy discussion. Staystik is re-workable and has a very high thermal conductivity. The latter is important because the FE-I4 chips tend to heat up significantly and need a good heat sink. The problem is that it has a curing temperature of 160/170 °C. This temperature may cause some unwanted stress build-up between the FE-I4 and the diamond sensor due to different coefficients of thermal expansion, pulling them apart. This would disconnect the pixels, yielding large regions of the module insensitive to radiation. To avoid this, an alternative glue was tried. Araldite 2011 can be cured at lower temperatures – down to RT – but it has a lower heat conductivity. In the end Araldite is used as the safer option. However, due to the longer curing, the whole assembly process using Araldite is extended to two working days. After curing, the module is wire-bonded and attached to the aluminium plate using screws made up of a radiation-resistant PEEK plastic. They have to be tightened with a great care, because their screw head is only 0.2–0.6 mm away from the sensor edge – the sensor displacement tolerance during gluing is of the order of 0.5 mm. Finally, the module is put in an aluminium carrier which protects

1837 it from mechanical damage or electrostatic discharges.

1838 **4.3.2 Testing**

1839 The modules are tested in the lab using an RCE readout system and a moving stage
1840 with two degrees of freedom. They are placed onto the stage and connected to the
1841 readout system and the power supplies. After ensuring the low- and high voltage
1842 connectivity they are checked for the signal connectivity. If everything is operational,
1843 a series of automated tests is run. Each of these tests calibrates a certain value within
1844 a pixel, whether it is the signal threshold or the value for integrated charge. These
1845 are tuned in a way that the response to a predefined calibration signal is uniform for
1846 all pixels across the sensor. This procedure is referred to as *tuning*.

1847 When the modules are tuned, they are tested using a ^{90}Sr radioactive source. Two
1848 things are checked: 1) operation of all pixels and 2) sensor efficiency. The first test
1849 is carried out by moving the module slowly under the source while taking data so
1850 that the whole surface is scanned uniformly. The resulting occupancy map reveals
1851 any pixels that are not electrically coupled to the sensor via bump bonds. This is an
1852 important step in the DBM QC procedure, because it turned out that a significant
1853 portion of the flip-chipped diamond sensors exhibited very poor connectivity. The
1854 disconnected regions on the faulty modules ranged anywhere from 0.5–80 % of the
1855 overall active surface. In two cases the sensor was even completely detached from the
1856 chip. Therefore the pixel connectivity turns out to be the most important qualification
1857 factor in the QC procedure. Unfortunately the only way to check it at the moment is
1858 to fully assemble a module and test it using a radioactive source. If the module turns
1859 out to be of poor quality, it is disassembled and sent for rework. The turnover time
1860 of this operation is of the order of one month, which affected the DBM installation
1861 schedule significantly.

1862 Only the modules that passed the pixel connectivity test undergo the second
1863 test stage in which the sensor’s efficiency was estimated. A scintillator is placed
1864 underneath the module and is used as a trigger. A particle that crosses the DBM
1865 module and hits the scintillator, triggers the module readout. In the end, the number
1866 of triggers is compared to the number of hits/clusters recorded by the module. The
1867 resulting ratio gives an estimate of the sensor’s detection efficiency. The real sensor
1868 efficiency can only be measured in a particle beam and using a beam telescope as a
1869 reference detector. Nonetheless, the *pseudo-efficiency* gives a rough estimate of the
1870 sensor’s quality.

1871 The results for the DBM QC are shown in section 4.4. All in all, 79 modules went
1872 through the QC procedure – 43 diamond modules and 36 silicon modules, 12 of the
1873 latter only for testing purposes. Figure 4.6 shows their production with time. 18
1874 diamond modules and 6 silicon modules were in the end chosen to be made up into
1875 DBM telescopes and installed into ATLAS.

1876 A very important issue is the so called erratic current. This term describes the
1877 leakage current in a pCVD diamond that becomes unstable. It can develop gradually

4.3. MODULE ASSEMBLY AND QUALITY CONTROL

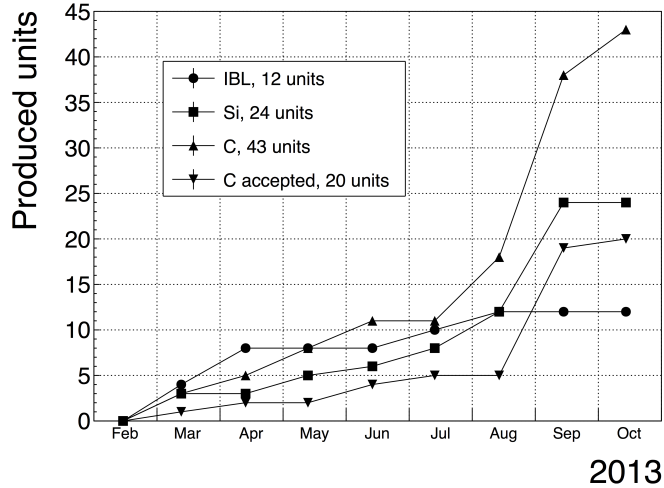


Figure 4.6: Module production with time

or can be triggered with a β source. Spikes appear in the otherwise stable leakage current. They can be up to three orders of magnitude higher than the base current. Sometimes the current also suddenly increases for a few orders of magnitude and stays at that level (e.g. from the initial 1 nA to 3 μ A). The amplitude differs in magnitude from sensor to sensor. This effect is still not fully explained, but the hypothesis is that the charges find a conductive channel along the grain boundaries, causing discharges. These discharges are picked up by the pixel amplifiers in the FE-I4. A single discharge can trigger a group of up to \sim 500 pixels, resulting in a *blob* on the detector occupancy map. Sometimes the conductive channel stays in a conductive state, making one or more pixels always to fire. These pixels only use the bandwidth of the readout channel, so they have to be masked out during measurements.

4.3.3 Installation and commissioning

The DBM modules that passed the QC tests were assembled into telescopes – sets of three modules one behind the other with a spacing of 50 mm. Of the 18 diamond and 6 silicon modules, 6 diamond and 2 silicon modules were built. A special care was taken when choosing the sets of three diamonds. The modules with a similar pseudo-efficiency, leakage current, maximum stable high voltage and shape of disconnected regions were grouped together. After assembly into telescopes, the modules were tested for their connectivity. Then the high voltage was applied and the leakage current was observed. This was an important point to check because all three modules shared the same high voltage channel. Any instabilities on one of the modules would cause problems on the other two. This would for instance happen if one of the modules had a much lower breakdown voltage.

Due to time constraints, the telescopes were not built at the same time but instead the production was pipelined. As soon as two telescopes were ready, they were transported to Point 1 – the site where parts of the ATLAS detector were being put

1904 together. There they were prepared for installation onto the pixel detector struc-
1905 ture that had been extracted from ATLAS due to pixel detector commissioning. The
1906 commissioning was nearing completion, so the technicians were preparing the detec-
1907 tor for re-insertion. The cylindrical structure was being closed off by four new service
1908 quarter-panels (nSQPs). This meant that with every day the access to the place
1909 of installation of the DBM was more difficult. The first two telescopes were still put
1910 into place when only one nSQP was in place. This allowed the installation process
1911 to be carried out from both sides. This proved to be helpful, because the process
1912 was lengthy and had to be done with great precision. It involved tightening several
1913 screws on both sides of the telescopes, adding thermal paste on the aluminium joints
1914 and removing the protective covers, revealing the fragile wire bonds. At the same
1915 time the surrounding electronics and cables had to be left untouched. The lessons
1916 learnt with the first part of the installation were helpful when installing the other tele-
1917 scopes. The last two were fitted onto the structure when three nSQPs were already
1918 in place, leaving only a narrow opening for access. The whole procedure was carried
1919 out blind. After every installation, the telescopes were tested again. First, the low
1920 voltage connectivity was checked and a set of tests was run on the FE-I4 front-end
1921 chips. An eye diagram was made to estimate the quality of the signal transmission.
1922 Then a ^{90}Sr source was used to perform a source test on three modules at the same
1923 time. Leakage current was observed during the source test. The final test included
1924 running four telescopes (all on one side) at a time. All the tests were successful and
1925 the DBM was signed off.

1926 **4.4 Performance results**

1927 This section gives an overview of the performance results of the DBM modules
1928 achieved during the QC and the test beam campaign. The source tests were per-
1929 formed to check for disconnected regions in the sensors and to measure the diamond's
1930 pseudo-efficiency. Only the modules with minimal disconnected regions and maxi-
1931 mum pseudo-efficiency were chosen for installation.

1932 **4.4.1 Source tests**

1933 All modules went through the same procedure when tested using a ^{90}Sr source – to
1934 check for disconnected regions and to measure the pseudo-efficiency.

1935 The setup consisted of a placeholder for the ^{90}Sr source, an X-Y moving stage
1936 with a holder for the module and a scintillator with a photomultiplier placed below
1937 the source and the module. The scintillator was used as a trigger – when it detected a
1938 particle, it triggered the readout of the module. If the module was placed in between
1939 the source and the scintillator, the particle had to traverse the module to hit the
1940 scintillator. Therefore, in the case of a module with a 100 % efficiency the triggered
1941 data read out by the module would need to contain at least one hit in the module. In
1942 reality the β particles scatter around the setup and sometimes hit the scintillator from

4.4. PERFORMANCE RESULTS

1943 other directions, without incident the module. This produces empty triggers. The
1944 phenomenon sets the limitation of measuring with a radioactive source as compared
1945 to the measurements in a test beam, in which the particles in principle always travel
1946 in one direction and their scattering is minimal.

1947 The test for disconnected regions was carried out by moving the module under the
1948 source in X and Y direction so that the exposure over the whole plane was uniform.
1949 This resulted in an occupancy scan seen in figures 4.7a and 4.7b. The silicon module
1950 had a very uniform occupancy plot. So much so that the features of the overlaying
1951 flexible PCB can be observed. The rectangular shadows are the passive components
1952 whereas the lines are the traces in the PCB. Furthermore, a circular-shaped edge of
1953 the PCB can be seen on the bottom right side of the plot. These darker areas are
1954 such because fewer electrons can penetrate the material with a high density. In the
1955 case of the diamond, the features of the PCB can be observed as well, but are much
1956 less distinguishable. In principle, the plot is much more granulated – less uniform.
1957 This high variance in the diamond’s detection ability is due to the grain boundaries
1958 in the pCVD material which trap the drifting charges, rendering some regions much
1959 less efficient.

1960 The pseudo-efficiency test was carried out by placing the module directly below the
1961 source and collimating the particles so that their trajectory was incident the module
1962 in the middle. For every trigger by the scintillator, a script checked whether there
1963 was a hit recorded in the module or not. The resulting ratio between the number
1964 of triggers and number of hits recorded in the module is a pseudo-efficiency – an
1965 estimation of the sensor’s efficiency. It cannot give a precise value due to the triggers
1966 produced by scattered particles, but at least gives a rough estimate.

1967 Figure 4.8a shows the distribution of disconnected regions across all tested mod-
1968 ules. Silicon modules were performing as expected, with a minimum number of dis-
1969 connected pixels. The majority of the silicon modules yielded the pseudo-efficiency
1970 of $(94.3 \pm 0.2) \%$. Silicon sensors being 99.99 % efficient, this value was underesti-
1971 mated by about 5 %. The measured pseudo-efficiency of the diamond modules was
1972 $(65 \pm 7) \%$, with outliers down to 10 %. The value depended on the diamond quality,
1973 the set threshold and the applied bias voltage. The latter two settings were varied to
1974 check the behaviour of the modules under various conditions.

1975 4.4.2 Test beam results

1976 The first two assembled prototype DBM modules, MDBM-01 and MDBM-03, were
1977 tested at DESY, Hamburg, in a test beam facility. The aim of the measurements was
1978 to measure their efficiency, the spatial distribution of the efficiency and the effect of
1979 the beam on the disconnected regions. A silicon module MSBM-02 was measured to
1980 crosscheck the measurements. Since the silicon module is almost 100 % efficient, it
1981 was used as an “anchor” – the efficiency of the diamond module was measured relative
1982 to that of the silicon module. Two beam telescopes were used as reference systems:
1983 Kartel [], built by JSI institute from Ljubljana, and EUDET Aconite []. Both are

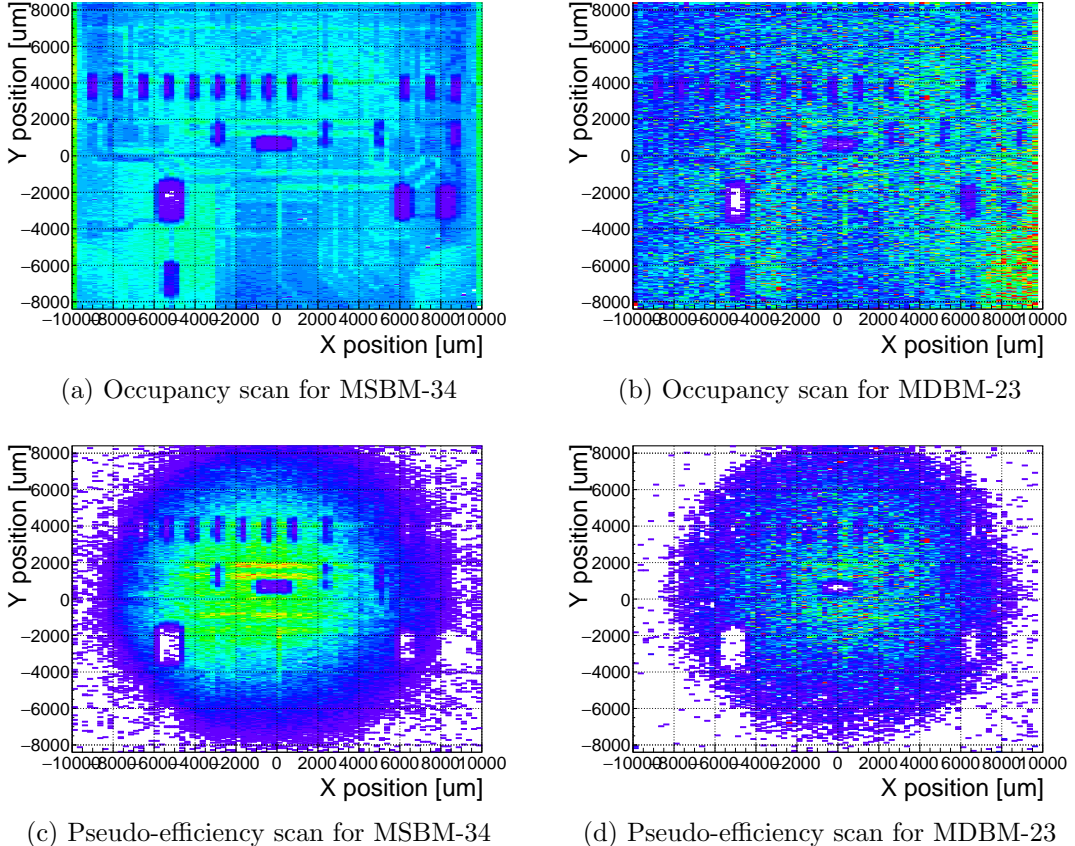


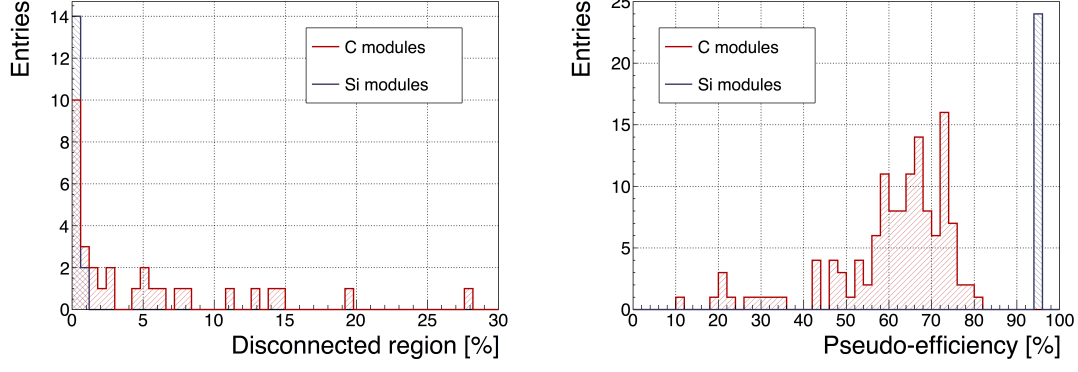
Figure 4.7: Occupancy and pseudo-efficiency scans for the silicon (left) and diamond sensor (right) to check for disconnected regions and estimate the sensor’s efficiency. Shadows of the electronic components are clearly visible because fewer electrons were able to traverse through such a higher amount of material.

instrumented with six Mimosa26 pixel planes and capable of tracking particles with a $2 \mu\text{m}$ pointing resolution.

The test beam prototypes did not meet the acceptance criteria for production DBM modules in the following areas: first, the stated CCDs were slightly below $200 \mu\text{m}$, which would be the DBM minimum. Secondly, the applied bias voltages ranged from $1\text{--}2 \text{ V}/\mu\text{m}$. In addition, the threshold cut could only be set to 1500 electrons, which is higher than the DBM minimum (1000 e). Nonetheless, the resulting module efficiencies were still in the range between 70–85 %.

To analyse the test beam data, Judith [] software framework was used. Judith is capable of synchronising data streams from several detector systems only connected via a trigger system, reconstructing tracks and calculating efficiency for the DUTs. It was also used to reconstruct and analyse the acquired Kartel test beam data together with the silicon and diamond module as DUTs. A sample of the analysed data is shown in figures 4.9a and 4.9b.

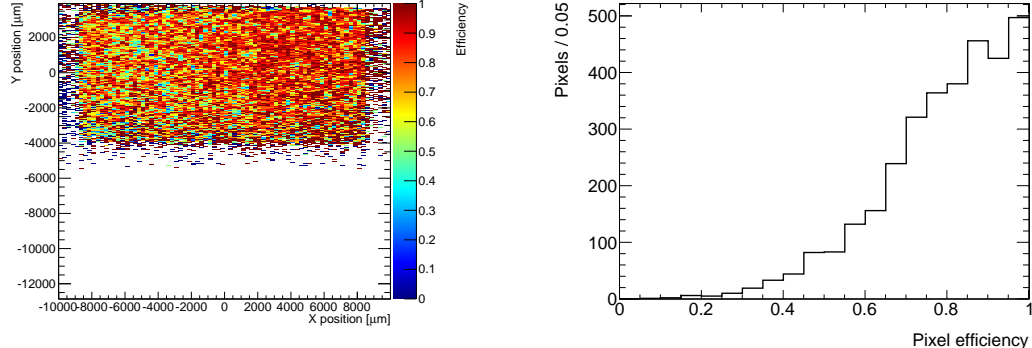
4.5. OPERATION



(a) Disconnected regions for all modules derived from the occupancy scans

(b) Pseudo-efficiencies for all modules at various threshold and voltage settings

Figure 4.8: Measurements of pseudo-efficiency and disconnected regions for all modules that went through the QC procedure



(a) This is an efficiency distribution. Each bin corresponds to a single pixel. The triggering scintillator of the Kartel telescope was smaller than the DUT. Hence, the recorded hits can only be seen in the top half of the sensor.

(b) Pseudo-efficiencies for all modules at various threshold and voltage settings

Figure 4.9: An efficiency study of a prototype DBM diamond module in a test beam. The statistics are low (~ 10 hits/pixel) as the data was collected during a short run.

1998 4.5 Operation

1999 4.5.1 Positioning

2000 The DBM is placed in the forward region of the ATLAS detector, very close to the
 2001 beam pipe (see figure 4.11). The mechanical structure that holds the sensor planes is,
 2002 due to its shape, referred to as a DBM telescope. A telescope is a system that consists
 2003 of several pixel sensors placed in series one behind the other. Each DBM telescope
 2004 houses three diamond pixel modules. Eight DBM telescopes reside approximately
 2005 1 m away from the collision region, four on each side. They are tilted with respect



Figure 4.10: This photo highlights four telescopes installed onto the nSQPs and around the pipe

2006 to the beam pipe for 10°. This is due to a specific phenomenon connected to erratic
2007 (dark) currents in diamond. Studies have shown [1] that the erratic leakage currents
2008 that gradually develop in diamond can be suppressed under certain conditions. For
2009 instance, if a strong magnetic field is applied perpendicular to the electric field lines
2010 in the diamond bulk, the leakage current stabilises [2]. The DBM was designed to
2011 exploit this phenomenon. The magnetic field lines in the ATLAS experiment are
2012 parallel to the beam. Hence, an angular displacement of the sensor with respect to
2013 the beam allows for the leakage current suppression. However, the DBM telescopes
2014 still need to be directed towards the interaction region. Taking these considerations
2015 into account, a 10° angle with respect to the beam pipe was chosen. The influence
2016 of the magnetic field on the particle tracks at this angle is very low as the field lines
2017 are almost parallel to the tracks. The tracks are therefore straight, which reduces the
2018 track reconstruction complexity.

2019 4.5.2 Data taking during collisions

2020 The DBM has been commissioned in ATLAS and is now taking data. Several issues
2021 still need to be resolved regarding the readout systems. Unfortunately, due to issues
2022 with the low voltage power supply regulators, six out of 24 modules were damaged
2023 during operation: four silicon and two diamond modules. The system configured

4.5. OPERATION

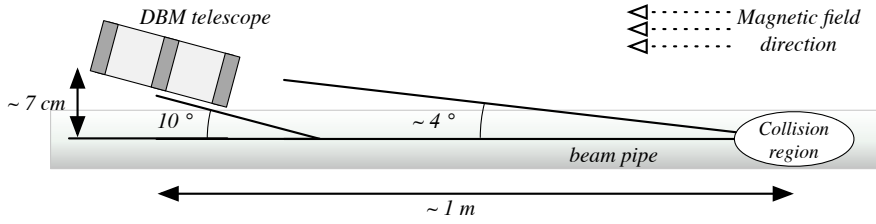


Figure 4.11: Position of the DBM in the ATLAS experiment

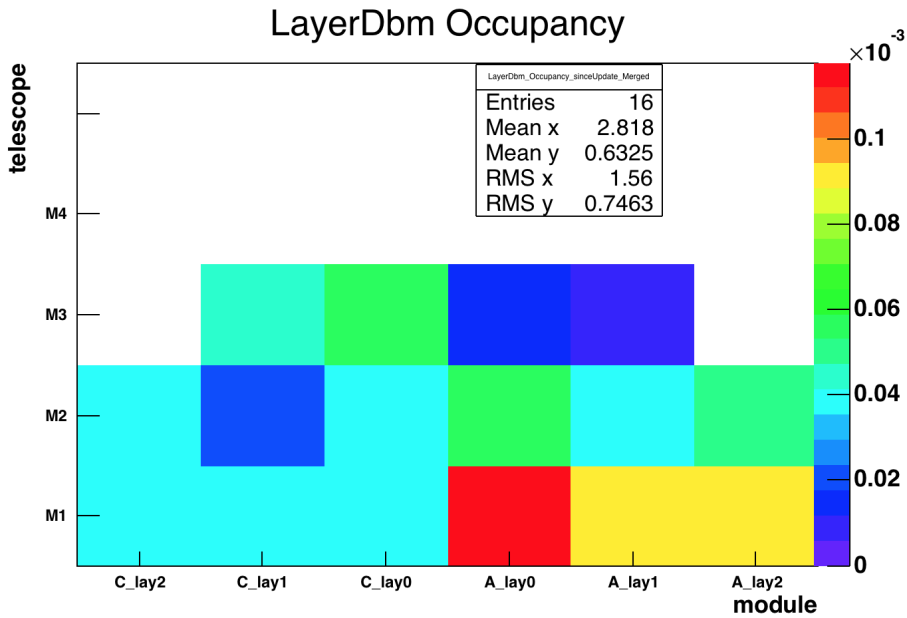


Figure 4.12: Occupancy of individual modules during collisions. Only 16 modules were taking data.

2024 the modules into an unsteady state whereby they drew twice as much current as the
 2025 allowed maximum. This current most probably fused the wire bonds within minutes.
 2026 This has left only five diamond telescopes fully operational. The preliminary data
 2027 obtained using the remaining telescopes show that the background rejection could
 2028 indeed work.

2029 The first step of the system test was to take data during collisions and check
 2030 the occupancy in the individual modules. The occupancies were plotted side by side
 2031 for comparison. Figure 4.12 shows some of the occupancy values. At the time, the
 2032 readout system was not yet configured to read out all telescopes in parallel.

2033 The second step was to test the detector's capability of particle tracking. Only one
 2034 telescope was used to take data with the beam. If all three planes of the telescope
 2035 were hit during a bunch crossing, a linear line was fitted to the hits. This line
 2036 represented the particle's trajectory. It was projected towards the interaction point.
 2037 Two parameters were calculated where the line is the closest to the interaction point:

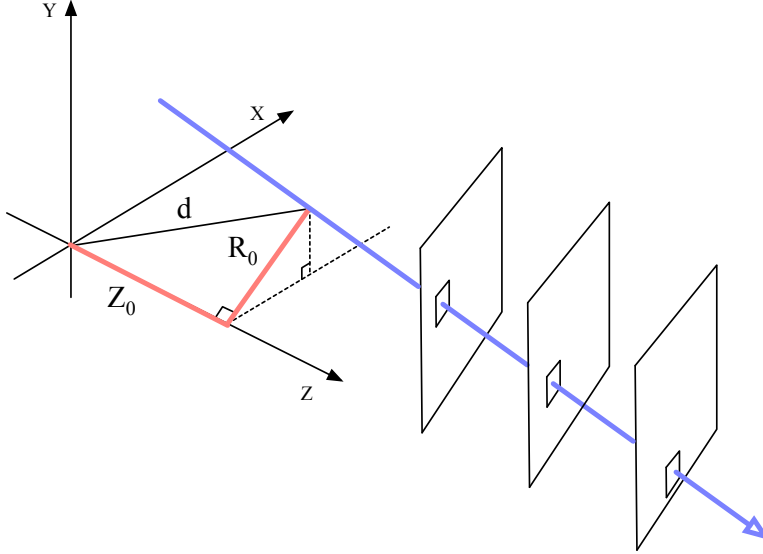


Figure 4.13: A diagram showing the radial distance R_0 and longitudinal distance Z_0 of the trajectory from the interaction point at the minimal distance d . Z is the axis along the beam line. Three module planes intercept a particle and reconstruct its trajectory.

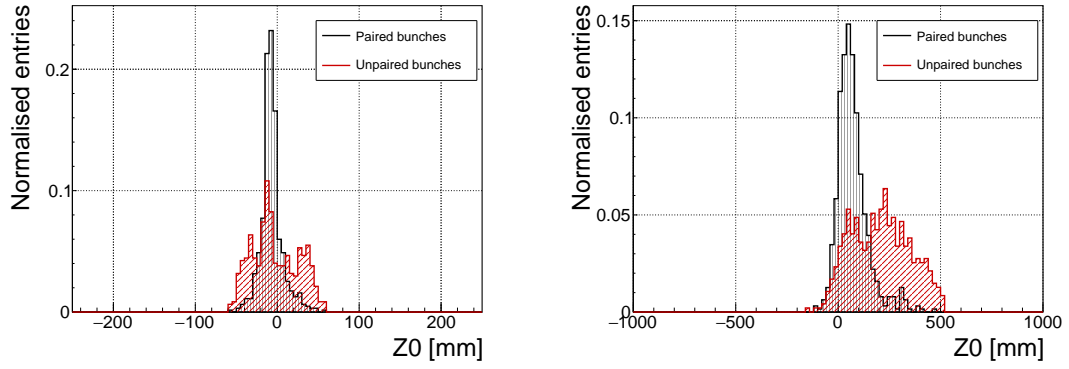
2038 the radial distance and the longitudinal distance between the line and the interaction
 2039 point (see figure 4.13). This was done for the events with two colliding bunches as
 2040 well as for events with only one, non-colliding bunch. The tracks recorded during
 2041 the events with two colliding bunches could either come from the collisions or could
 2042 the background scattering. Tracks recorded during a non-colliding bunch, on the
 2043 other hand, are definitely background particles since, in principle, there should be no
 2044 collisions taking place.

2045 A comparison of the data acquired (see figures 4.14a and 4.14b) showed that, for
 2046 the colliding bunches, the majority of the reconstructed tracks had the origin in the
 2047 interaction point, with an expected spread in Z and R . For non-colliding bunches,
 2048 the distribution is more spread out. In the Z_0 plot the distribution has one peak in
 2049 the middle, which means that the empty RF buckets still held some particles. The
 2050 two peaks on the sides, however, show that a significant number of tracks had their
 2051 origin at the radius of the beam pipe. Therefore these tracks were made by stray
 2052 protons colliding with the beam pipe. These collisions are unwanted as they do not
 2053 produce any meaningful physics while still damaging the ATLAS detector by means
 2054 of the scattered radiation.

2055 4.6 Conclusion

2056 The Diamond Beam Monitor has been designed as an upgrade to the existing lu-
 2057 minosity detectors in the ATLAS experiment. It is the first diamond pixel tracking

4.6. CONCLUSION



(a) Radial distance of the particle trajectories from the interaction point

(b) Longitudinal distance of the particle trajectories (along the beam path) from the interaction point

Figure 4.14: These two plots show two parameters of particle tracks recorded by one of the DBM telescopes: radial and longitudinal distance of the projected tracks from the interaction point.

2058 detector installed in a high-energy physics experiment. The pixelated front-end elec-
 2059 tronic chips ensure precise spatial detection of the charged high-energy particles.
 2060 The projective geometry allows for particle tracking and background rejection. The
 2061 detector is placed in a high-radiation forward region of the experiment. Therefore,
 2062 radiation hardness of the chosen pCVD diamond sensors is an important requirement.
 2063 The tests carried out in the test beam and in the laboratory confirmed that enough
 2064 detector-grade DBM modules have been built to be installed in the experiment. The
 2065 DBM is now running in ATLAS during collisions. Further improvements have to be
 2066 made on the readout firmware before it is included in the main readout stream.

2067

Chapter 5

2068

Current monitoring

2069

Real-time particle identification

2070 Diamond sensors have a very fast signal response due to their low capacitance. The
2071 electrical signal created by drifting charge carriers retains its shape without significant
2072 distortion. When the sensor is used together with a fast current amplifier with a high
2073 broadband limit (~ 2 GHz) and a readout device with a similar limit, the information
2074 about the drifting charges is retained. For instance, a proton creates the free e-h pairs
2075 along its trajectory. The electrons and holes start drifting immediately. Those closest
2076 to the electrodes recombine quickly whereas those at the opposite side contribute to
2077 the induced signal for longer. The resulting signal is therefore a triangular pulse
2078 with a steep rising edge and a gentle falling edge. It is possible to determine the
2079 drift velocity of the charge carriers by measuring the width of the pulse, as was done
2080 in chapter **??**. Furthermore, it is possible to determine with a certain probability
2081 what is the type of incident radiation, judging by the shape of the induced pulse.
2082 This, however, only applies to sCVD diamond material. Its uniform carbon lattice
2083 allows the ionisation profiles to retain their shape, unlike in pCVD material, laden
2084 with grain boundaries, or in even in silicon where the shape is deformed due to p-n
2085 junction non-uniformities.

2086 This chapter describes an application that carries out particle identification by
2087 means of the pulse shape analysis. It was developed for measuring activity of a
2088 neutron reactor. In this case the device has to be able to filter out the photon
2089 background with a rate several orders of magnitude higher than the neutron rate.
2090 Overall detected rate in a neutron reactor can easily exceed 10^8 particles $\text{cm}^{-2}\text{s}^{-1}$,
2091 depending on the distance of the detector from the reactor core. The device has to
2092 be able to cope with such high rates. It also needs to be dead time free or at least
2093 close to that, to minimise the counting error. At these rates, it still has to be able to
2094 identify the types of pulse. This type of online analysis cannot be done in software.
2095 It has to be implemented in an FPGA.

5.1 MOTIVATION

5.1 Motivation

Pulse shape analysis (PSA) is a common software tool for analysing sensor response to incident particles. It is usually done by means of software that runs over big amounts of data that have been acquired and saved to storage. This offline analysis can be repeated and improved. However, the saved data take up a lot of storage space. In addition, saving raw waveform data requires a system capable of a high data throughput and fast data storing. For instance, an oscilloscope can save up to 100 signal waveforms per second. This means that there is a high measurement dead time. To avoid the high dead times, the software algorithms can be ported to the FPGA where they analyse the incoming signal in real time. The signal is then discarded and only the analysis results are saved, decreasing the storage space significantly.

The offline pulse shape analysis has already been used for particle identification with a diamond sensor [29, 24]. An effort has been made to implement an online and real time application for this analysis by porting the algorithms into an FPGA. This section first describes the device specifications Then it describes in detail the PSA algorithms and the structure of the code. Afterwards it discusses the performance results, which showcase the limitations of the device. Finally it describes the data acquired with radioactive sources and in neutron reactors.

5.2 Requirements

Chapter ?? shows that the shape is heavily dependent on several factors, such as environmental temperature and received irradiation dose. At temperatures lower than 150 K the signal from an α starts deteriorating due to recombination of charges in the charge cloud. Sensor irradiation, on the other hand, introduces charge traps, which cause the signal to decay exponentially. These two factors are a significant limitation for particle identification. Priming can improve the charge collection and longterm stability of the pulse shapes. To improve the measurement further, a high bias voltage has to be applied, increasing the measurement SNR.

Factor	Operating range
Sensor material	sCVD diamond
Sensor thickness	500 μm
Temperature	150 K – 400 K
Radiation dose	$1 \times 10^{13} \text{ neq cm}^{-2}\text{s}^{-1}$
Charge carriers	holes
Bias voltage	$\sim 1 \text{ V } \mu\text{m}^{-1}$
Signal-to-noise	5

Table 5.1: Limitations to particle identification

2126 **5.3 Device specifications**

2127 The ROSY box has a single BNC input with the termination $50\ \Omega$ or $1\ M\Omega$ with a
2128 DC or AC coupling. The analog chain has a 250 MHz bandwidth limit. The input
2129 range can be set from $\pm 50\text{ mV}$ up to $\pm 5\text{ V}$. The signal offset can be set to any value
2130 within this range. The ADC samples this signal with an 8-bit precision at a rate of
2131 up to 5 GSPS. The PSA uses the highest sampling to achieve width measurement
2132 resolution of 0.2 ns. The spectroscopic application does not need such a fine timing
2133 resolution and therefore operates at a reduced sampling rate of 0.8 ns. The amplitude
2134 resolution depends on the chosen input range, but at 256 ADC counts per sample, it
2135 can be as low as 0.39 mV s^{-1} at the range of $\pm 50\text{ mV}$ and as high as 39 mV s^{-1} at
2136 the range of $\pm 5\text{ V}$.

2137 The logic structure of the PSA is designed using VHDL and runs on Xilinx Virtex 5. The PSA is capable of a maximum counting rate of 1.56×10^8 pulses per second,
2138 yielding a 6.4 ns double pulse resolution. The analysis is more time consuming; the
2139 maximum throughput rate of the pulse shape analysis is $\sim 5 \times 10^6$ pulses per sec-
2140 ond. This means that after every pulse, the device has a dead time of approximately
2141 (200 ± 15) ns, depending on the width of the pulse being analysed. Any pulse arriving
2142 during the analysis of the previous one will be counted, but not analysed. Any two
2143 pulses with the distance between the rising edges lower than 6.4 ns will be counted
2144 as a single pulse.

2145 The device is very sensitive to noise pick-up. Therefore the setup must be designed
2146 to minimise the pick-up by means of proper shielding, use of high-quality cables etc.
2147 The relatively low bandwidth limit filters out some high-frequency noise, but not the
2148 ringing or higher noise spikes. That is the task for the PSA.

2150 **5.4 Pulse parameters**

2151 A signal pulse on the input is parametrised during the analysis process. The PSA
2152 measures its amplitude, area, width and the slope of its falling edge (see figure 5.1).
2153 The amplitude is the difference between the baseline and the highest sample in the
2154 pulse and is given in ADC counts as an 8-bit value. The area is defined as the sum
2155 of amplitudes of all samples between two defined boundaries within the pulse. The
2156 width is defined as the number of samples with a value higher than a set amplitude
2157 threshold. If the threshold is at half the maximum amplitude, the resulting width
2158 is *full width at half maximum* (FWHM). The falling slope is the maximum negative
2159 difference between values of two samples and is given in ADC counts per sample.
2160 These parameters can also be used as *qualifiers* for accepting or discarding a pulse.
2161 All four parameters limited by the low and high limit are called a *qualifier set*. For
2162 instance, a rectangular pulse by an α particle will always have the same FWHM and
2163 a very steep slope. In comparison, a photon will have a lower falling slope value and
2164 a narrower FWHM. Therefore the low and high cut on these two qualifiers will make
2165 it possible to discriminate between the two pulses. Another qualifier is a *form factor*

5.5. APPLICATIONS

and is defined as the ratio between the measured area and the amplitude multiplied by the width. By comparing the measured and the calculated area the difference between a triangular and a rectangular pulse can be inferred.

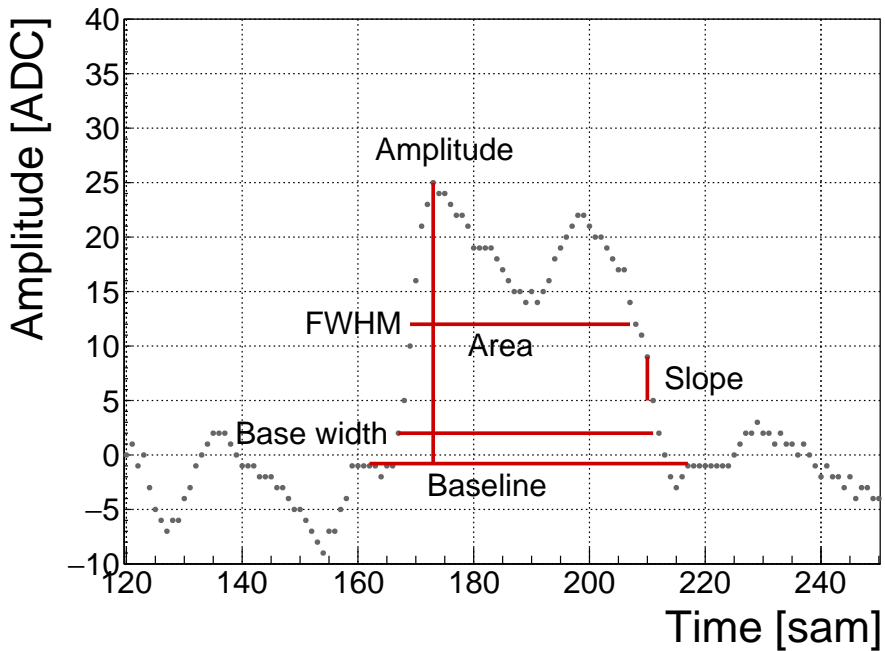


Figure 5.1

5.5 Applications

The FPGA firmware is designed for systems instrumented with CIVIDEC amplifiers and CIVIDEC sVCD diamond detectors. Three applications are available: *Spectroscopy*, *Pulse Shape Analysis* and *Counter*, each optimised for a specific task. Their capabilities are described below. The firmware runs in ROSY, a readout system produced by CIVIDEC.

Spectroscopy is a tool for measuring energy spectra of radioactive sources. It is used in combination with the CIVIDEC Cx spectroscopic charge amplifier. The signal from the charge amplifier is analysed in real time. The FPGA measures the maximum amplitude of the signal. The amplitude value is ready at the end of the pulse and is stored in the amplitude histogram. Immediately after, the analysis is reset and the system is ready for a new acquisition. Upon request from the software, the histogram is read out, during which the analysis is paused. In addition to the histogram building, the firmware can also store raw pulse waveforms, which can be then read out by the software. The maximum allowed throughput is 1 million counts per second.

2185 **Pulse Shape Analysis** is a tool for measuring energy spectra of radioactive sources,
2186 with an additional feature. It can identify the type of radiation detected by the
2187 diamond detector. By means of the pulse analysis it can subtract the background
2188 radiation and only measure the signals from the defined radiation source. It is used
2189 in combination with the CIVIDEC C2 fast current amplifier. The firmware receives
2190 a current pulse from the detector and digitises it. The pulse is then analysed and
2191 parametrised. The analysis module measures its maximum amplitude, full width
2192 at half maximum (FWHM), baseline amplitude, falling slope and its area. Then
2193 it compares the obtained pulse parameters with the qualifiers set by the software
2194 and determines what type of radiation hit the diamond detector. Depending on the
2195 qualifiers, the pulse can either be *accepted* or *rejected*. The firmware then stores the
2196 parameters of the analysed pulse into histograms. Two histograms exist for each
2197 parameter: one for all pulses and one for accepted pulses. In addition, there is one
2198 2D histogram (a scatter plot), which can plot two parameters one with respect to the
2199 other. Upon request from the software, all histograms are read out, during which the
2200 analysis is paused. The maximum allowed throughput is 1 million counts per second.

2201 **Counter** is a tool that measures the count rate and the mean time during counts.
2202 It is used in combination with the CIVIDEC Cx, C6 or C2 amplifier. It contains
2203 one histogram which holds the information about the mean time during counts. The
2204 counter is operational also during the readout of the histogram. The highest counting
2205 rate with enabled histogram writing is $3 \times 10^7 \text{ s}^{-1}$.

2206 5.6 Description of the firmware

2207 The applications are built on top of the Picotech platform. The base code handles
2208 the communication between the software and the hardware. Furthermore, it provides
2209 the interface to the ADC data, the input/output registers and the USB data transfer.
2210 The applications have a set of modules that handle the data input and output and
2211 a module for signal analysis (see figure 5.2).. The data handling modules are very
2212 similar in all the applications to ensure compatibility of the communication between
2213 software and firmware and the readout data format. The analysis module, however,
2214 is different from one application to the other. The data handling layer is the same for
2215 all applications and consists of the final state machine (FSM), the histogram builder,
2216 the raw signal handler, the USB FIFO buffer and the register array.

2217 The firmware is written entirely in VHDL. The diagram in figure 5.2 shows the
2218 module architecture. The ADC provides the module with 32 digitised signal samples
2219 every clock cycle (6.4 ns). The signal is routed directly to the pulse analyser and
2220 into the raw signal handler. The analyser outputs are connected to the I/O registers
2221 and to histogram buffers. Both the histogram buffers and raw signal buffers are
2222 connected to the USB FIFO through a multiplexor. The firmware communication to
2223 the controller is done via input/output (I/O) registers (control and status registers,
2224 counters) and serially via USB (histogram data, waveforms).

5.6. DESCRIPTION OF THE FIRMWARE

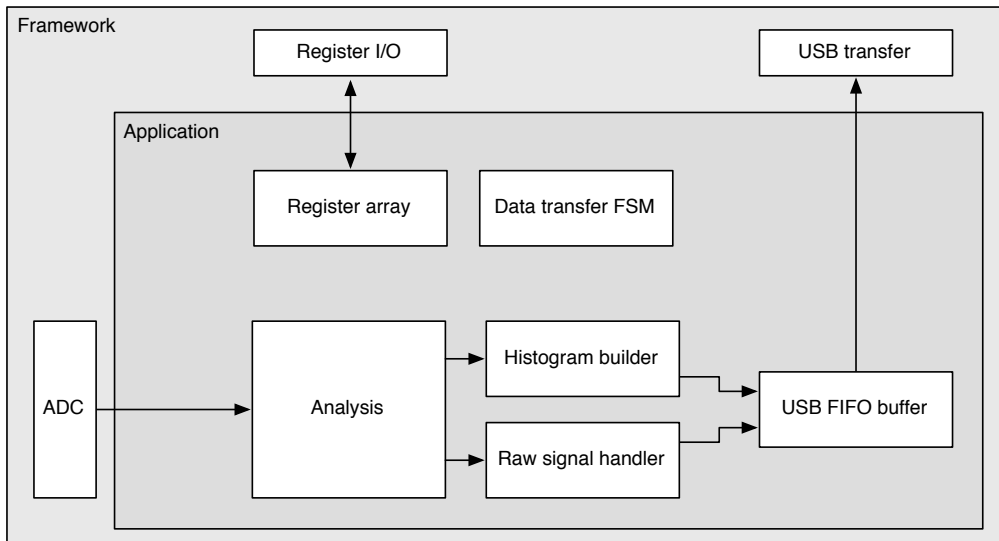


Figure 5.2: Firmware design structure

5.6.1 Design constraints

2225 **Speed** The ADC provides 32 8-bit samples on every 6.4 ns clock cycle. It is not
2226 possible to e.g. sum all 32 values in a single cycle, because the summation takes too
2227 long to complete. This is why the summation has to be pipelined and carried out
2228 in three cycles. This adds up to the analysis duration, which in turn decreases the
2229 maximum pulse rate.

2231 **Firmware size** The PSA application makes use of a number of FIFO and RAM
2232 buffers to store the pulse waveforms and histograms. 48 32k block RAM modules
2233 have been used for the implementation, maxing out the available block RAM memory
2234 space on this FPGA. The analysis algorithm also takes up a significant portion of the
2235 FPGA. Many of the operations are carried out on 256-bit long numbers received from
2236 the ADC, which quickly fills up the available logic. This is also why the place and
2237 route procedure takes a long time.

2238 **Power consumption** The reduction of the power consumption is not crucial for the
2239 intended applications.

2240 5.6.2 Analysis module

2241 This module is different for different applications. The Pulse Shape Analysis (PSA)
2242 application has the most complex module design. The spectroscopy application only
2243 uses a small part of that design and the Counter application an even smaller one.

2244 The analysis (or parametrisation) is carried out in several steps, as shown in
2245 figure 5.3. The triggering block starts the readout upon signal threshold crossing.
2246 The maximum slope of the falling edge is observed. The Amplitude block calculates

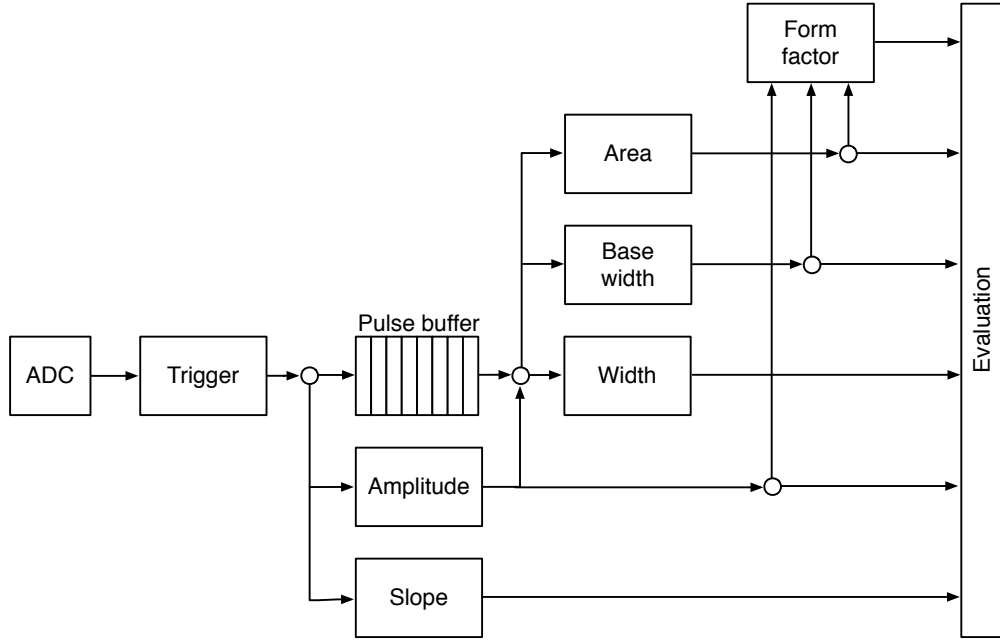


Figure 5.3: Code design plan

the pulse height and retains the maximum amplitude while pushing the signal into the pulse buffer. Then the whole pulse is clocked out of the buffer while its FWHM, baseline width and area are measured. Finally, the Form factor is calculated. At the end the Evaluation block takes in all the parametrised information and classifies the pulse according to user-defined cuts.

Triggering module handles signal polarity swapping, triggering on threshold and defining the trigger window. The real-time processing algorithm allows for a positive or an inverted input signal. However, the PSA only handles positive-polarity pulses. Therefore a negative signal is swapped in the *triggering* block. Signal analysis and readout are then triggered when the signal crosses a user-defined threshold. In addition, the signal has to be over the threshold for a defined number of samples. This is to avoid triggering on noise spikes. A double clock cycle delay is used on the signal to make sure that the recorded signal window will include the rising edge of the pulse as well as some baseline before it. A *trigger active* signal marks a window that contains the whole pulse including some baseline signal before and after it. The trigger can be vetoed by three signals: if the pulse analysis is still taking place, if the input signal exceeds the maximum voltage range or if the data transfer FSM is pausing the analysis due to data transfer to the controller.

Amplitude block calculates the pulse height from the difference between the pulse and the baseline. It also finds the position of the maximum amplitude within the clock cycle. It receives 32 8-bit samples from the triggering block every clock cycle. Time delays in the logic prevent it to find the maximum value of the 32 samples

5.6. DESCRIPTION OF THE FIRMWARE

2269 within one clock cycle (6.4 ns). Therefore the decision logic has been pipelined in
2270 three stages, which means that the final maximum value is ready three clock cycles
2271 after the end of the pulse.

2272 **Pulse buffer** is a FIFO that stores the signal while its amplitude is being measured.
2273 At the end of the pulse the FIFO is read out so that the remaining measurements
2274 can take place.

2275 **Width** block uses the maximum amplitude to determine the *half-maximum* and to
2276 measure the FWHM. To do so, it counts the samples that are above the half-maximum
2277 amplitude. However, this method might also count high enough noise spikes before
2278 or after the pulse. Hence an improved method, which “cleans” the measurement of
2279 unintentional additional noise, has been implemented. It is described in section 5.6.3.

2280 **Baseline width** block is the same as the Width block, but it measures the width
2281 either at 50 %, 25 %, 12.5 % or 6.25 %, depending on the setting in the register. It
2282 also makes use of the special method described in 5.6.3 to avoid overestimations due
2283 to including noise in the measurement.

2284 **Area** block measures the pulse area by summing up the amplitude values of the sam-
2285 ples in the pulse. The boundaries of the summation are defined with the crossing of
2286 the amplitude above a certain threshold. Only the samples between those boundaries
2287 are summed up. The boundaries can be set at 50 %, 25 %, 12.5 % or 6.25 % of
2288 the maximum amplitude of the pulse. The area measurement makes use of the same
2289 routine as the FWHM and Baseline width block to remove the potential outlying
2290 samples.

2291 **Falling slope** block measures the highest negative difference between amplitudes of
2292 two adjacent samples, thus getting the maximum negative slope of the pulse. It is an
2293 experimental routine, only used for academic purposes.

2294 **Form factor** block is used as a special qualifier for particle identification. It com-
2295 pares the weighted measured area of the pulse with its weighted calculated “form”,
2296 which is defined as the multiplication of the measured amplitude and baseline width.
2297 The equation is as follows:

$$x \cdot a - y \cdot A \cdot BW \geq 0, \quad (5.1)$$

2298 where a is the measured area, A is the amplitude, BW is the baseline width and x
2299 and y the weighting factors for the measured and calculated area, respectively. The
2300 output of the block is the boolean result of this equation.

2301 **Evaluation** block takes in all the parameters from the analysis blocks and compares
2302 them against the user-defined qualifiers. If the parameters are within the bounds,
2303 the pulse is accepted, otherwise it is rejected. The corresponding counters within the
2304 block are incremented.

2305 5.6.3 Vector cleaning for area and width measurements

2306 The routine for measuring pulse area and width was designed to improve the mea-
2307 sures with respect to the previous implementation. The core difference is that
2308 the new routine precisely defines the edges of a pulse. It does so by means of *vector*
2309 *cleaning*, presented in figure 5.4. An important input, beside the ADC data and the
2310 measurement threshold, is the position of the sample with the highest amplitude.

2311 The signal arrives from the ADC as a set of 32 8-bit samples every every clock cycle
2312 with a period of 6.4 ns. All 32 samples are compared against the width measurement
2313 threshold. If a sample value is equal or higher than this threshold, a binary 1 is set
2314 in a 32-bit *vector* on the position corresponding to the position of the sample in the
2315 incoming ADC data set. The resulting vector might also include some noise at the
2316 edges of the pulse, depending on the height of the width measurement threshold. The
2317 old routine simply counts the binary ones in this vector to get the pulse width. This
2318 works well for measuring the FWHM because the threshold was high. However, for
2319 width measurements at 25 %, 12.5 % or 6.25 % of the pulse height this might already
2320 become a problem, because the noise might be counted in as well. This is why the
2321 new routine cleans the outliers in this vector before counting the remaining ones in
2322 the clean vector.

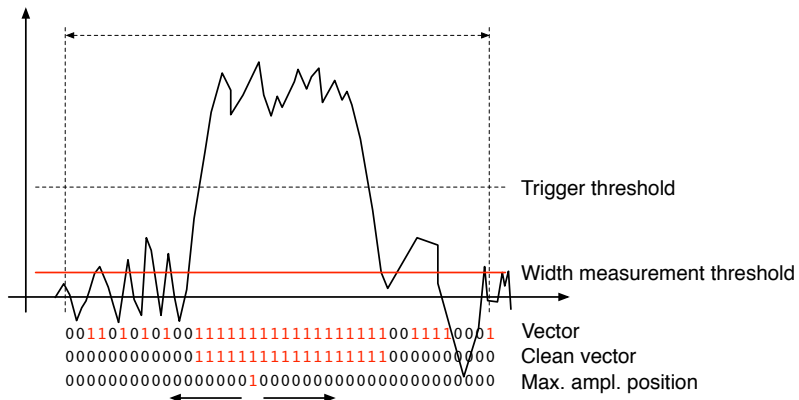


Figure 5.4: A sample pulse. The first vector shows which samples are above the width measurement height. The second vector is a clean vector. The third line shows the position of the maximum amplitude. The vector cleaning algorithm starts from the maximum amplitude and continues in both ways along the vector.

2323 The routine starts from the position of the maximum height. It follows the vector
2324 in both ways and finds the first falling edge (0 at this position and 1 at the previous
2325 one). From there on it rewrites any binary 1 with a binary 0. The resulting clean
2326 vector only has one bunched set of binary ones which are summed, yielding a precise
2327 pulse width. The area measurement is similar - it only integrates over the samples
2328 marked in the clean vector. Both measurement routines, for area and for width, are
2329 implemented separately so that the area routine can have a different threshold set.

2330 This section explains how the algorithm is designed. First, the idea for it was

5.6. DESCRIPTION OF THE FIRMWARE

2331 tested using Excel and was only afterwards ported to the VHDL. The underlying
 2332 algorithm first cleans the vector. Then it passes the cleaned vector either to the width
 2333 or area measurement (see figures 5.5a, 5.5b, 5.6a and 5.6b). The width measurement
 2334 module only sums the ones in the vector whereas the area measurement module sums
 2335 the data samples marked by the cleaned vector. Both modules issue a *valid* signal
 2336 when they finish the measurement.

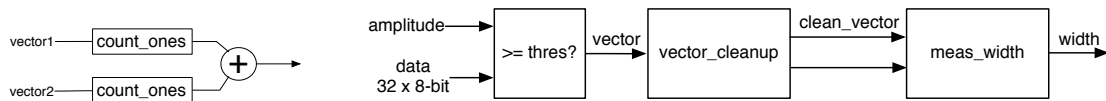


Figure 5.5: This block counts the remaining binary ones in the clean vectors and outputs this value as the pulse width.

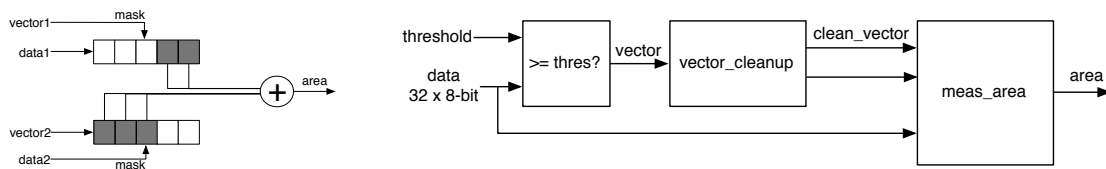


Figure 5.6: This block masks the input data with the clean vector and sums the remaining samples.

2337 5.6.3.1 Vector cleaning

2338 This is the most important block. Its inputs are: *vector*, *parsing active*, *position of the*
 2339 *max. amplitude (PA) and its delay (DA)*. PA is a 32-bit binary number that shows the
 2340 position of the sample with the maximum amplitude within the data block whereas
 2341 the DA tells us how many clock cycles after the start of the parsing this PA block
 is. The vector cleaning module is designed as a final state machine (FSM) with the

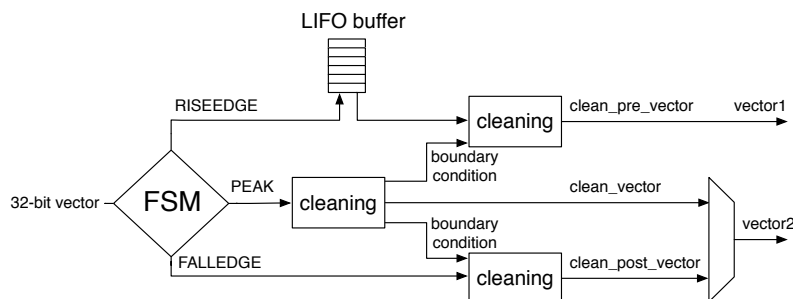


Figure 5.7: Vector cleaning routine outputs two vectors - one forward in time and one back in time from the peak of the pulse.

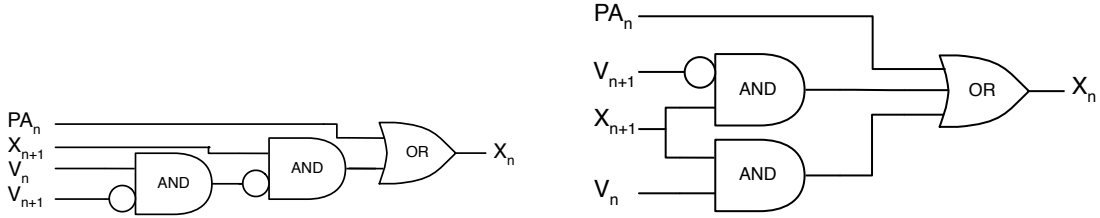


Figure 5.8: One logic step in the algorithm chain before and after Karnaugh minimisation.

2343 states IDLE, RISEEDGE, PEAK, FALLEDGE and READY. The FSM is idle until it
 2344 receives the *active* signal from the external module, marking that the vector parsing
 2345 has commenced. It switches to RISEEDGE, which starts two procedures: 1) it fills
 2346 the vector of the pulse's rising edge into a last-in-first-out (LIFO) buffer and 2) counts
 2347 down from the DA value. When this counter reaches 0, the FSM changes its state to
 2348 PEAK because the current vector on the input is the one containing the maximum
 2349 amplitude. This data block is sent through the *peak algorithm*, which cleans the
 2350 vector. The FSM switches to FALLEDGE state. Now both the previously buffered
 2351 vector of the rising edge and current vector of the falling edge go through the *pre-*
 2352 *and post- algorithm* where they are cleaned, but they get their boundary conditions
 2353 from the *peak algorithm*. The output of this module is therefore two cleaned vectors
 2354 in parallel – one forward in time and the other backwards.

2355 5.6.3.2 Algorithm

2356 The underlying algorithm is sequential - it carries out a logic operation on vector bit
 2357 0, uses the output of this operation for the operation on bit 1 and so on. This means
 2358 that it has to carry out 32 logic operations per clock cycle. With each operation taking
 2359 approximately 0.3 ns, the whole logic chain takes approximately 10 ns to complete.
 2360 With only 6.4 ns per clock cycle, this means timing errors would occur. To fix the
 2361 problem, a more complicated *decimated algorithm* was invented. It consists of two
 2362 parallel logic chains which only take every second bit into account and are at the end
 2363 merged together. This effectively reduces the number of sequential logic operations
 2364 to around 18, which is within the timing constraints.

2365 5.7 Control and data interface

2366 Communication between the device and the controller PC is done via the API func-
 2367 tions provided by the producer. In addition, the API used by CIVIDEC has access
 2368 to several extra functions. These allow the user to download a customised bitfile to
 2369 the FPGA, access the I/O registers and use the USB data transfer.

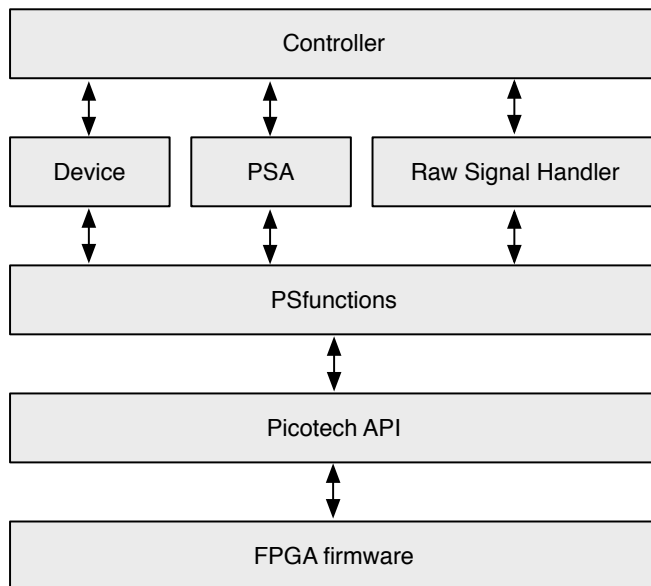


Figure 5.9: Abstraction levels of the controller software

2370 5.7.1 Software

2371 The software has been designed in C++ in several levels of abstraction. Figure 5.9
 2372 shows the structure of the classes. The classes Device, PSA and RawSignalHandler
 2373 are there to make it easier to read and understand the controller code. In principle the
 2374 PSfunctions can also be accessed directly by the controller, but for this the instruction
 2375 sequences must be well known and understood.

2376 5.7.2 Data readout

2377 The device records the data in two forms - as signal waveforms and as histograms
 2378 of analysed pulse parameters. Both are available upon request from the controller.
 2379 Only one of the two can be transferred via the USB line at a time.

2380 The waveforms are saved into a FIFO buffer, which can hold up to 64 pulses of the
 2381 length of \sim 500 samples. The data format for each pulse is such that it starts with a
 2382 header containing the pulse timestamp and the sequential number, continues with the
 2383 data samples and ends with a header containing all the measured parameters (width,
 2384 amplitude, area, falling slope and form factor). When the FIFO is full, it issues a
 2385 flag, which tells the controller that the data buffer is ready for readout.

2386 The histograms are implemented into the FPGA's Block RAM. Their size ranges
 2387 from 256 to 4096 bins (an 8-bit or a 12-bit histogram, respectively), depending on the
 2388 required histogram resolution. For instance, the width parameter is measured with a
 2389 0.2 ns resolution; the expected maximum pulse width is less than 20 ns. This yields
 2390 the maximum range of 100 bins, making an 8-bit histogram sufficiently large. The
 2391 same reasoning is applied to the amplitude measurement. In this case the maximum

*CHAPTER 5. CURRENT MONITORING
REAL-TIME PARTICLE IDENTIFICATION*

range is defined by the 8-bit resolution of the ADC. The area measurement, however, yields higher values and can therefore have a more refined binning (12-bit). Finally, a single 12-bit 2D histogram is included, with 6 bits for every axis. It is used as an online scatter plot for comparing one measured parameter to another. An example for it is a comparison of the width against the area, which can help the user determine the cuts that need to be applied to the measurement.

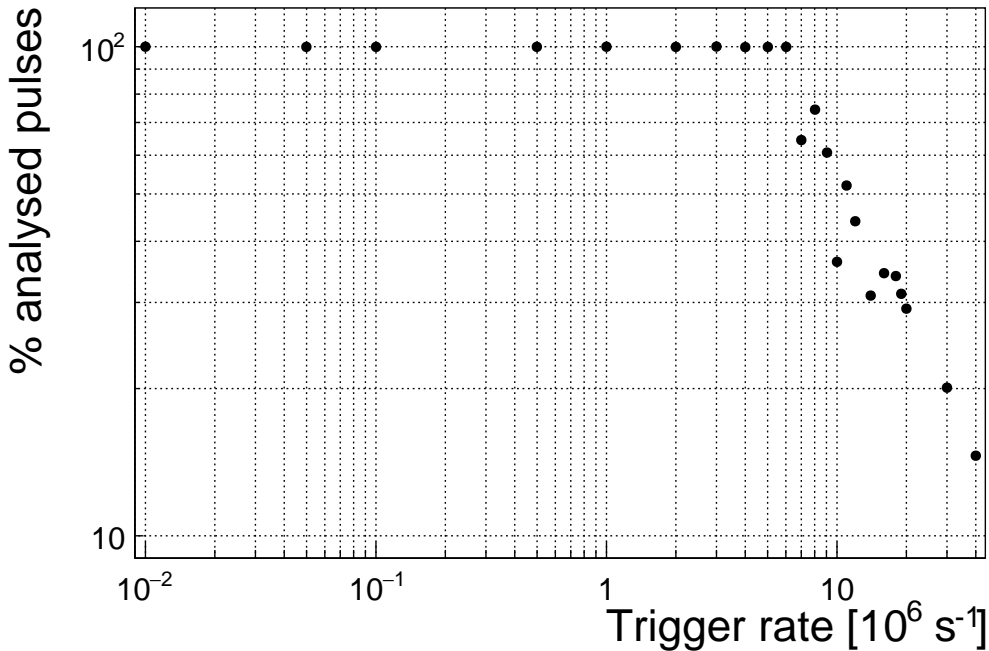


Figure 5.10: This figure shows the capability of the device to analyse all arriving pulses for a range of input frequencies. The highest achievable rate with zero lost pulses is $5 \times 10^6 \text{ s}^{-1}$.

2398 5.8 Performance results

2399 The device has been tested in the lab using a pulse generator as well as several radioac-
2400 tive sources. The results show that: 1) the amplitude, area and width measurement
2401 are linear across all input ranges, 2) the highest rate of the PSA algorithm is $\sim 5 \times 10^6$
2402 pulses per second and 3) the lowest SNR where the algorithm still functions is ~ 5 .

2403 **Trigger rate** A pulse generator was used to verify the highest achievable rate at
2404 which the PSA still analyses every incoming pulse. The final state machine imple-
2405 mented in the pulse analysis module prevents the triggering block from issuing a
2406 trigger due to an incoming pulse if the previous analysis is still in ongoing. Given
2407 that all the pulses were of the same length, the analysis duration was always the
2408 same. When the time between the incoming pulses was shorter than the time of the
2409 analysis, the pulses were not analysed. Figure 5.10 shows the sharp decline in the
2410 percentage of the analysed pulses when reaching the rate of 5 MHz. Therefore the
2411 overall analysis duration for a 10 ns pulse is approximately 200 ns.

2412 **Linearity** A pulse generator was used to verify the linearity of the measurements
2413 across all input ranges. Pulse width and amplitude were varied and measured both
2414 with the oscilloscope and the PSA to check for non-linearities or inconsistencies in the
2415 PSA measurements. The resulting plots in figures ?? and 5.11c show that the PSA
2416 measurements agree well with those from the oscilloscope. The major inconsistency

is observed in the lower range of the plots. It stems from the fact that the bandwidth limit of the PSA is lower than that of the oscilloscope, which affects the pulse shape. Effectively, the PSA cannot measure the rectangular pulses of the width smaller than 2 ns.

Stability The input pulse signal was superimposed with white noise generated by a noise generator with a variable gain. The mixed signal yielded pulses with an SNR ranging from 5 (very noisy) to 100 (noise negligible). The PSA then performed the pulse parametrisation at different SNRs. The resulting plots in figures 5.11b, 5.11d and 5.11e show that the pulse width measurement is stable even for low SNR whereas the amplitude measurement is affected significantly. This stems from the analysis taking the highest sample as the pulse's amplitude. The area measurement, being effectively the integrated amplitude across the pulse, is also affected by the faulty amplitude measurement. Nevertheless, the mean area remained the same. This means that the added noise only affects the resolution of the spectrum, not its position.

5.8.1 Comparison between the charge- and current-sensitive spectroscopy

The calibration was done using a $^{148}\text{Gd}^{239}\text{Pu}^{241}\text{Am}^{244}\text{Cm}$ source which emits α particles with four different energies. The PSA in combination with the current amplifier was compared against the 8-bit spectroscopic application in combination with the charge amplifier and a commercial 14-bit spectroscopic readout.

The ^{241}Am peak measured by the Cx amplifier has an RMS of 0.8 ADC, which corresponds to a 32 keV energy resolution. For comparison, the C2 amplifier measures this peak with an RMS of 1.9 ADC, which corresponds to a 75 keV energy resolution. Therefore the energy spectrum measured by the current amplifier has a lower energy resolution.

5.9 Source calibration

The operation of the pulse shape analysis was tested using several radioactive sources. In particular, an α , a β , a γ and a n source were used. Each source was placed on top of the diamond detector and left for a predefined time depending on its activity. Table 5.2 shows the sources used, the time of exposure and their rate during this time. The data for the α source were taken for both polarities. In addition, a long run with an α source with a sheet of paper in between the source and the diamond was taken. The paper stopped the α particles but let through the photons, which helped to estimate the background photon radiation of the source.

5.9. SOURCE CALIBRATION

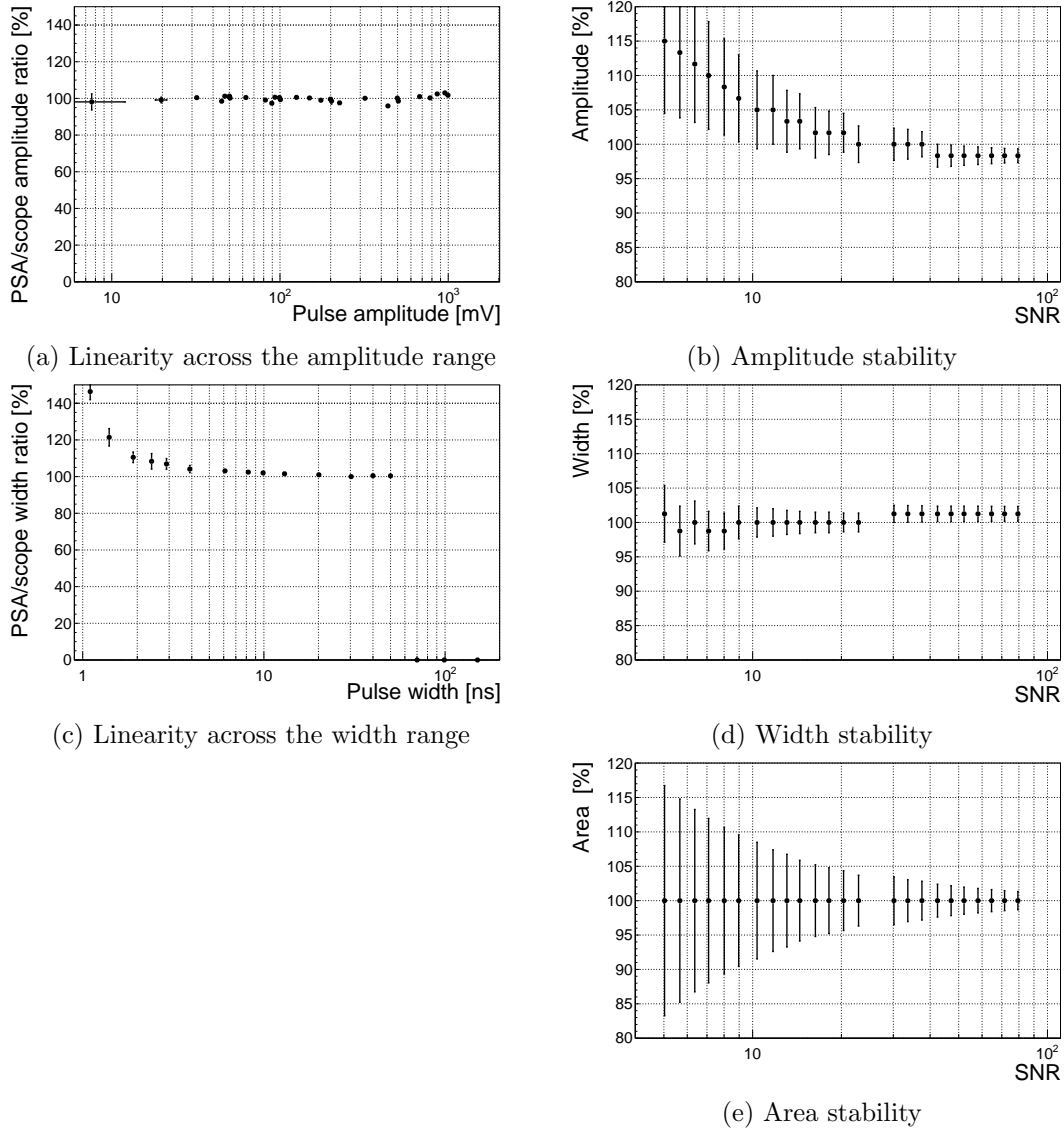


Figure 5.11: These diagrams show the linearity of the measurements and their stability with respect to analog noise.

Run	Source	Radiation	Energy [MeV]	Time [h]	Triggers	Rate [s^{-1}]	Bias [V]
2452	1 $^{241}\text{Am}^*$	α	5.5	60	958	4.4e-3	500
	2 ^{241}Am	α	5.5	17	10558	0.17	500
	3 ^{241}Am	α	5.5	18	11454	0.18	-500
	4 ^{90}Sr	β	2.3	0.42	1.07e6	1000	500
	5 ^{60}Co	γ	1.3	0.28	1.34e6	3300	500
	6 $^{239}\text{Pu Be}$	n	1–10	2.5	1.5e6	230	500

Table 5.2: Measurements carried out at Atominstitut

2454 The pulses acquired during the data taking are shown in persistence plots in
 2455 figures 5.13. Figure 5.13a showing the ^{241}Am source background reveals that the
 2456 diamond detector had been contaminated. This stems from the fact that α pulses

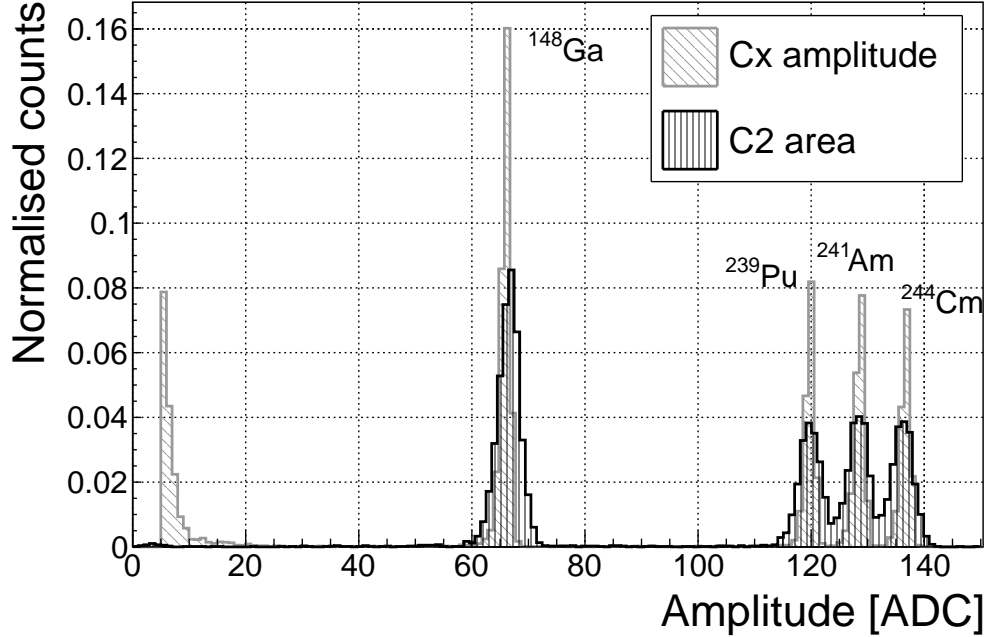


Figure 5.12: Spectrum of a $^{148}\text{Gd}^{239}\text{Pu}^{241}\text{Am}^{244}\text{Cm}$ source using a Cx and a C2 amplifier

are recorded despite having a sheet of paper, which stops all the particles emitted by the source. However, the number of α hits due to contamination is negligible - an estimated 1 h^{-1} . Another point worth noting is the falling slope of the rectangular pulse in figure 5.13c. This stems from the space charge that had built up during the neutron irradiation and is discussed in section 5.9.3. Finally, figure 5.13f shows that the neutron source causes the widest variety of pulse shapes - triangular and rectangular as well as those in between. Pulse shapes caused by neutrons are described in detail in [44, 43].

5.9. SOURCE CALIBRATION

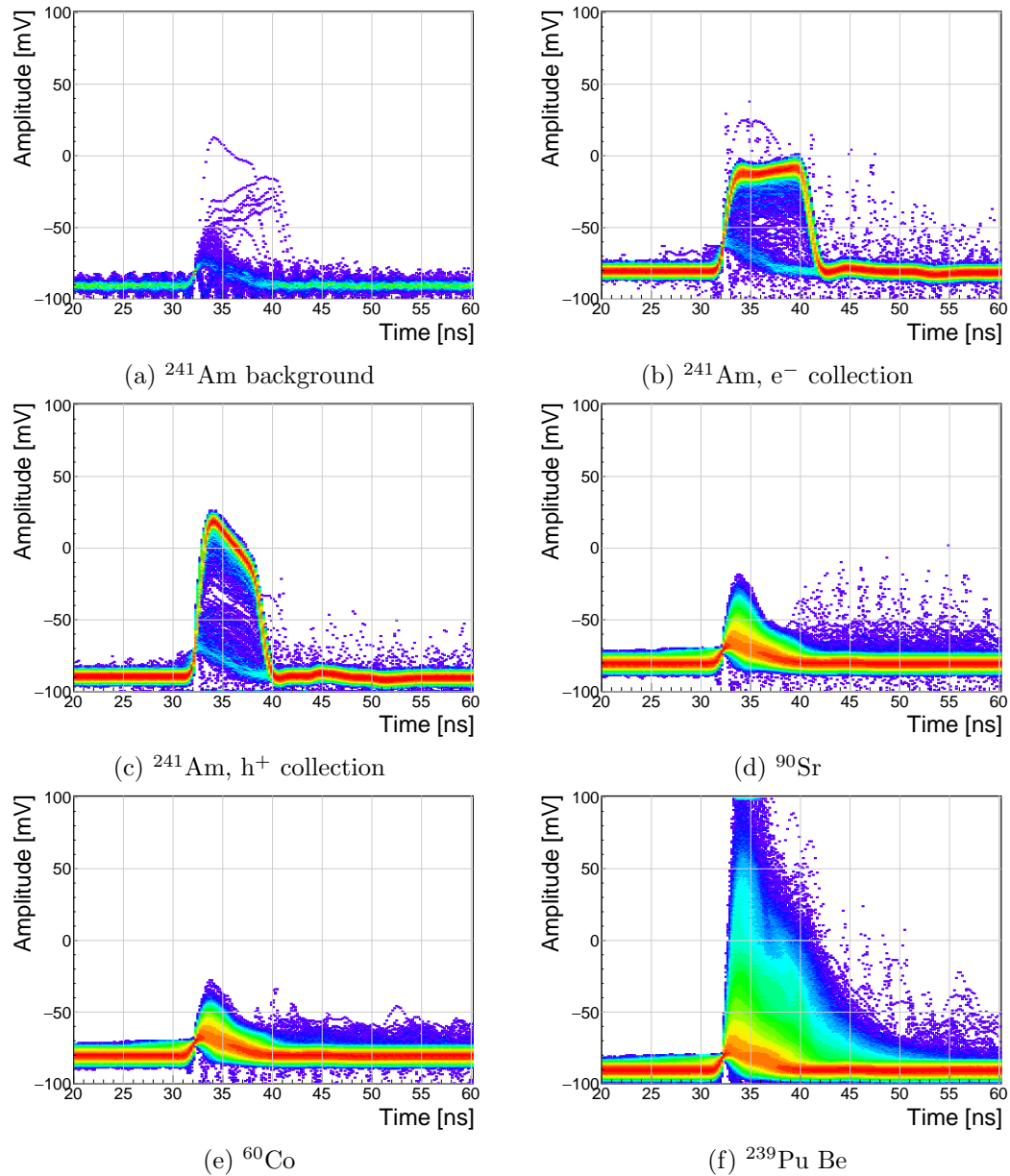


Figure 5.13: Accumulated pulses for all runs

2465 5.9.1 Source measurements - scatter plots

2466 An online pulse shape analysis has been run on all the above mentioned data sets.
2467 The parameters of the pulses are plotted in 2D histograms - in form of scatter plots.
2468 The aim is to find a way to distinguish between the various types of radiation in
2469 order to only select the spectrum of a single type of particles from a spectrum of a
2470 mixed source. The energy spectrum is directly proportional to the measured area of
2471 the current pulses, therefore all the parameters were plotted against the pulse area.
2472 The parameters used are:

- 2473** • FWHM
2474 • Base width
2475 • Amplitude
2476 • Amplitude × Base width
2477 • Base width - FWHM
2478 • Slope

2479 The sets of plots in figures 5.14, 5.15, 5.16, 5.17 and 5.18 show the above listed
2480 parameters plotted against the pulse area for ^{241}Am background, electrons and holes,
2481 ^{90}Sr and ^{64}Co source, respectively. Any distinguishable difference between the plots
2482 of two sources would suggest that that particular parameter can be used to distinguish
2483 one type radiation from the other. In these figures the photons are considered the
2484 rejected pulses (greyscale colour palette) whereas α particles or neutrons are accepted
2485 (yellow colour palette).

5.9. SOURCE CALIBRATION

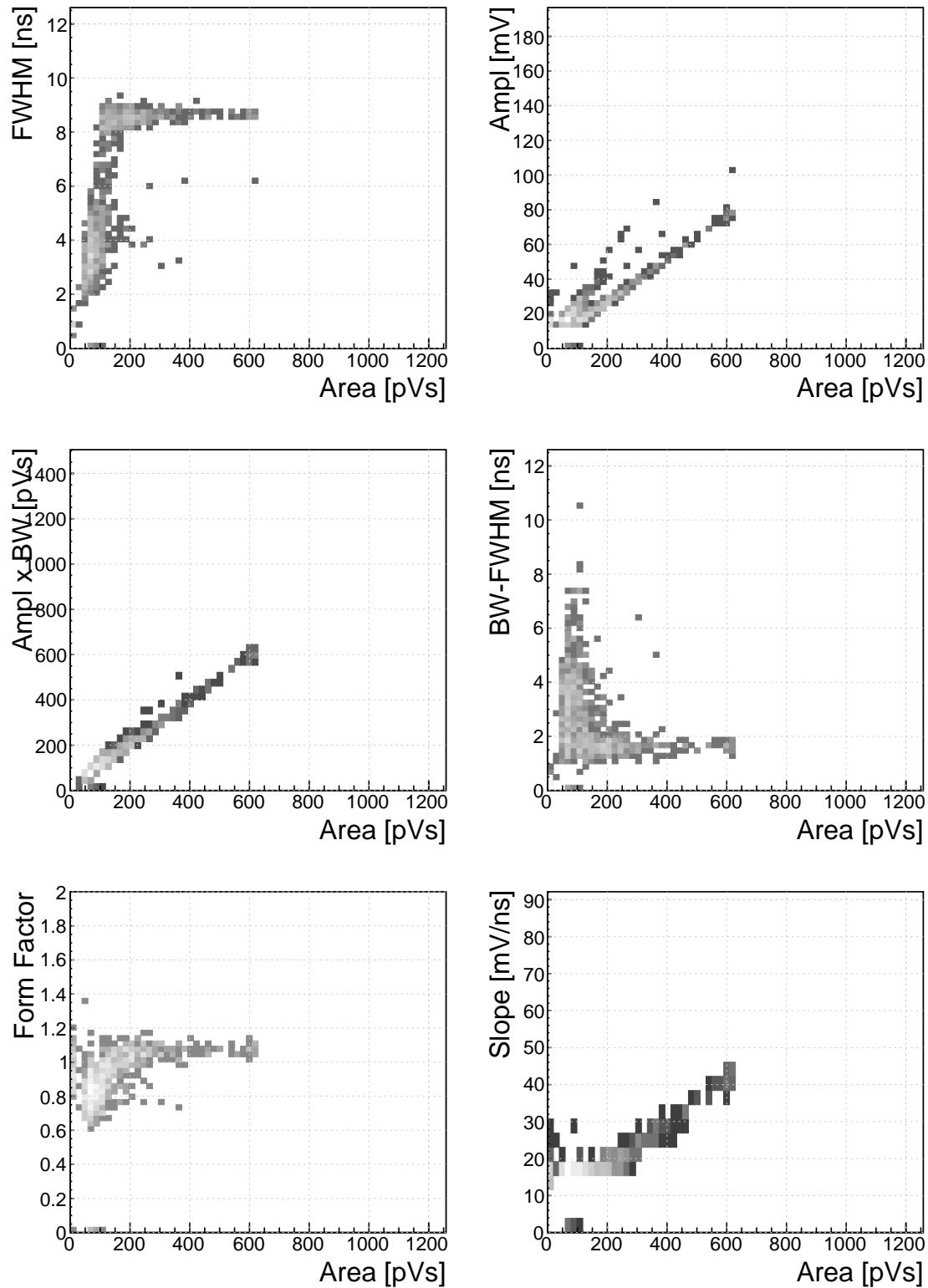


Figure 5.14: Background measurements

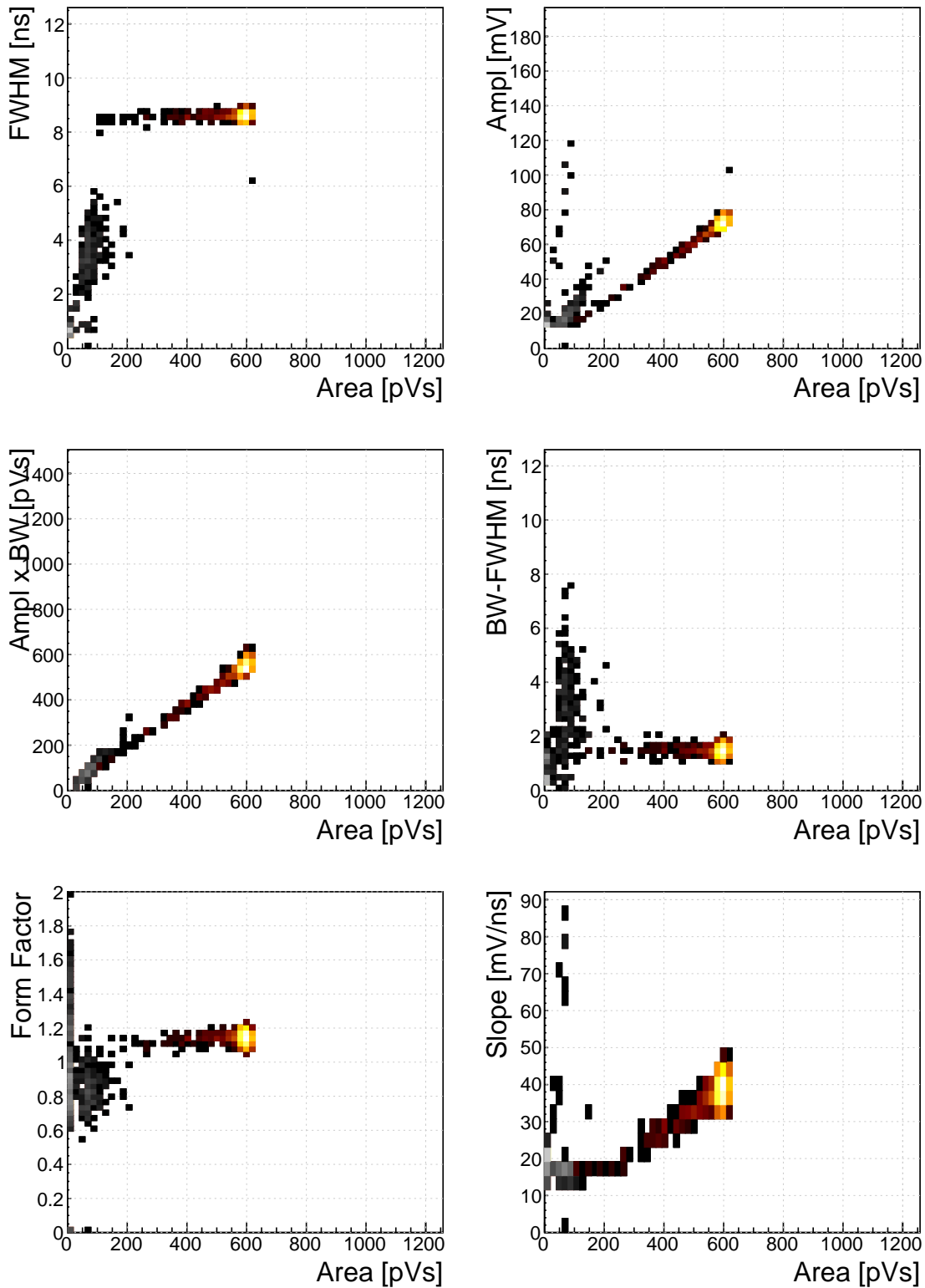


Figure 5.15: ^{241}Am , e^- collection. Qualifier: FWHM 7–10 ns.

5.9. SOURCE CALIBRATION

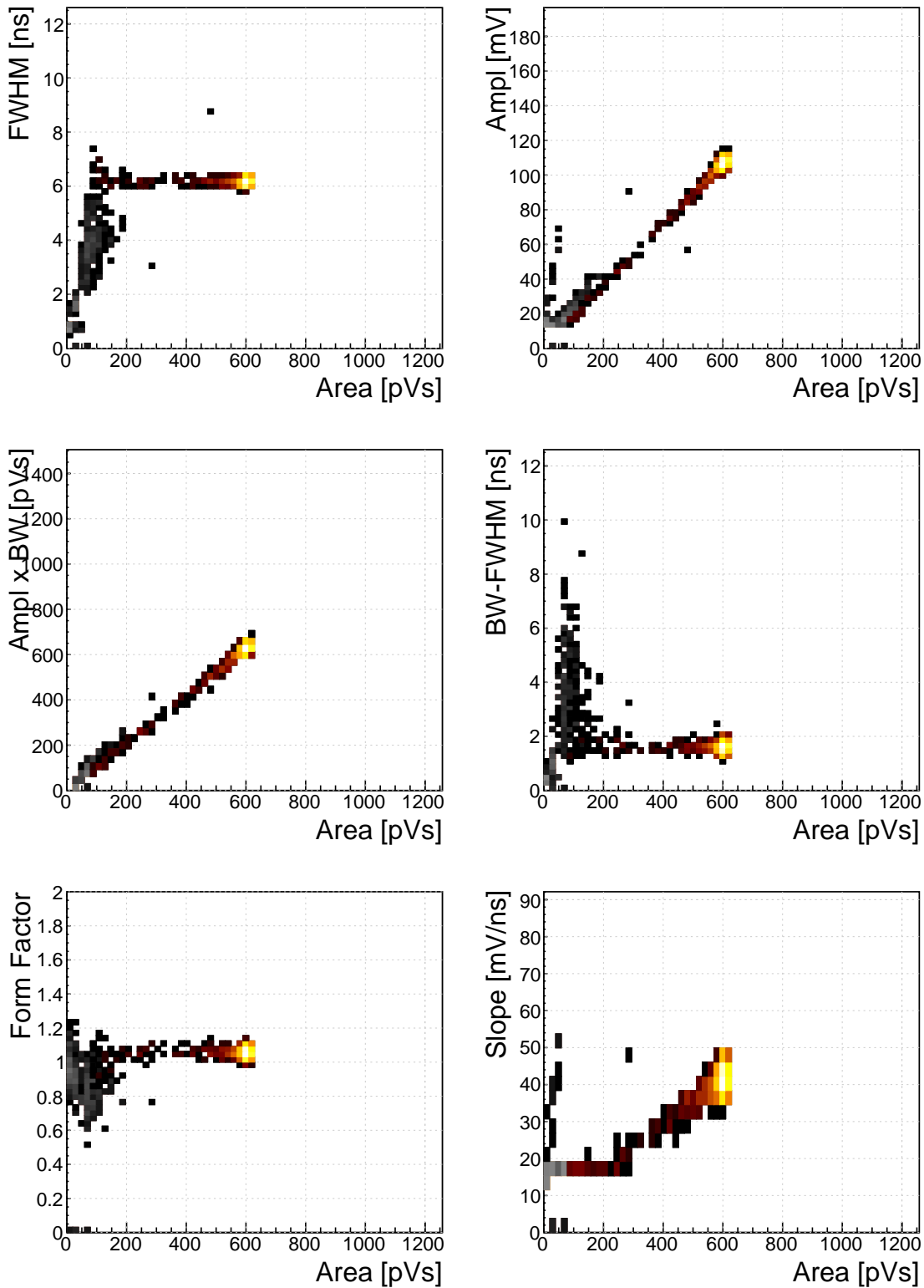


Figure 5.16: ^{241}Am , h^+ collection. Qualifier: FWHM 5.5–8 ns.

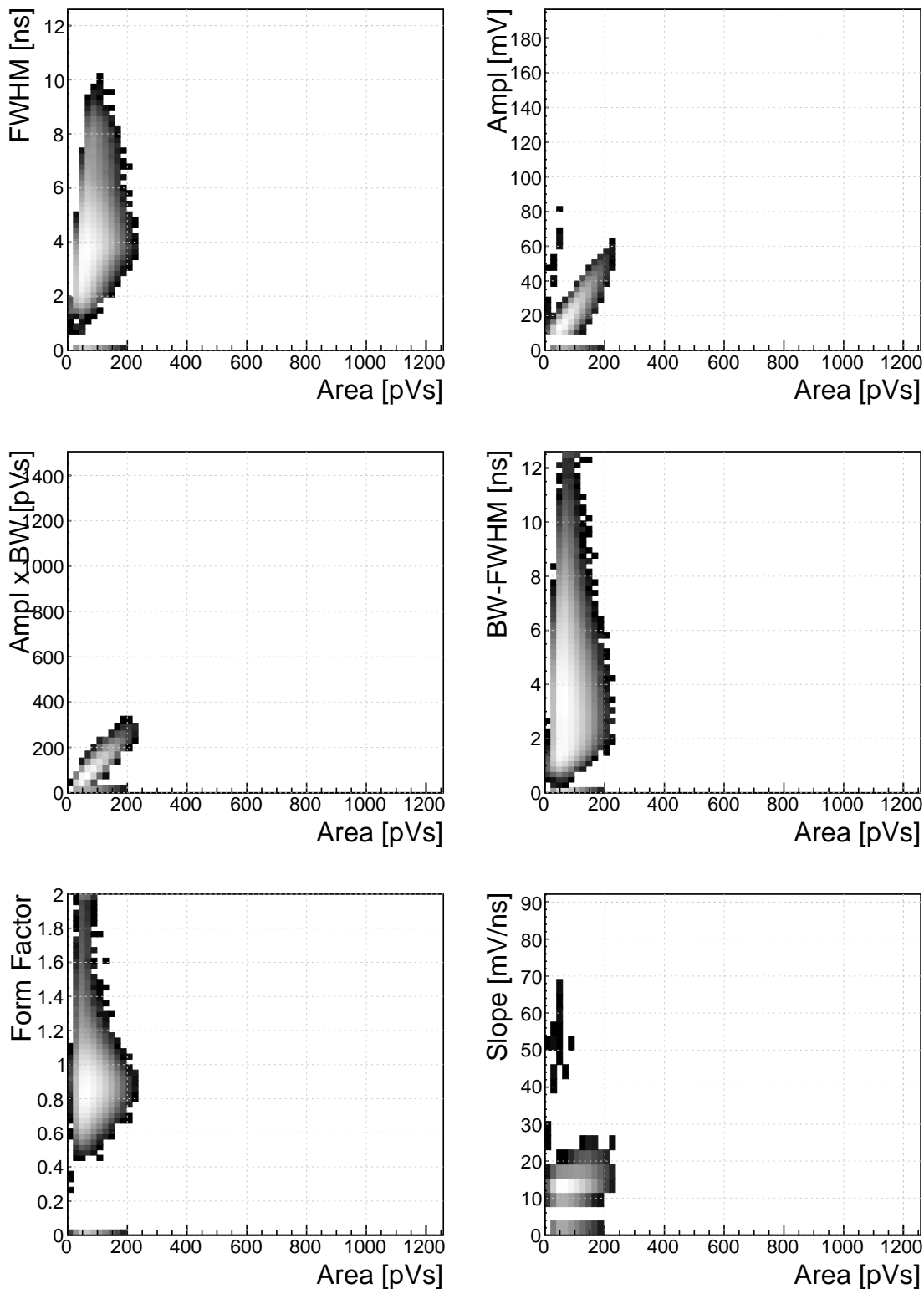


Figure 5.17: ^{90}Sr

5.9. SOURCE CALIBRATION

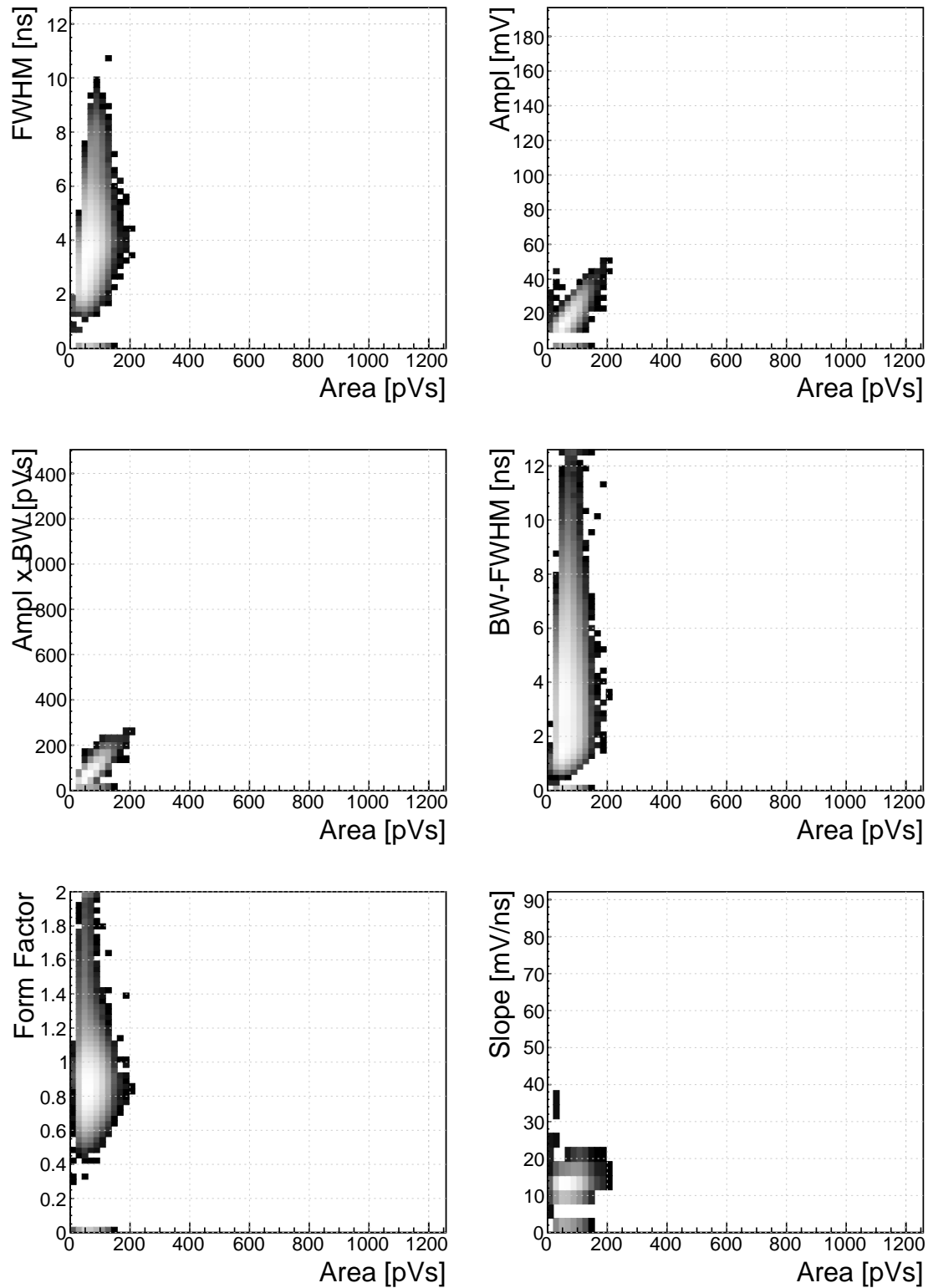


Figure 5.18: ^{60}Co

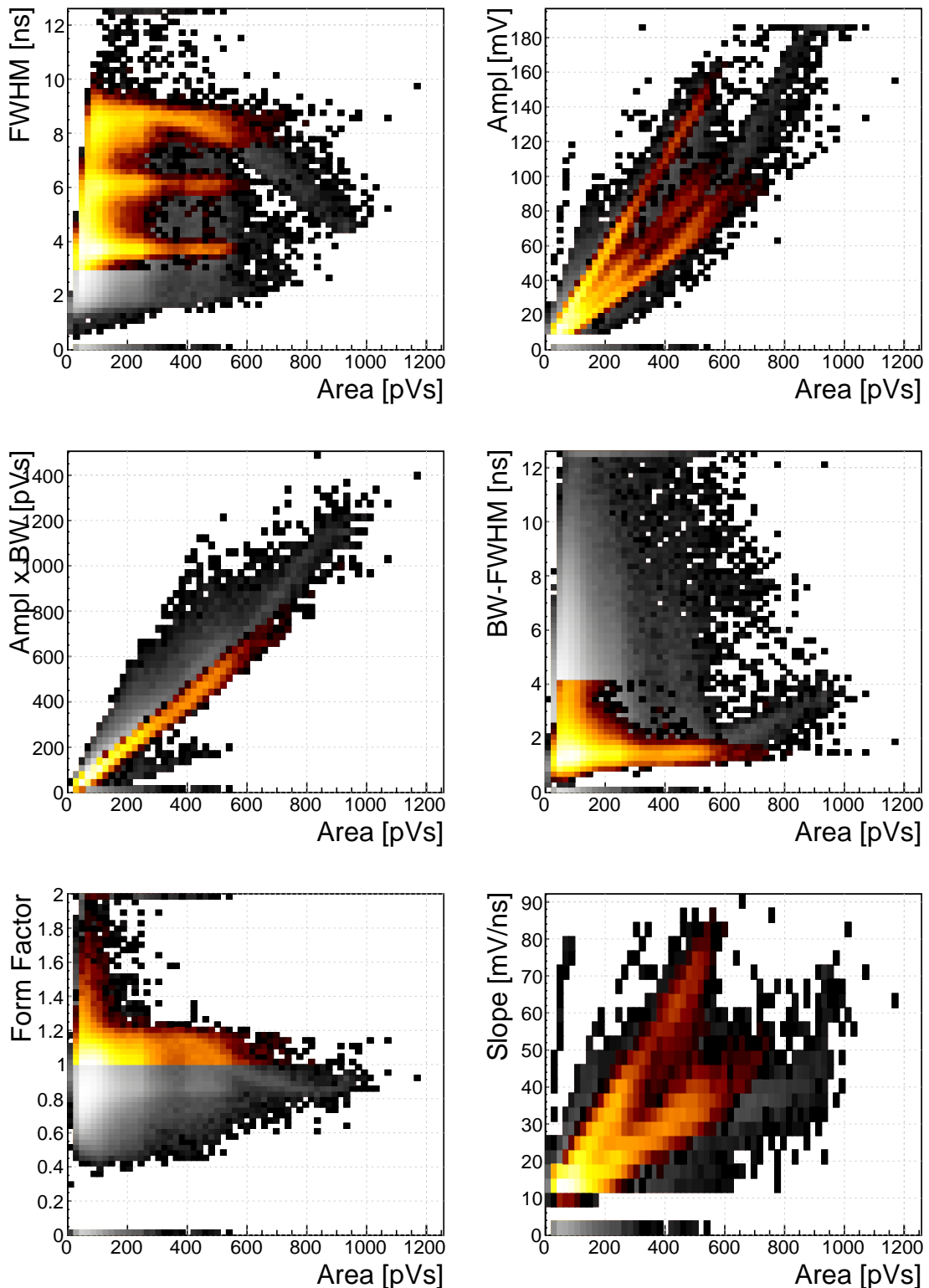


Figure 5.19: ^{239}Pu Be. Qualifiers: BW-FWHM 0.2–4 ns, FWHM 3–12 ns, Form factor 1.45

5.9. SOURCE CALIBRATION

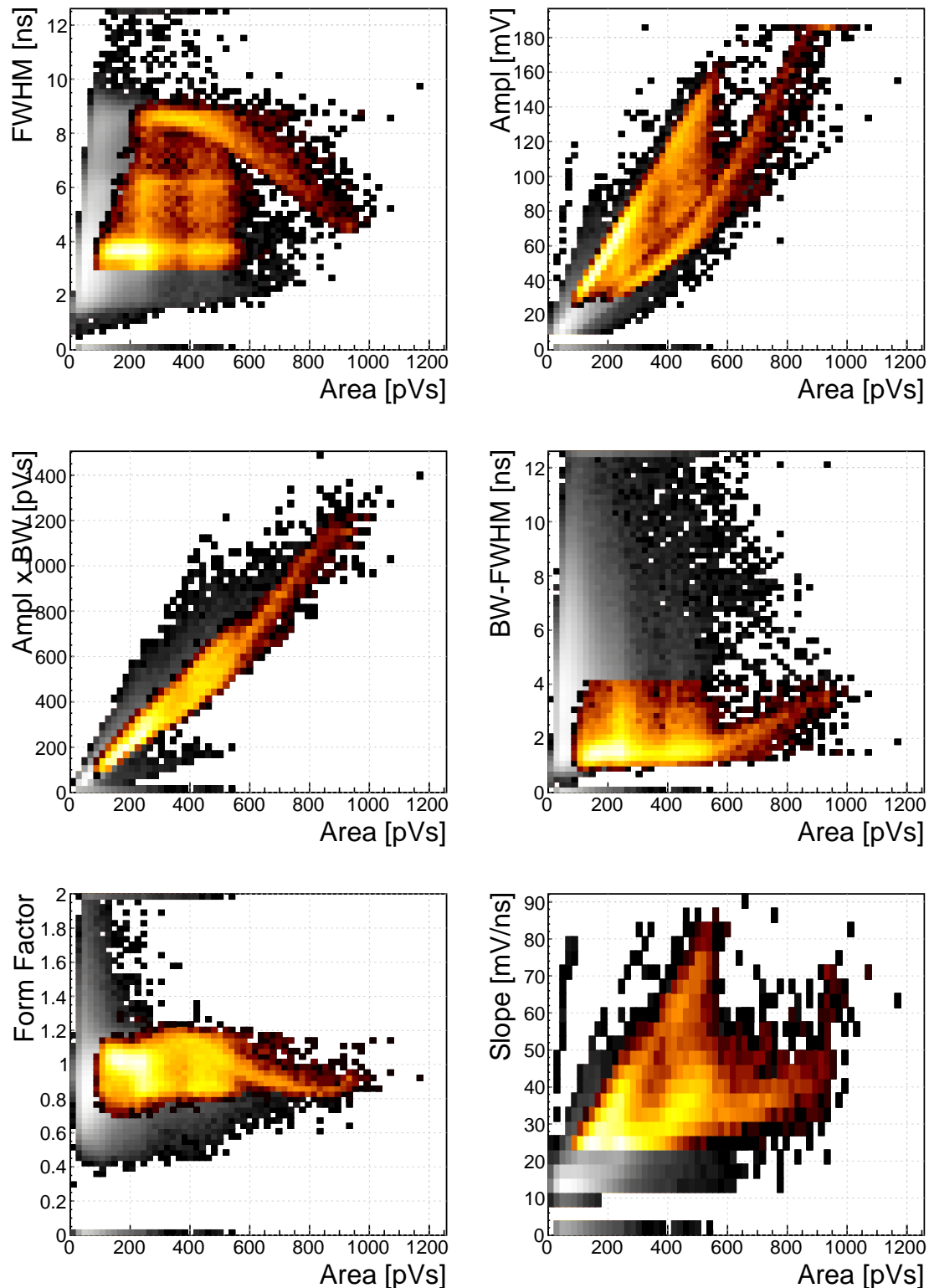


Figure 5.20: ^{239}Pu Be. Qualifiers: BW-FWHM 0.2–4 ns, FWHM 3–12 ns, Slope 25–104 mV/ns

2486 **5.9.2 Discussion**

2487 The ^{241}Am background measurement (see figure 5.14) revealed that the diamond de-
2488 tector has been contaminated, probably with chipped-off grains of the source. These
2489 emit α particles, which are detected by the diamond detector. The resulting plots are
2490 almost identical to those taken during the ^{241}Am run (figure 5.15), with a difference
2491 that there are much fewer α entries in the former. Due to the losses in the air they
2492 vary in energy – from ~ 5 MeV down to 1 MeV. Therefore in the top left plot a dis-
2493 tinctive horizontal stripe appears at a width of 9 ns, ranging from 100 up to 630 pVs.
2494 The shape of the pulse at smaller energies retains the width, only its amplitude is
2495 decreased. The other cluster in the FWHM–area phase space comes from the back-
2496 ground photons. The two clusters are far apart from one another with no overlap. It
2497 is therefore straightforward to define a cut in the FWHM to distinguish between the α
2498 and γ entries. The situation is similar when inverting the bias voltage and collecting
2499 holes (see figure 5.16), but here the two clusters are much closer together, making it
2500 more difficult to define a clear border between the two. The other five qualifiers are
2501 in this case less important than the FWHM. Nevertheless, it can be deduced from the
2502 plots that the difference BW-FWHM must be below 4 ns and that the Form Factor
2503 (bottom left plots) has to be set to 1.45 to push the α entries over 1, which is the
2504 threshold for accepting entries. The slope is dependent of the amplitude, which can
2505 be seen in the bottom right plot, making it an unreliable qualifier in the lower area
2506 range. The amplitude, scaling with area, makes a distinguishable straight line in the
2507 bottom right plot. For the electron collection this line has a different slope coefficient
2508 than the photon related line. For the holes, however, these two lines are overlapping,
2509 rendering it impossible to use this as a means of identifying the α from a γ entry.

2510 The phase space of the ^{90}Sr source overlaps entirely with that of the ^{60}Co source
2511 (see figures 5.17 and 5.18). This renders it virtually impossible to distinguish between
2512 photons and electrons (MIPs). Comparing the FWHM phase space of the photons
2513 and alphas and the high reach of the former, the electron collection of the alphas
2514 would need to be used to distinguish between the two types of particles.

2515 The neutron source emits a mixed field of neutrons and photons. The neutrons are
2516 rarely detected – the interactions happen mostly in the electrodes on either side of the
2517 detector. The α particles created by the interactions are detected by the diamond.
2518 Depending on the side of the interaction, the created pulse is either due to hole- or
2519 electron collection. They make the two distinct lines in the FWHM phase space (see
2520 figure 5.19, top left plot) at 9 ns and 6 ns. The third line at 4 ns is created when
2521 a neutron interacts in the ballistic centre [?] of the diamond – the position where it
2522 takes the holes and the electrons the same time to drift to the opposite electrodes.
2523 The entries in between are created by neutron interactions at random positions in the
2524 diamond, which produce pulses of various shapes. By making use of the Form Factor
2525 set to 1.45, the three-line structure becomes more pronounced. However, a part of the
2526 cluster belonging to the 9 ns line is omitted. This part with the area ranging between
2527 600 and 1000 pVs starts decreasing in FWHM due to an unexplained phenomenon,
2528 probably detector related. Consequently its Form Factor falls below the threshold

5.9. SOURCE CALIBRATION

of 1, rejecting these entries as background. In an alternative case (see figure 5.20), a Slope qualifier is used instead. By cutting the pulses whose falling slope is not steep enough, there is a big chance that neutrons with a low energy deposition (small amplitudes) are cut away as well. Nevertheless, the entries with the large area, which definitely pertain to the neutron interactions, are accepted in this case. The three distinct lines in the FWHM phase space are still visible.

5.9.3 Space charge build-up

Space charge built up during the neutron irradiation ($\sim 10^{10}$ n), which reflected on the pulse shapes. Instead of a flat top, they developed a slope. This was of opposite signs for the two polarities, as can be seen in figures 5.21a and 5.21b. The figures contain a set of 64 superimposed pulses taken at ± 500 V bias. The shape persisted until the space charge was neutralised by means of a β source irradiation at a 0 V bias. Figure 5.22 shows the decreasing of the slope coefficient as a function of received β dose.

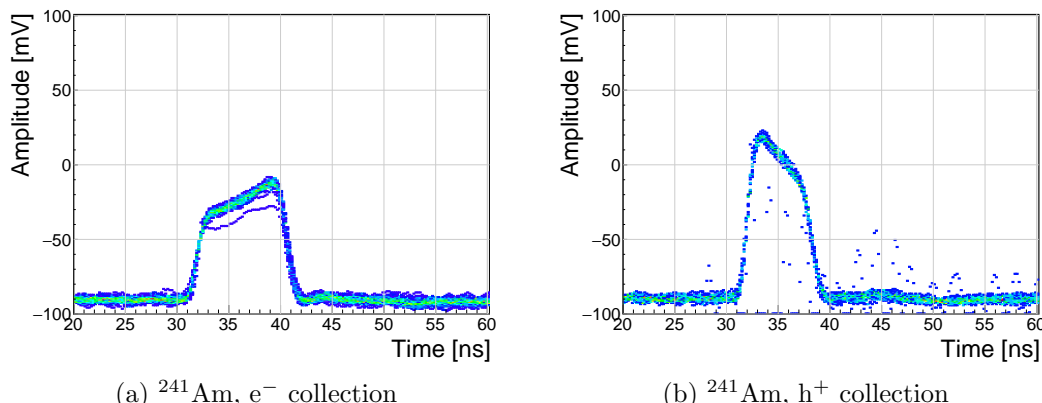


Figure 5.21: Built up space charge causes a slope which has the opposite slope for electrons and holes

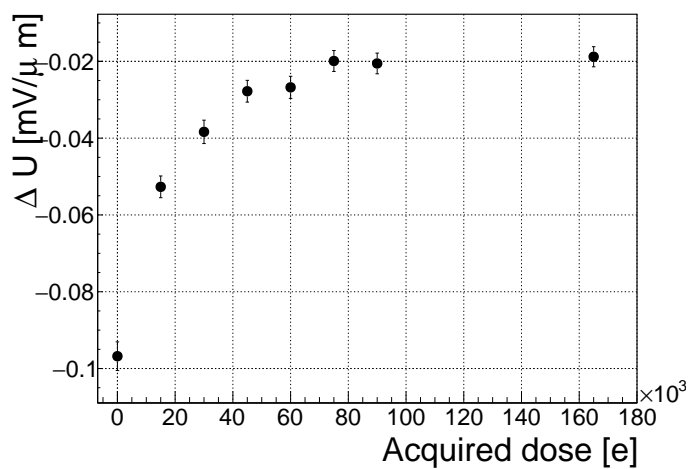


Figure 5.22: Using β radiation to reduce space charge in diamond

5.10 Applications in neutron instrumentation

The real-time pulse shape analysis procedure can be applied to more complex systems. This section includes three applications where the PSA has been applied.

Semiconductor-based neutron detectors provide a compact technology for neutron detection. However, the cross section of a neutron with the diamond bulk is very low, since it only interacts with the core of the atom. Diamond is mainly used to detect charged particles and photons.

Research neutron reactors radiate a mix of particles, apart from neutrons also photons. The photons are considered a background radiation, concealing the neutron spectrum. When measured with diamond, the signal from neutrons is difficult to distinguish from the photon spectrum. In addition, low energy neutrons do not cause nuclear reactions in the bulk. All in all, the neutron measurements in a reactor present a challenge with diamond. However, by means of the PSA, the neutron signal can be discriminated from the photon background to some extent. The following two cases show how measurements of fast (n^+) and thermal (n^-) neutrons have been carried out by making use of the PSA.

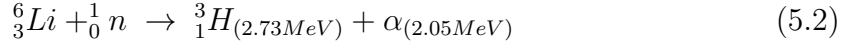
Note the changing scale on the X axis in the figures.

5.10.1 Thermal neutron flux monitoring

Research neutron reactors like TRIGA MARK II [?] at Atominstitut [?] in Vienna are capable of emitting neutrons at a wide range of energies. The neutron flux is proportional to the current power of the reactor. It is therefore instrumental to monitor the neutron flux to make sure that the reactor operation is within the specified limits. However, the byproduct of the radioactive decays in the core is γ radiation, which has an energy range that overlaps with that of neutrons, making it difficult to measure the neutron flux. This is where PSA and diamond detectors come into play. This section describes the application of thermal neutron flux monitoring by means of the PSA.

Thermal neutrons do not interact with the diamond bulk due to their low kinetic energy (of the order of 0.012 eV). Hence a converter foil has to be added to produce second order effects. Incoming neutrons interact with the foil, producing a set of secondary particles. These can then be detected upon hitting the detector bulk. Common neutron interactions that are used in thermal neutron detection are $^{10}\text{B}(n,\alpha)^7\text{Li}$ reaction and $^6\text{Li}(n,\alpha)^3\text{H}$ reaction (α stands for ^4_2He , see equation 5.2). The focus in this section is on the latter. With a foil installed, there are several possibilities for neutrons to interact with the detector system. Each of these interactions ionises the diamond bulk in its own way, resulting in a specific shape of the current pulse. A neutron can: 1) interact with the foil, producing an α and a ^3H , 2) interact with a carbon atom in the lattice, producing an α and a γ or even three α . The thermal neutrons do not have enough kinetic energy to interact with the lattice,

2582 therefore the focus will be on case (1), the equation for this reaction is the following:



2583 The particles in the first case are produced outside the diamond and get stopped
2584 immediately upon hitting the sensor. The resulting pulses for both particles have a
2585 rectangular shape of the same width, because the carriers drift with the same speed
2586 in both cases. The difference is in the number of free carriers produced - the tritium
2587 creates more (proportional to the deposited energy), which in turn induces a higher
2588 pulse.

2589 TRIGA MARK II neutron reactor emits large amounts of γ radiation in the
2590 energy range up to 3 MeV. This already affects the measurements of α particles, the
2591 energy of which peaks at 2.05 MeV in the case of 6Li converter foil. However, γ
2592 background radiation can be suppressed by discriminating current pulses of photons
2593 from those induced by α particles. This idea has already been implemented in offline
2594 analysis in [29, 24]. The results show that the background photons can be subtracted
2595 successfully. In order to make sure that every single incident thermal neutron has
2596 been accounted for, the algorithm has been ported to FPGA where it detects and
2597 analyses particles in real time.

2598 5.10.1.1 Measurements

2599 ROSY readout device with the implemented Pulse Shape Analysis was put to a test
2600 at Atominstut in Vienna. Their TRIGA2 neutron reactor is capable of delivering
2601 thermal neutrons with the energy 0.012 eV at a rate of $10^3 n \text{ cm}^{-2} s^{-1}$, with a
2602 considerable γ background.

2603 First, the device was calibrated using an unsealed monochromatic ${}^{241}Am$ source
2604 with the emitted particle energy $E_\alpha = 5.12MeV$ (taking into account the losses in
2605 the air). Then the diamond detector was exposed to the beam. Secondary reaction
2606 products (α and 3H particles), created by neutrons hitting the converter foil, were
2607 detected by the diamond sensor, together with a significant photon background. Then
2608 the pulse identification algorithm was applied to discriminate between the reaction
2609 products and the photons.

2610 The main parts of the detector are an sCVD diamond sensor sized $4.7 \times 4.7 \text{ cm}^2$
2611 and a $1.8 \mu\text{m}$ thick LiF converter foil, both embedded in an RF-tight PCB. The
2612 diamond sensor is biased with a bias voltage of $1 \text{ V}/\mu\text{m}$ and capacitively coupled to
2613 CIVIDEC's C2 40 dB wide bandwidth current preamplifier. A 5 m long BNC cable
2614 connects the preamplifier to CIVIDEC ROSY box. The detector assembly together
2615 with the preamplifier has to be placed in front of an exit hole of the reactor.

2616 Note: this data set has been taken with an older version of the firmware, which
2617 only measured a limited number of pulse parameters.

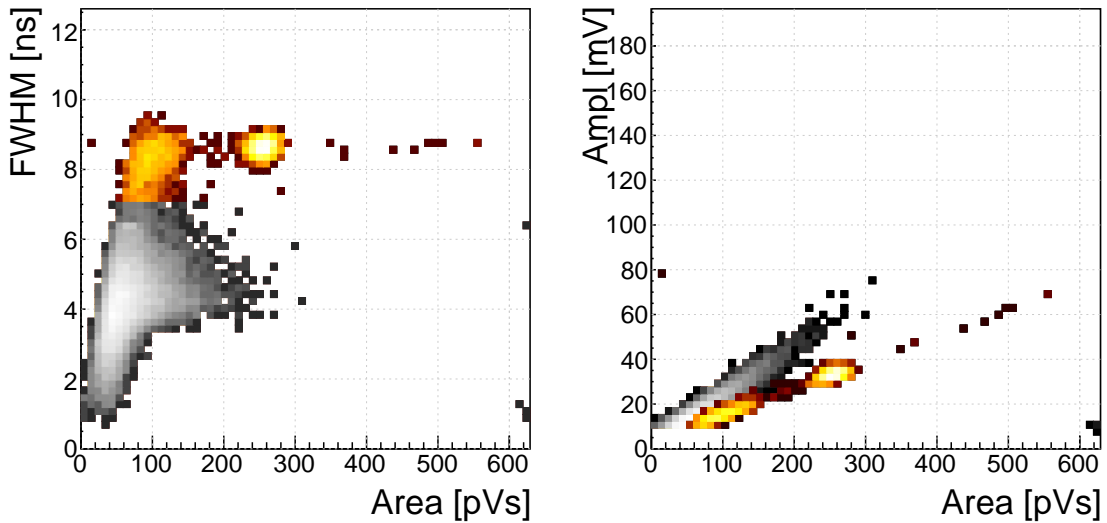


Figure 5.23: Thermal neutrons, photons. Qualifier: FWHM 7–12 ns

5.10.1.2 Results

The data collected by the PSA show a high flux of photons, which covers a wide area range. The ^3He peak is clearly visible and has almost no overlap with the photon cluster. The α cluster has a much lower energy and is in the same energy range as the photons. However, if a FWHM parameter is observed, a distinction between the photons and the α can be seen. By setting a qualifier to the right value, the photon background is cut away, leaving only the thermal neutron decay products in the data set (see figure 5.23).

5.10.2 Fusion power monitoring

Many research collaborations around the world are trying to develop a functional fusion reactor, which could provide a cleaner energy source. One of them is ITER [8], a research fusion reactor being built in France. The idea behind it is to harvest energy from the fusion of light atoms into a heavier one. For ITER the fuel chosen is a mixture of deuterium and tritium, which fuse into a helium atom at extremely high temperatures (plasma), emitting a highly energetic neutron as a byproduct. The equation is the following:

$${}_1^2D + {}_1^3T \rightarrow {}_2^4He + {}_0^1n + 17.6 \text{ MeV.} \quad (5.3)$$

The α particle immediately deposits its energy within the plasma. The neutron, due to its neutral charge, continues its way out of the system where it is stopped. The stopping power is converted into energy, which heats the water into steam, which in turn spins the turbines, generating electricity.

It is possible to monitor the activity of the reactor by measuring the flux of neutrons emitted. Neutron diagnostics such as neutron cameras, neutron spectrometers

and neutron flux monitors therefore provide robust measurements of fusion power. A high γ background makes it difficult to accurately measure the neutron flux. This is a motivation to use a diamond based detector with a real-time PSA algorithm.

The neutrons emitted are 14 MeV mono-energetic fast neutrons. The most accurate and efficient way to detect them with a diamond detector is by means of a $C_{12}(n,\alpha)$ reaction with a carbon atom in the ballistic centre [30]. In this region the positive and negative charge carriers created by α that start drifting in the opposite directions need the same time to reach the opposite electrodes.

5.10.3 Fast neutron monitoring

The CROCUS reactor at EPFL [3] is a research neutron reactor. The research group working on the reactor is interested in measuring neutrons with energies between 1–2 MeV, which is overlapping with the γ background energy range.

The highest output power of the CROCUS reactor is 100 W. Currently there are fission chambers that carry out the neutron counting, which is a measure of the activity of the reactor. The new goal is to measure both neutrons and photons, but separately. The pulse shape analysis is a good solution for this task. For this, a 400 μm thick diamond detector with a specially designed casing was added to measure the activity. The LiF foil was added for conversion of thermal neutrons. The ROSY box with the integrated PSA routine was used for signal analysis.

The results from a test run at 10 W output power are shown in figure 5.24. The data include a mixed field consisting of fast neutrons, photons and of α and 3He particles as products of thermal neutron decay (due to a LiF foil in front of the detector). The data after the applied cuts again show a distinct 3He cluster, as well as the three-lane neutron signature. The α signal is buried under the signals stemming from fast neutrons and photons.

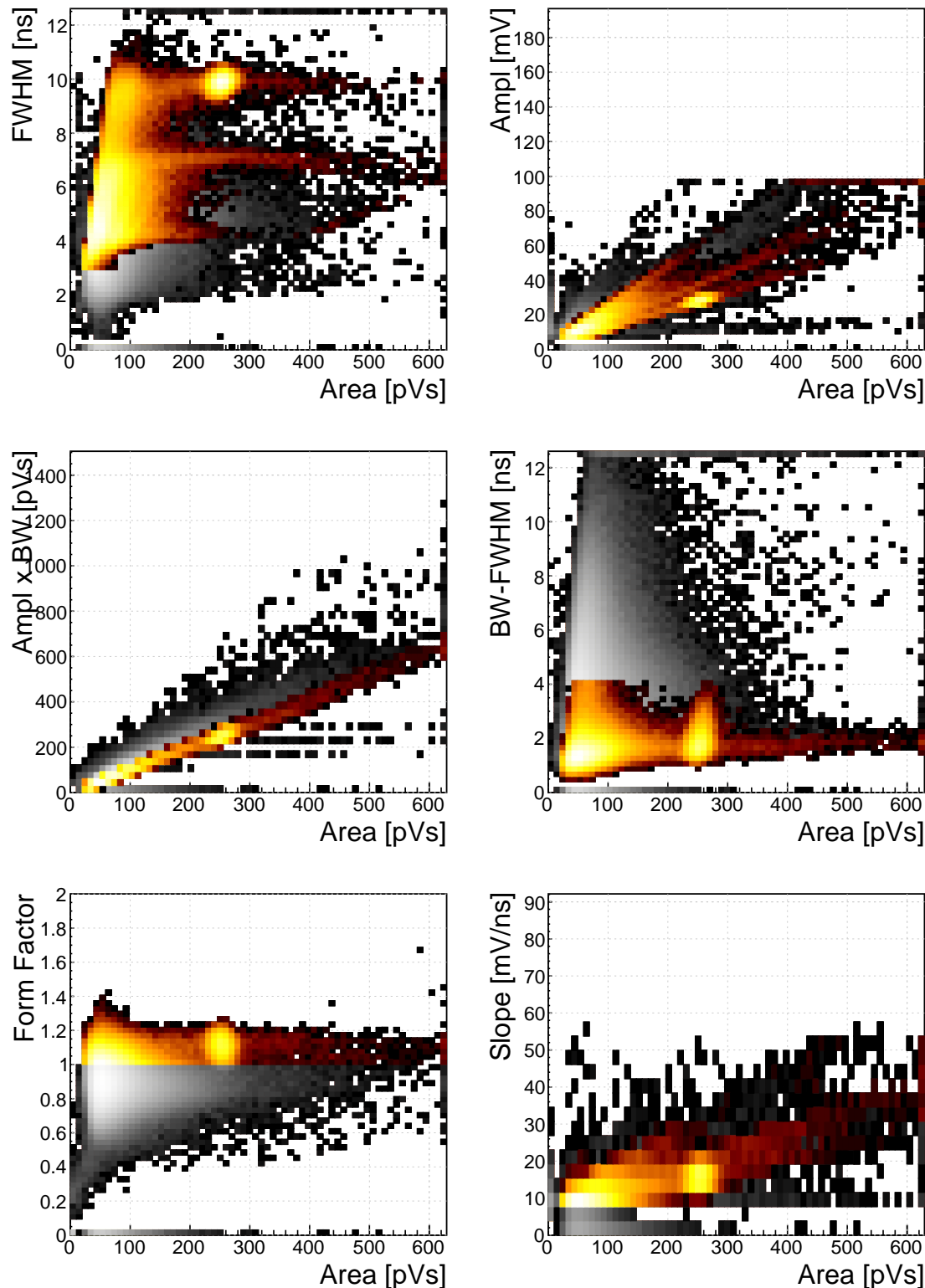


Figure 5.24: Fast neutrons, thermal neutrons, photons. Qualifiers: BW-FWHM 0–4 ns, FWHM 3–12 ns, Form factor 1.45, Slope 10–108 mV/ns

2665 **5.11 Conclusion**

2666 This chapter describes a system that can identify the type of radiation in real time.
2667 The system is implemented on an FPGA in a CIVIDEC ROSY box and is used with
2668 diamond detectors. The signal from the diamond sensor is read in and analysed in the
2669 firmware. First the shape of the pulse is parametrised. Then the logic determines the
2670 type of particle according to the user defined cuts. Finally the parameters are written
2671 into a histogram, which is read out by the user. The firmware is designed to carry
2672 out the pulse shape analysis of a single pulse in ~ 200 ns, yielding a maximum pulse
2673 rate of 5×10^6 particles per second. The rate as well as the linearity the measurement
2674 stability with respect to noise have been verified using a pulse generator. Then
2675 several radioactive sources were used to calibrate the device. Finally the system was
2676 installed in two neutron reactors to test the operation in a mixed field containing
2677 thermal neutrons, fast neutrons and photons. Various cuts were tested to optimise
2678 the identification.

₂₆₇₉

Bibliography

- ₂₆₈₀ [1] *ASIC*. http://www.embedded-systems-portal.com/CTB/CTB_images/L2/L2 ASIC.jpg.
- ₂₆₈₁ [2] *Atominstytut, Technical University of Vienna, Austria*.
₂₆₈₂ <http://ati.tuwien.ac.at/startpage/EN/>.
- ₂₆₈₃ [3] *CROCUS neutron reactor*. <http://lrs.epfl.ch/page-55655-en.html>.
- ₂₆₈₄ [4] *DRS4*. <https://www.psi.ch/drs/evaluation-board>.
- ₂₆₈₅ [5] *Element Six*. <http://www.e6.com>.
- ₂₆₈₆ [6] *European Centre for Nuclear Research, CERN*. <http://home.cern>.
- ₂₆₈₇ [7] *IHa Technologies Pte. Ltd.* <https://www.2atechnologies.com>.
- ₂₆₈₈ [8] *ITER fusion reactor*. <https://www.iter.org/>.
- ₂₆₈₉ [9] *Neutron Time-of-flight experiment*. <https://ntof-exp.web.cern.ch/ntof-exp/>.
- ₂₆₉₀ [10] *Paul Scherrer Institute*. <https://www.psi.ch/>.
- ₂₆₉₁ [11] *RD42 collaboration*. <http://rd42.web.cern.ch/rd42/>.
- ₂₆₉₂ [12] *TRIGA MARK II neutron reactor*. <http://ati.tuwien.ac.at/reactor/EN/>.
- ₂₆₉₃ [13] *Xilinx Virtex 5 FPGA*. <http://www.hdl.co.jp/XCM-109/top.560.jpg>.
- ₂₆₉₄ [14] *Determination of operational dose equivalent quantities for neutrons*. ICRU,
₂₆₉₅ Washington, DC, 2001.
- ₂₆₉₆ [15] General Atomics. *View of the TRIGA reactor*. 2015.
- ₂₆₉₇ [16] H. Bethe and J. Ashkin. *Experimental Nuclear Physics*, ed. E. Segre, page 253,
₂₆₉₈ 1953.
- ₂₆₉₉ [17] W. Blum, W. Riegler, and L. Rolandi. Particle Detection with Drift Chambers,
₂₇₀₀ volume 2 of 2. Springer-Verlag, Berlin Heidelberg, 2008.
- ₂₇₀₁ [18] Giorgio Brianti. SPS North Experimental Area. Technical Report CERN-SPSC-
₂₇₀₂ T-73-8. LabII-EA-Note-73-4, CERN, Geneva, 1973.

BIBLIOGRAPHY

- [19] Maximilien Brice. *View of the nTOF detector*. Oct 2010.
- [20] Maximilien Brice. *LHC tunnel*. Jan 2011.
- [21] P. Carazzetti and H. R. Shea. *Electrical breakdown at low pressure for planar microelectromechanical systems with 10- to 500 μm gaps*. *J. Micro/Nanolith. MEMS MOEMS*, (8(3), 031305), Jul-Sep 2009.
- [22] Daniel Dominguez. *Standard Model. Le modele standard*. General Photo, Mar 2015.
- [23] CIVIDEC Instrumentation GmbH. *sCVD diamond sensor*. <http://www.cividec.at>, 2015.
- [24] E. Griesmayer, R. Bergmann, H. Böck, M. Cagnazzo, P. Kavrigin, B. Morganbesser, and M. Villa. *A Novel Neutron Flux Monitor Based On Diamond Detectors at the Vienna TRIGA Mark II Reactor*. submitted to the proceedings of ICRR 2015, 2015.
- [25] E. Griesmayer and B. Dehning. Diamonds for beam instrumentation. *Physics Procedia*, 37:1997 – 2004, 2012. Proceedings of the 2nd International Conference on Technology and Instrumentation in Particle Physics (TIPP 2011).
- [26] Moritz Guthoff, Wim de Boer, and Steffen Mller. Simulation of beam induced lattice defects of diamond detectors using {FLUKA}. *Nuclear Instruments and Methods in Physics Research Section A: Accelerators, Spectrometers, Detectors and Associated Equipment*, 735:223 – 228, 2014.
- [27] M. Huhtinen. Simulation of non-ionising energy loss and defect formation in silicon. *Nuclear Instruments and Methods in Physics Research A*, 491:194–215, September 2002.
- [28] Hendrik Jansen, Norbert Wermes, and Heinz Pernegger. *Chemical Vapour Deposition Diamond - Charge Carrier Movement at Low Temperatures and Use in Time-Critical Applications*. PhD thesis, Bonn U., Sep 2013. Presented 10 Dec 2013.
- [29] P. Kavrigin, P. Finocchiaro, E. Griesmayer, E. Jericha, A. Pappalardo, and C. Weiss. *Pulse-shape analysis for gamma background rejection in thermal neutron radiation using CVD diamond detectors*. *Nuclear Instruments and Methods in Physics Research A*, (795), 2015.
- [30] P. Kavrigin, E. Griesmayer, F. Belloni, A.J.M. Plompen, P. Schillebeeckx, and C. Weiss. *$^{13}\text{C}(n,\alpha_0)^{10}\text{Be}$ cross section measurement with sCVD diamond detector*. submitted to EPJA, 2016.
- [31] Claude A. Klein. Radiation-induced energy levels in silicon. *Journal of Applied Physics*, 30(8):1222–1231, 1959.

BIBLIOGRAPHY

- 2739 [32] Gregor Kramberger, V. Cindro, A. Gorisek, I. Mandic, M. Mikuz, and M. Zavr-
2740 tanik. Effects of bias voltage during priming on operation of diamond detectors.
2741 *PoS*, Vertex2012:013, 2013.
- 2742 [33] W. Y. Liang. Excitons. *Physics Education*, 5:226–228, July 1970.
- 2743 [34] Claudia Marcelloni De Oliveira. *IBL installation into the inner detector of the*
2744 *ATLAS Experiment side C*. General Photo, May 2014.
- 2745 [35] M. Mikuž. *Diamond sensors for high energy radiation and particle detection*.
2746 TIPP, 2011.
- 2747 [36] W P C Mills. *The present performance of the SPS*. *IEEE Trans. Nucl. Sci.*,
2748 26(CERN-SPS-AOP-79-9):3176–3178. 3 p, Mar 1979.
- 2749 [37] S. F. Novaes. *Standard model: An Introduction*. In *Particles and fields. Pro-*
2750 *ceedings, 10th Jorge Andre Swieca Summer School, Sao Paulo, Brazil, February*
2751 *6-12, 1999*, 1999.
- 2752 [38] Joao Pequenao. *Computer generated image of the whole ATLAS detector*. Mar
2753 2008.
- 2754 [39] Heinz Pernegger. *The Pixel Detector of the ATLAS Experiment for LHC Run-2*.
2755 Technical Report ATL-INDET-PROC-2015-001, CERN, Geneva, Feb 2015.
- 2756 [40] S. Ramo. *Currents Induced by Electron Motion*. *Proceedings of the IRE*, 27:584–
2757 585, 1939.
- 2758 [41] V. Sarin. *Comprehensive Hard Materials*. Elsevier Science, 2014. p. 411.
- 2759 [42] W. Shockley. *Currents to Conductors Induced by a Moving Point Charge*. *Journal*
2760 *of applied Physics*, 9:635, 1938.
- 2761 [43] C. Weiss. A CVD diamond detector for (n,α) cross-section measurements. PhD
2762 thesis, TU Wien, Vienna, 2014.
- 2763 [44] C. Weiss, H. Frais-Kölbl, E. Griesmayer, and P. Kavrigin. *Ionization signals of*
2764 *diamond detectors in fast neutron fields. publication in preparation*, 2016.
- 2765 [45] J. L. Yarnell, J. L. Warren, and R. G. Wenzel. Lattice vibrations in diamond.
2766 *Phys. Rev. Lett.*, 13:13–15, Jul 1964.